University of Louisville
ThinkIR: The University of Louisville's Institutional Repository

Electronic Theses and Dissertations

5-2017

A performance and visualization study on inlet geometries of a cross-flow fan.

Yoel Tanquero
University of Louisville

Follow this and additional works at: https://ir.library.louisville.edu/etd

Part of the Aerodynamics and Fluid Mechanics Commons, and the Applied Mechanics Commons

Recommended Citation

Tanquero, Yoel, "A performance and visualization study on inlet geometries of a cross-flow fan." (2017). *Electronic Theses and Dissertations.* Paper 4236.
https://doi.org/10.18297/etd/4236

This Master's Thesis is brought to you for free and open access by ThinkIR: The University of Louisville's Institutional Repository. It has been accepted for inclusion in Electronic Theses and Dissertations by an authorized administrator of ThinkIR: The University of Louisville's Institutional Repository. This title appears here courtesy of the author, who has retained all other copyrights. For more information, please contact thinkir@louisville.edu.

A PERFORMANCE AND VISUALIZATION STUDY ON INLET GEOMETRIES OF A CROSS-FLOW FAN

By

Yoel Tanquero
B.S., Florida International University, 2014

A Thesis
Submitted to the Faculty of the
University of Louisville
J.B. Speed School of Engineering
in Partial Fulfillment of the Requirements
for the degree of

Master of Science

in Mechanical Engineering

Department of Mechanical Engineering
University of Louisville
Louisville, KY

May 2017

A PERFORMANCE AND VISUALIZATION STUDY ON INLET GEOMETRIES OF A CROSS-FLOW FAN

By

Yoel Tanquero
B.S., Florida International University, 2014

A Thesis Approved on

April 12, 2017

by the following Thesis Committee:

_____
Dr. Ellen Brehob, Thesis Co-Advisor

_____
Dr. Andrea Kelecy, Thesis Co-Advisor

_____
Dr. Michael McIntyre, Committee Member

DEDICATION

I dedicate this thesis to all my family and friends for their love and support throughout the years. In particular, I want to dedicate it to my parents Rosa and Nelson Tanquero, my big brother Nelson, and my lovely wife Deanna.

ACKNOWLEDGMENTS

I would like to thank my advisors, Dr. Brehob, Dr. Kelecy, and James Armstrong for their guidance, advice, and support during this past year. In particular, I would like to thank Dr. Brehob and Dr. Kelecy, for their dedication, their countless and continuous advice, and their willingness to proof read each section multiple times. I have been very lucky to have all of you as advisors. I would like to thank Dr. McIntyre for his support and agreeing to serve on the committee.

Special thanks to James Armstrong, the best assignment leader that I could ever ask for. Your knowledge guided me throughout this thesis and I really appreciate it.

I would like to thank the staff of GE Appliances a Haier Company, my manager Tim O'Connell, and the rest of the staff who provide us with infinite opportunities to continuously learn and grow. Also, thank you so much for allowing me to conduct this research in your facilities and providing all the resources requested.

Finally, I want to thank my wife, Deanna, for her support, her unconditional love, and many nights of brainstorming.

ABSTRACT

A PERFORMANCE AND VISUALIZATION STUDY ON INLET GEOMETRIES OF A CROSS-FLOW FAN

Yoel Tanquero

April 12, 2017

A study was conducted to characterize the flow-field in the suction region of different inlet geometries of a cross-flow fan. The characterization was accomplished by correlating the static performance curves measured for each fan-inlet configuration to the streamline plot obtained using a particle tracking velocimetry (PTV) measurement system at two constant flow rates (40 and 55 CFM). The PTV measurement system used was developed by the author and uses helium bubbles as tracers, an LED light sheet, a slow motion camera, and a Matlab program. Four inlet geometry design variables were defined and independently studied to evaluate the effect on fan performance. The flow visualization results showed reasonable agreement with the fan performance curves measured. For example, the appearance of large vortices and other flow structures showed a reduction in fan performance. One key result was that the distance from the center of the impeller to the inlet expansion point is a critical variable. It was verified that reducing the ratio of ε_2/D_2 (where ε_2 is vortex wall distance and D_2 is the outer impeller diameter) below 7.66% improves the performance of the fan, but as ε_2/D_2 decreases the noise and vibration of the fan increases. Inlet geometries were identified that preserve up to 75% of the original fully-open average fan performance in constricted spaces.

TABLE OF CONTENTS

DEDICATION iii

ACKNOWLEDGMENTS iv

ABSTRACT v

LIST OF TABLES ix

LIST OF FIGURES xi

1. INTRODUCTION 1

2. LITERATURE REVIEW 3

2.1. Cross-Flow Fans 3

2.1.1. Design of Cross-flow fans 3

2.1.2. Characteristic Vortex Location 6

2.2. Fan Characteristic Curve 9

2.2.1. Performance and Efficiency 10

2.2.2. Typical performance and efficiency of cross-flow fans 13

2.3. Pressure Measurements 14

2.4. Airflow Visualization 18

2.4.1. Image Velocimetry Methods 20

2.4.2. Matlab: Computer Vision and Kalman Filter 23

2.5. Summary 24

3. METHODOLOGY 25

3.1. Design of Test Fixture 26
3.1.1. Cross-Flow Fan 26
3.1.2. Inlet Geometries and Design Variables 27
3.1.3. Fan-Duct System 31
3.1.4. Measurement Systems 36
3.2. Fan Characterization Methodology 44
3.2.1. Pressure and Volumetric Flow Rate Measurement 44
3.2.2. Fan Speed Measurement 46
3.2.3. Fan Performance and Efficiency Curves 47
3.2.4. Flow Rate Comparison 50
3.2.5. Measurement Uncertainty 52
3.3. Airflow Visualization 54
3.3.1. Helium Bubble Generator 55
3.3.2. Illumination and Background 57
3.3.3. High Speed Video 62
3.3.4. Post-Processing: Matlab Program 65
3.3.5. PTV System Calibration Test 71
4. RESULTS 75
4.1. Performance and Efficiency Curves 75
4.2. Flow Visualization Results 82
4.3. Discussion of the Results 96
5. CONCLUSIONS AND RECOMMENDATIONS 107
Future Work 108

REFERENCES 110

APPENDICES 113

Appendix A: Matlab Program Logic 114

Appendix B: Static Efficiency Curves 115

Appendix C: Performance Curves using Dimensionless Coefficients 118

Appendix D: Efficiency Curves using Dimensionless Coefficients 121

Appendix E: Performance Test Measurements 124

CURRICULUM VITAE 134

LIST OF TABLES

Table 3-1 Design variables for each inlet geometry 30

Table 3-2 Velocity transverse measured with Centroids of Equal Area Method . 41

Table 3-3 Velocity transverse measured with Log-Tchebycheff Method 41

Table 3-4 Set of values to calculate flow rate with an airflow chamber..... 43

Table 3-5 Measurement and combined uncertainties 53

Table 4-1 Vortex wall length increment and resultant ratio ($\varepsilon 2/D2$)..... 99

Table 4-2 Average relative performance for each inlet geometry 104

Table Appendices-1 Performance measurements: inlet geometry 0..... 124

Table Appendices-2 Performance measurements: inlet geometry 1..... 124

Table Appendices-3 Performance measurements: inlet geometry 2..... 124

Table Appendices-4 Performance measurements: inlet geometry 3..... 125

Table Appendices-5 Performance measurements: inlet geometry 4..... 125

Table Appendices-6 Performance measurements: inlet geometry 5..... 125

Table Appendices-7 Performance measurements: inlet geometry 6..... 126

Table Appendices-8 Performance measurements: inlet geometry 7..... 126

Table Appendices-9 Performance measurements: inlet geometry 8..... 126

Table Appendices-10 Performance measurements: inlet geometry 9..... 127

Table Appendices-11 Performance measurements: inlet geometry 10..... 127

Table Appendices-12 Performance measurements: inlet geometry 11..... 127

Table Appendices-13 Performance measurements: inlet geometry 12..... 128

Table Appendices-14 Performance measurements: inlet geometry 13..... 128

Table Appendices-15 Performance measurements: inlet geometry 14..... 128

Table Appendices-16 Performance measurements: inlet geometry 15..... 129

Table Appendices-17 Performance measurements: inlet geometry 16..... 129

Table Appendices-18 Performance measurements: inlet geometry 17..... 129

Table Appendices-19 Performance measurements: inlet geometry 18..... 130

Table Appendices-20 Performance measurements: inlet geometry 19..... 130

Table Appendices-21 Performance measurements: inlet geometry 20..... 130

Table Appendices-22 Performance measurements: IG 0 VW +0.04" 131

Table Appendices-23 Performance measurements: IG 0 VW +0.08" 131

Table Appendices-24 Performance measurements: IG 0 VW +0.12" 131

Table Appendices-25 Performance measurements: IG 0 VW +0.16" 132

Table Appendices-26 Performance measurements: IG 0 VW +0.20" 132

Table Appendices-27 Performance measurements: IG 7 VW +0.12" 132

Table Appendices-28 Performance measurements: IG 7 VW +0.16" 133

Table Appendices-29 Performance measurements: Fan without inlet geometry 133

LIST OF FIGURES

Figure 2-1 Original drawing from Mortier's patent (Mortier, 1893) 4

Figure 2-2 Cross-flow fan components and parameters (Tuckey, 1983)..... 5

Figure 2-3 Flow in a cross-flow fan impeller without housing (Eck, 1973)..... 6

Figure 2-4 Eccentric vortices Left: (Tuckey, 1983) Right: (Eck, 1973)..... 7

Figure 2-5 Designs by Eck (right) Ikegami and Murata (left) (Mazur, 1984)..... 8

Figure 2-6 Fukutomi and Nakamura experimental setup (2005)..... 9

Figure 2-7 Fan test setup with airflow chamber per ANSI/AMCA 210 (2000) ... 10

Figure 2-8 Typical fan performance curves (Strike, 2014)..... 12

Figure 2-9 Orifice effect on static pressure measurement (Rayle Jr., 1949) 16

Figure 2-10 Recommended pressure tap location..... 17

Figure 2-11 Suggested distance between impeller and any walls at inlet..... 19

Figure 2-12 Schematic of a 2D PIV system (2014)..... 20

Figure 3-1 Cross-flow fan used for the experiment..... 26

Figure 3-2 Cross-flow fan design parameters..... 27

Figure 3-3 Side view of inlet geometry 16 with the design variables 28

Figure 3-4 Inlet geometries studied for every design variables..... 29

Figure 3-5 Dimensions kept constant for all inlet geometries studied..... 31

Figure 3-6 CAD model of a section of the test fixture 32

Figure 3-7 Loss coefficients for a set of entrance conditions (Jorgensen, 1983) 34

Figure 3-8 Contraction cone showing semi-angles..... 35

Figure 3-9 Contraction cone: CAD model (left) and 3D printed part (right) 35

Figure 3-10 Full CAD model of the test fixture 36

Figure 3-11 Design guidelines for a pressure tap (Jorgensen, 1983)..... 38

Figure 3-12 Airflow chamber exterior (left), interior (right)..... 39

Figure 3-13 Physical average of static pressure on outlet duct..... 39

Figure 3-14 Measurement locations for Centroids of Equal Area method..... 40

Figure 3-15 Measurement locations for Log-Tchebycheff method..... 41

Figure 3-16 Fluke 922 digital manometer 45

Figure 3-17 Static pressure measurement locations..... 46

Figure 3-18 Cross-flow fan used in the experiment..... 47

Figure 3-19 Static performance and efficiency curves for the cross-flow fan..... 49

Figure 3-20 Dimensionless performance and efficiency curves..... 50

Figure 3-21 Airflow restriction for constant flow rate measurements..... 52

Figure 3-22 Fan characteristic curve with upper and lower uncertainty curves ... 54

Figure 3-23 Helium Bubble Generator Model 5 (Sage Action, 2016) 55

Figure 3-24 Helium Bubble Generator: micro-metering valves..... 56

Figure 3-25 Projected field of view of the LED light sheet (CAD Model) 59

Figure 3-26 Light analysis locations..... 61

Figure 3-27 Four consecutive video frames (Iphone 6 @240 fps) 63

Figure 3-28 Four consecutive video frames (Sony RX100IV @960 fps) 65

Figure 3-29 User interface 69

Figure 3-30 Velocity vector plot and streamlines plot for IG 0 at 55 CFM 71

Figure 3-31 Probability that St < 1 for different helium valve set points..... 73

Figure 4-1 Static performance: θ = expansion angle 75

Figure 4-2 Static performance for inlet geometries 2, 9, and 15 76

Figure 4-3 Static performance for inlet geometries 1 and 9 77

Figure 4-4 Static performance: X = distance to expansion point..... 78

Figure 4-5 Static performance: Y = distance to top wall 79

Figure 4-6 Static performance for inlet geometries 9 and 15 80

Figure 4-7 Static performance: δ = angle of guide vane near vortex wall 81

Figure 4-8 Streamlines: θ = expansion angle at 25 CFM 83

Figure 4-9 Streamlines: θ = expansion angle at 40 CFM 85

Figure 4-10 Streamlines: θ = expansion angle at 55 CFM 86

Figure 4-11 Streamlines: X = distance to expansion point at 40 CFM..... 88

Figure 4-12 Streamlines: X = distance to expansion point at 55 CFM..... 89

Figure 4-13 Streamlines: Y = distance to top wall at 40 CFM 92

Figure 4-14 Streamlines: Y = distance to top wall at 55 CFM 93

Figure 4-15 Streamlines: inlet geometries 2, 9, and 15 at 40 CFM 94

Figure 4-16 Streamlines: inlet geometries 2, 9, and 15 at 55 CFM 95

Figure 4-17 Relationship between X and static performance at 40 CFM..... 97

Figure 4-18 Representation of the flow field showing reversed flow 98

Figure 4-19 Static performance curves IG 0: W = length added to vortex wall ... 99

Figure 4-20 Streamlines plot IG 0: W = length added to vortex wall (40 CFM) 101

Figure 4-21 Streamlines plot IG 0: W = length added to vortex wall (55 CFM) 102

Figure 4-22 Static performance curves IG 7: W = length added to vortex wall . 105

Figure Appendices-1 Program logic diagram (red: from Matlab example) 114

Figure Appendices-2 Static Efficiency: θ = expansion angle..... 115

Figure Appendices-3 Static Efficiency: X = distance to expansion point 116

Figure Appendices-4 Static Efficiency: Y = distance to top wall..... 116

Figure Appendices-5 Static Efficiency: W = vortex wall added length 117

Figure Appendices-6 Static Efficiency: X and W..... 117

Figure Appendices-7 Dimensionless performance: θ 118

Figure Appendices-8 Dimensionless performance: X 119

Figure Appendices-9 Dimensionless performance: Y 119

Figure Appendices-10 Dimensionless performance: W 120

Figure Appendices-11 Dimensionless performance: X and W..... 120

Figure Appendices-12 Dimensionless efficiency: θ 121

Figure Appendices-13 Dimensionless efficiency: X 122

Figure Appendices-14 Dimensionless efficiency: Y 122

Figure Appendices-15 Dimensionless efficiency: W 123

Figure Appendices-16 Dimensionless efficiency: X and W..... 123

1. INTRODUCTION

Cross-flow fans are known for their small size, stable flow, and low noise operation. As a result, cross-flow fans are commonly used in applications such as wind curtains, cooling electronics, appliances, etc.; many of which have constricted inlet conditions. A rule of thumb suggested by cross-flow fans manufactures requires leaving a distance of one impeller diameter between any object and the impeller all around the suction region of the fan. However, this rule of thumb is not always followed due to the restricted space in some of these applications. In those cases, the typical solution requires incorporating more restrictive inlet geometries to the cross-flow fan.

These more restrictive fan-inlet configurations alter the aerodynamics in the suction region of the cross-flow fan, reducing its performance and modifying its characteristics curve. Typically, these performance drops have to be determined experimentally, which could be a long iterative process. This motivated a study of the impact of inlet design parameters on fan performance. The results of this study could ultimately be used to develop a design guide that can be used by engineers to design these inlet geometries. Previous published research focuses on impeller design, internal flow-field or vortex location, housing, and outlet conditions, but no published research discusses these fan-inlet configurations. There is a need to understand the effect that different inlet geometry parameters have in cross-flow fan performance.

As it was first demonstrated by Bruno Eck (1973), a renowned German fan researcher and inventor, flow visualization can be used to determine the location and size

of vortices as well as low velocity regions in cross-flow fans. An objective of this study is to characterize the flow-field in the suction region of different fan-inlet configurations by correlating performance measurements with airflow visualization. Airflow visualization techniques that are accurate enough to measure the flow-field are expensive. However, with recent technological developments in the fields of video cameras and computer vision, a particle tracking velocimetry (PTV) technique can be developed that is cost effective and that can measure the flow near the fan impeller with accuracy.

In this study, four inlet geometry design variables and a total of twenty-one inlet geometries were investigated. A test fixture that combines measuring the performance of the different fan-inlet configurations and recording the flow visualization videos for flow-field measurements was developed. The PTV measurement system was developed using Matlab: Image Processing and Computer Vision toolbox. The acceptable ranges of the design variables and a set of suitable inlet geometries were proposed.

2. LITERATURE REVIEW

2.1. Cross-Flow Fans

The concept of the cross-flow fan was first introduced by Mortier (Figure 2-1), a French electrical engineer, in 1892. During the first half of the 1900's, the cross-flow fan was widely used for mine ventilation, but it was replaced by what was known then as the Capell and Rateau fan, which is nothing more than the predecessor of the centrifugal fan (Cory, 2005). Many researchers improved the design and performance of the fan, but the applications were few due to their low efficiency in comparison to axial and cylindrical fans. With the invention of air curtains and air conditioning, during the 1970's, a need for a smaller and quieter fan grew. As a result, the cross-flow fan became the standard for such applications. Their implementation was, and is still today, mostly driven by space limitations on the design and low noise requirements.

2.1.1. Design of Cross-flow fans

The cross-flow fan has evolved since Mortier's patent and today, it has three main components: the impeller, the housing, and the vortex wall. The impeller is a rotor with closed ends and a cascade of blades on its curved surface (Tuckey, 1983). As shown in Figure 2-2, the housing and the vortex wall define the suction and discharge regions. An advantage over other types of fans is that the impeller diameter can be very small without losing too much flow. This is possible by increasing the axial length of the impeller. This flexibility is the main reason why the cross-flow fan is used in restricted space applications, like air conditioning systems.

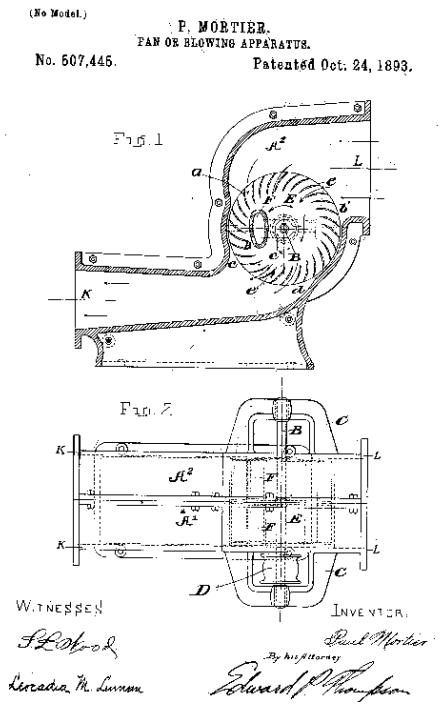

Figure 2-1 Original drawing from Mortier's patent (Mortier, 1893)

The design parameters of the fan are shown in Figure 2-2. In past studies, the typical numbers of blades have ranged from 18 to 36 blades depending on the impeller diameter. Typically, the inner blade angle (β_1) is 90°, but the effect of changing the angle over the range from 60° to 100° is negligible. For the impeller, the critical parameter is the outer blade angle (β_2). Previous studies have shown that β_2 should be greater than 22° for stability with values around 26° representing optimum (Tuckey, 1983). The vortex wall position angle (α_2) is determined by the ratio between the vortex wall distance (ε_2) and the impeller outer diameter (D_2). The optimal vortex wall position angle should be in the range from 10° to 20° for an $\varepsilon_2/D_2 = 7.5\%$ (Ikegami & Murata, 1966). Ikegami and Murata also showed that reducing the ratio ε_2/D_2 below 3% will increase the performance, but it will also increase the noise.

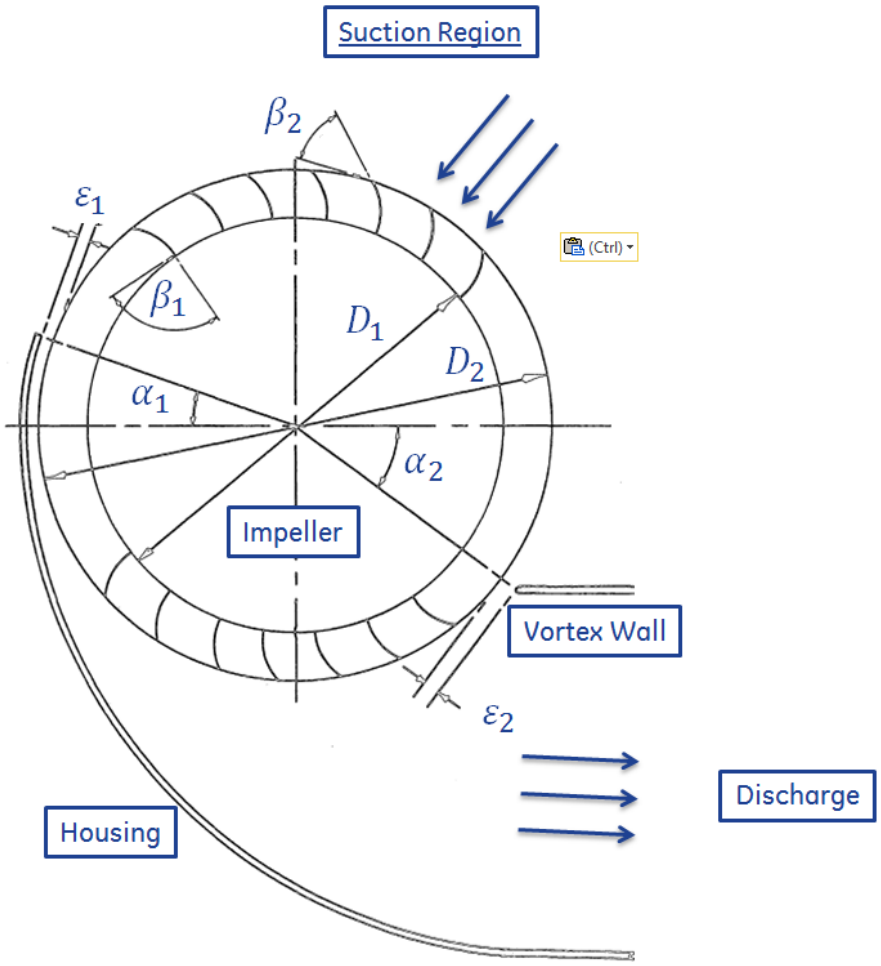

Figure 2-2 Cross-flow fan components and parameters (Tuckey, 1983)

The ratio of the impeller length to outside diameter ratio (L/D_2) should be around 1.6, although its effect highly depends on the material used to manufacture the impeller. For the inside diameter to outside diameter ratio (D_1/D_2) a value in the range from 0.70 to 0.85 produces good results (Tuckey, 1983). The housing position angle (α_1) should be approximately 20 degrees, although angles up to 40 degrees are acceptable. The housing distance to impeller outer diameter ratio (ε_1/D_2) should be between 9% and 12.5%. However, this parameter has small effect of the fan performance and is a function of other variables (Mazur, 1984).

Figure 2-3 shows that even without the housing, the impeller will generate a free stream (Eck, 1973). However, without the housing and the vortex wall, the suction and discharge locations cannot be predicted because they will develop spontaneously.

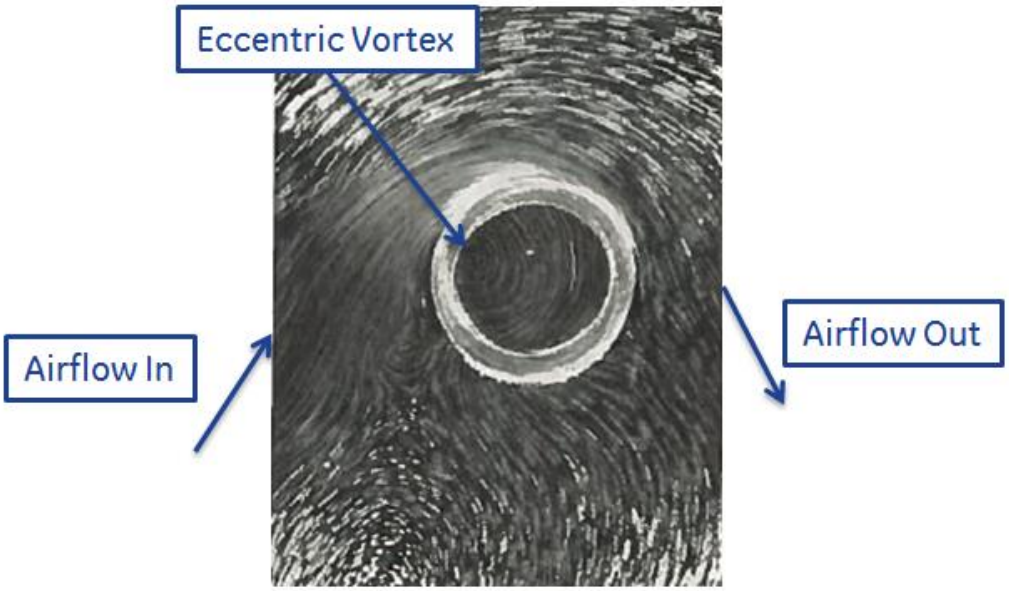

Figure 2-3 Flow in a cross-flow fan impeller without housing (Eck, 1973)

2.1.2. Characteristic Vortex Location

Unlike any other type of fan, the air in cross-flow fans passes twice through the impeller. The vortex wall, as stated by its name, creates an eccentric vortex in the inside edge of the discharge region of the impeller (see Figure 2-4). This vortex also defines the through-flow section. The size and location of the vortex varies depending on the flow velocity. The eccentric vortex is the feature, that above all others, defines the efficiency and stability of a cross-flow fan. Minimizing the vortex size and placing it to the internal edge of the blades improves the performance of the cross-flow fan. This is the main reason why the eccentric vortex has been a research topic for many years.

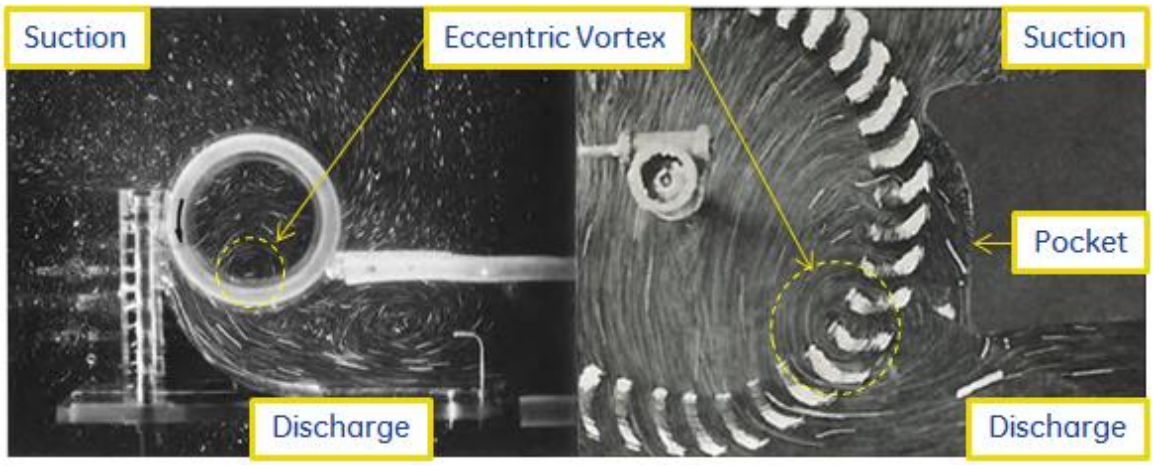

Figure 2-4 Eccentric vortices Left: (Tuckey, 1983) Right: (Eck, 1973)

Bruno Eck proposed a recirculation passage that he called a "pocket" in which the back flow can return to the impeller externally (see Figure 2-4 right). This solution controlled the vortex by moving it closer to the vortex wall and away from the center of the discharge region of the impeller. However, experiments by Ikegami and Murata (1966) showed that the optimum performance can be achieved with a flat vortex wall with round end or a tongue (see Figure 2-5 left). This was also confirmed by Porter and Markland (1970). In addition, it was shown that the angle β_2 and the ratio ε_2/D_2 have a direct effect on the vortex location (Ikegami & Murata, 1966).

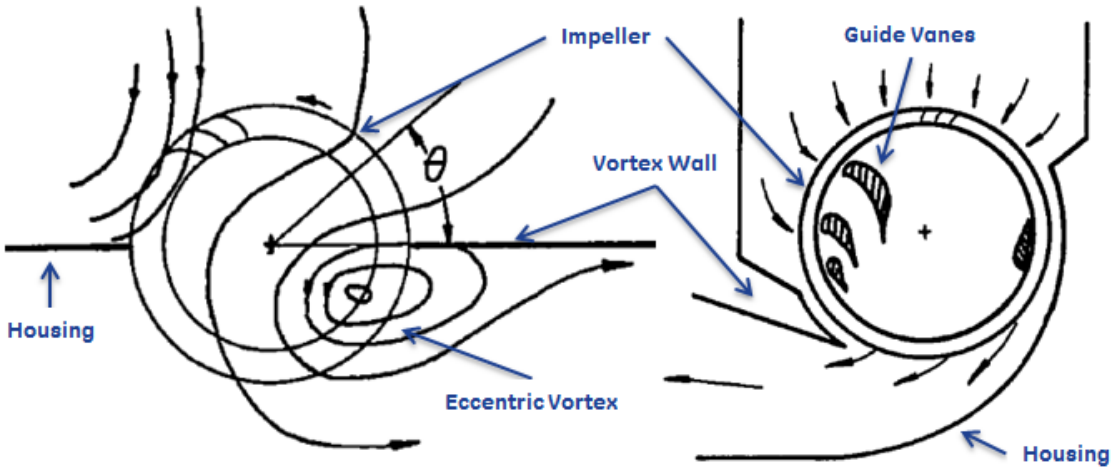

Figure 2-5 Designs by Eck (right) Ikegami and Murata (left) (Mazur, 1984)

Another way to control the eccentric vortex is by adding a vane guide inside the impeller (see Figure 2-5 right). It has been proven that interior vane guides can be used to make the vortex small and stable (Murata et al., 1978). However, this solution is very difficult to implement in a cost effective way, and it is particularly challenging for small and long impellers.

Andrea Toffolo (2004) studied the housing geometry and the vortex wall thickness concluding that higher positions of a thin vortex wall (smaller α_2) result in a more stable characteristic curve. Murata and Nishihara (1976) also studied the effect of radial fan housing concluding that its effect in performance is less significant than the effect that β_2 or ε_2/D_2 have. However, Kim et al. (2008) showed that replacing the radial housing with an Archimedes spiral will increase the pressure coefficient and the efficiency of the cross-flow fan.

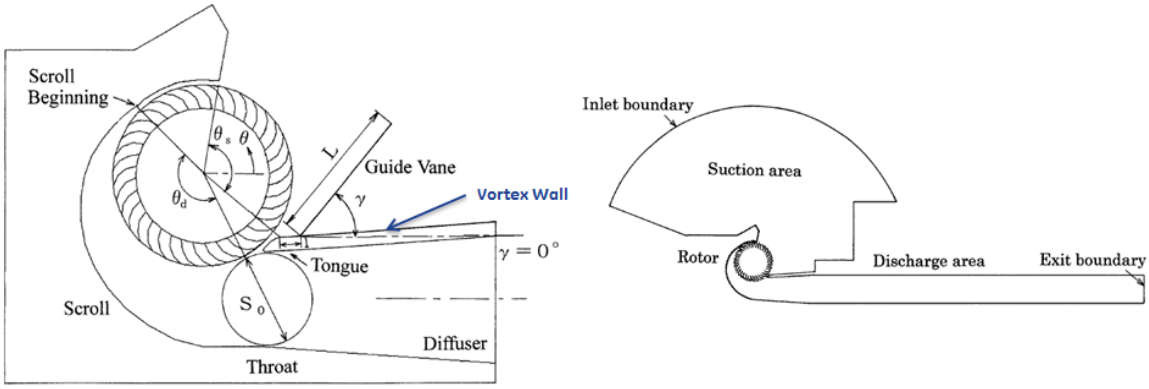

Figure 2-6 Fukutomi and Nakamura experimental setup (2005)

During the years researchers have focused on studying the eccentric vortex, the vortex wall, and the fan housing and their relationship to the performance and efficiency of the fan. Only one study was found that discussed the way that the performance of the fan is affected by some type of inlet geometry. Fukutomi and Nakamura (2005) studied the effect of a guide vane on a cross-flow fan (see Figure 2-6). Their study shows that adding an inlet guide vane will increase the performance of the fan. However, their fan configuration requires a fully open inlet condition and some applications require inlet geometry restrictions that have not been investigated in previous studies. As a result, there is a need to study the effect that inlet geometries have in the performance of the cross flow fan.

2.2. Fan Characteristic Curve

The fan characteristic curve represents the performance of the fan operating under a specific set of conditions. The performance of the fan is given by the relationship between total pressure or static pressure and the volumetric flow rate at a constant voltage, air temperature, and fan impeller speed. In the United States of America the fan characteristic curve is determined as the static pressure in inches of water and the

volumetric flow rate in CFM. The ANSI/AMCA 210 provides the standard procedures, test setup, and laboratory equipment required to determine the fan characteristic curve (2000).

2.2.1. Performance and Efficiency

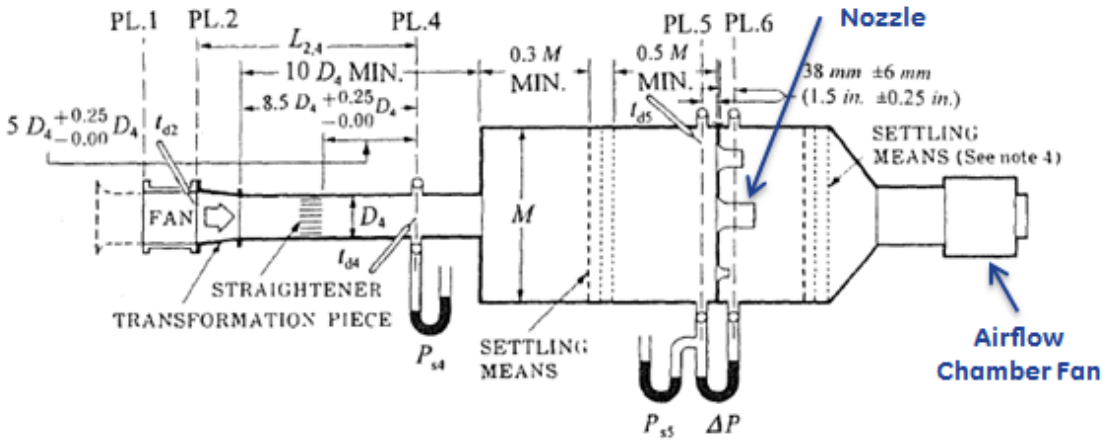

Figure 2-7 Fan test setup with airflow chamber per ANSI/AMCA 210 (2000)

The ANSI/AMCA 210 describes the procedure to measure the fan characteristic curve. The standard provides 10 different test setups covering a broad range of operating conditions of the fan. For example, Figure 2-7 shows the recommended test setup for a fan operating with a ducted inlet and a ducted outlet. Although it is not shown in Figure 2-7, the ANSI/AMCA 210 clearly states that the ducted inlet condition shall be simulated, which means that the any obstruction or modification should be taken into account including inlet geometries (2000).

Using the setup shown in Figure 2-7, the fan characteristic curve is determined by measuring the pressure at P_{s4} as well as P_{s5}, the pressure across the nozzle inside the chamber. The pressure across the nozzle P_{s5}, is used to determine the volumetric airflow.

Equation 1 is used to calculate volumetric flow rate across the nozzle in an airflow chamber (Abdelaziz et al., 2005)

$$\dot{Q} = 1096\, Y \sqrt{\Delta P_{nozzle}\, \rho_{nozzle}}\, C_{nozzle}\, A_{nozzle} \tag{1}$$

where Q is the volumetric flow rate in cubic feet per minute (CFM), ΔP_{nozzle} is the static pressure measured across the nozzle in inches of water (inH_2O), ρ_{nozzle} is the air density in pounds per cubic foot (lb/ft^3) determined from the air temperature at the nozzle, A_{nozzle} is the nozzle cross sectional area in square inches (in^2), and the expansion factor, Y, and nozzle discharge coefficient, C_{nozzle}, are determined from equations 2 and 3 respectively.

$$Y = 1 - (0.548 + 0.71\, \beta^4)(1 - \alpha) \tag{2}$$

$$C_{nozzle} = 0.9986 - \left(\frac{7.006}{\sqrt{Re_{nozzle}}}\right) + \left(\frac{134.6}{Re_{nozzle}}\right) \tag{3}$$

For Equation 2, the coefficients α and β are determined by equations 4 and 5, where α is the ratio of absolute pressures at the exit and inlet of the nozzle, and β is the ratio of nozzle throat diameter to chamber diameter. Also, for Equation 3, the Reynolds number for flow through the nozzle is approximated from Equation 6.

$$\alpha = \frac{P_{nozzle,\ exit}}{P_{nozzle,\ upstream}} \tag{4}$$

$$\beta = \frac{D_{nozzle}}{D_{chamber}} \tag{5}$$

$$Re_{nozzle} = 1{,}363{,}000\, D_{nozzle} \sqrt{\frac{\Delta P_{nozzle}\, \rho_{nozzle}}{1 - \beta^4}} \tag{6}$$

The ANSI/AMCA 210 states that the fan curve is measured from zero flow to the maximum flow condition and that there has to be a minimum of 8 points to fully plot a

fan characteristic curve (2000). Figure 2-8 shows an example of a typical fan performance curve with its respective efficiency curve and a system curve. The fan static efficiency curve is determined from Equation 7 (Strike, 2014)

$$\eta = \frac{\dot{P}_{out}}{\dot{P}_{in}} \tag{7}$$

where $\dot{P}_{in}$ is usually determined experimentally and is the power input to the fan. The power output $\dot{P}_{out}$ is given by Equation 8.

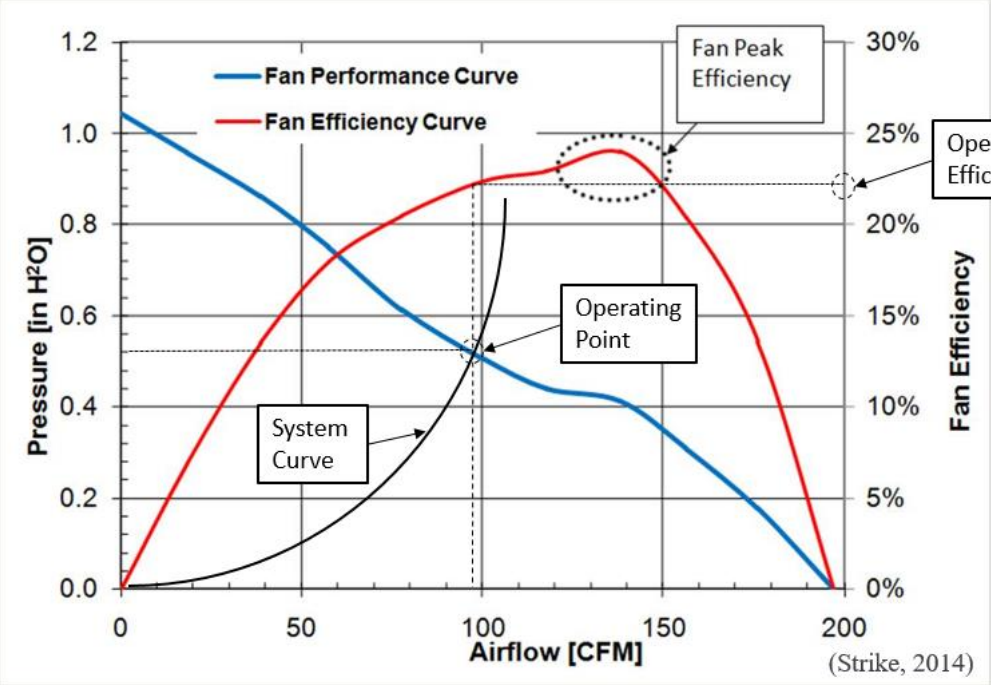

Figure 2-8 Typical fan performance curves (Strike, 2014)

$$\dot{P}_{out} = \Delta P_{fan}\, \dot{Q} \tag{8}$$

The system curve is the sum of the static pressure losses in the system as a function of flowrate. This curve can be estimated for simple systems by adding the losses of the ducts, elbows, contractions, expansions, and the losses across equipment.

However, it is commonly determined experimentally. The operating point is the location where the system curve intercepts the fan characteristic curve and the operating efficiency of the fan is the corresponding efficiency of the fan at that same airflow rate.

Dimensionless coefficients

Many researchers prefer to determine the fan performance curves using dimensionless coefficients instead of the international system of units or imperial units. Equation 9 is used to determine the flow coefficient ϕ (Jorgensen, 1983)

$$\phi = \frac{\dot{Q}}{LD_2U_2} \tag{9}$$

where $\dot{Q}$ is the volumetric flow rate, L is the length of the impeller, D_2 is the outside diameter of the impeller, and U_2 is the blade tip speed. The blade tip speed is calculated by multiplying the circumference length of the impeller by the rotational speed.

The pressure coefficient ψ, also known as head coefficient, is determined with Equation 10, where P_s is the static pressure, ρ is the air density, and U_2 is the blade tip speed.

$$\psi = \frac{P_s}{\frac{1}{2}\rho U^2} \tag{10}$$

2.2.2. Typical performance and efficiency of cross-flow fans

Some of Eck's designs achieved total pressure coefficient ψ of 3.6 at a flow coefficient ϕ of 1.5, and peak efficiency of over 60% (Eck, 1973). Mortier's fan had flow coefficient ϕ around 0.5 with very low pressure coefficient ψ, but efficiencies above 65% (Mazur, 1984). Tuckey (1983), Toffolo (2004), and Murata and Nishihara (1976), worked with very similar cross-flow fans. Their results were similar with the peak total pressure

coefficient ψ_T, slightly above 3.00 at a flow coefficient ϕ near 1.00, and the peak efficiencies near 50%.

For cross-flow fans, the selection criteria typically depend on the system curve, space and noise requirements. In general high efficiency fans are preferred. However, studies have shown that in cross-flow fans high efficiency is linked to high noise and low operating noise is one of the main benefits of cross-flow fans. As a result, many commercially available cross-flow fans have been designed with lower efficiency than the maximum found in previous research. In terms of performance, fan selection is highly dependent on the system curve and is usually a tradeoff. For example, for high resistance systems total pressure coefficients would be more important than high flow coefficient, so a low flow, high pressure fan characteristic curve would be preferred.

2.3. Pressure Measurements

Measurements in dynamic pressure systems can be complex because both the static and the dynamic pressure have to be measured in order to determine the total pressure. At any given point in the system, the total pressure is equal to the sum of the static pressure and the dynamic pressure. The static pressure is measured with pressure taps placed perpendicular to the flow in the fully developed region. Steady-state conditions are required in order to make good measurements. The dynamic pressure can be hard to measure directly; therefore, the total pressure is typically measured in its place (Heeley, 2005). The total pressure can be measured using a Pitot tube. Once the total pressure is measured, the dynamic pressure can be calculated by subtracting the static pressure from the total pressure. The dynamic pressure is used to determine the flow velocity or the flow rate in dynamic systems.

Another way to determine the dynamic pressure consists of measuring the velocity of the flow and using Equation 11 to calculate the dynamic pressure.

$$P_d = \frac{1}{2}\rho V^2 \tag{11}$$

Making static pressure taps may seem as simple as just making small perpendicular holes on the wall. However, they have to be made carefully to avoid significant sources of error. In theory the pressure tap orifice should be infinitely small with square edges. However, for flows in a duct with Reynolds numbers (Re_{duct}) less than 10^7 and for orifice sizes less than 0.01 duct diameters, the error will be less than 1% (Jorgensen, 1983). For the cross-flow fan used in this study the typical Reynolds number (Re_{duct}) ranged from 10^4 to 10^6. Another source of error for pressure taps is manufacturing defects in the orifice edge. Figure 2-9 shows some of the errors that can be introduced by common manufacturing errors. While orifice size and fitting eccentricity are definitely significant sources of error, studies show that failing to remove burrs can introduce errors of up to 15% (Jorgensen, 1983).

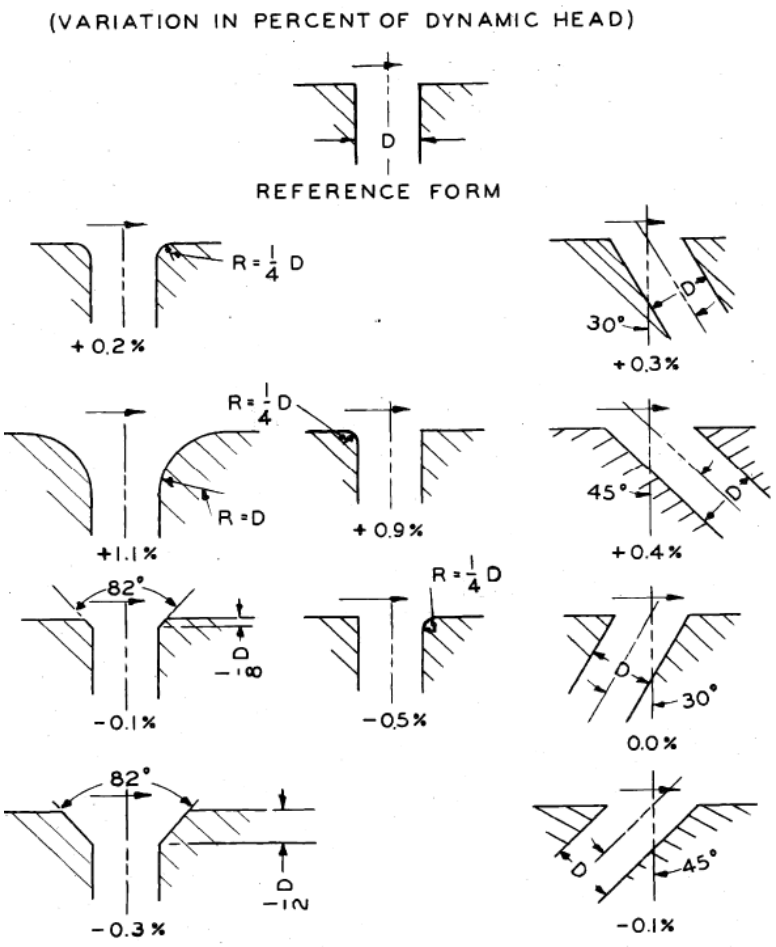

Figure 2-9 Orifice effect on static pressure measurement (Rayle Jr., 1949)

Once the pressure taps are properly made, taking the static pressure measurements is an accurate and simple process with the use of digital manometers. On the other hand, total pressure measurements are simple in terms of manufacturing, but they require meticulousness during data collection. For total pressure measurements, it is important that the Pitot tube is perfectly aligned parallel to the flow field with the tip pointing directly into the flow (Heeley, 2005). The direction is very important because the dynamic pressure is a vector quantity which depends on both direction and magnitude. A small misalignment of the Pitot tube produces a partial result instead of the total dynamic pressure value.

The location of the measurement must be selected carefully. A rule of thumb for pressure measurements is that the location of the measurement should be at least ten hydraulic diameters downstream and at least two hydraulic diameters upstream of any change or obstruction (see Figure 2-10). This rule of thumb ensures that the measurement is made at the fully developed region for turbulent flow inside a pipe or a duct.

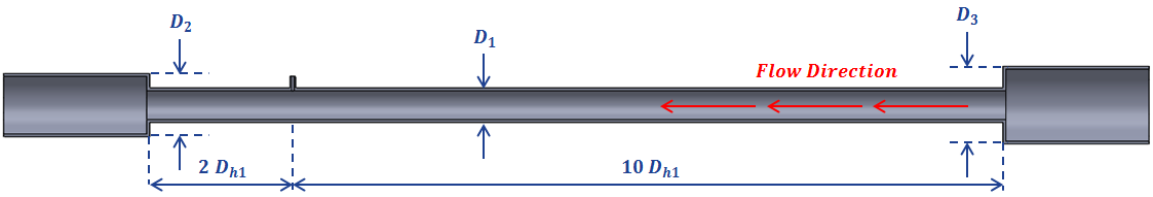

Figure 2-10 Recommended pressure tap location

The dynamic pressure field for flow inside a pipe or a duct is non-uniform; therefore, multiple measurements have to be made to find the average velocity or average dynamic pressure. The specific positions where the measurements have to be made are specific to each method. Two of the most common methods are the Centroids of Equal Areas and the Log-Tchebycheff.

The Centroids of Equal Areas method is the most common method of the two. In this method, the duct is divided into equal areas and the measurements are taken at the centroid of each area. "This method does not take into account the retardation of the flow near the wall, so a positive error nearly always results." (Jorgensen, 1983) The Log-Tchebycheff method assumes a logarithmic distribution near the wall and a polynomial distribution of the velocity elsewhere. For these two methods the average velocity is simply an average of the velocities measured. Multiplying the average velocity by the cross-sectional area gives the volumetric flow rate $\dot{Q}$.

2.4. Airflow Visualization

In Section 2.1.2 it was discussed how the angle of incoming air (β_2 in Figure 2-2) affects the location of the eccentric vortex which in turn alters the performance of the fan. Similar changes in performance are produced when the walls for the fan inlet geometry is close to the fan impeller, affecting the flow patterns in the suction region. As a rule of thumb, manufacturers suggest leaving a space of at least one impeller diameter between the impeller and any walls at the inlet. In addition, in Section 2.2.1 the fan characteristic curve provides useful information about the fan performance, but does not provide information about the complex aerodynamics in the vicinity of the fan. Experimental techniques like hot-wire anemometers are intrusive and provide only one-point measurements (Rezig et al., 2015). As a result, experimental flow visualization is commonly the technique used to study complex fluid mechanic problems in airflow related applications.

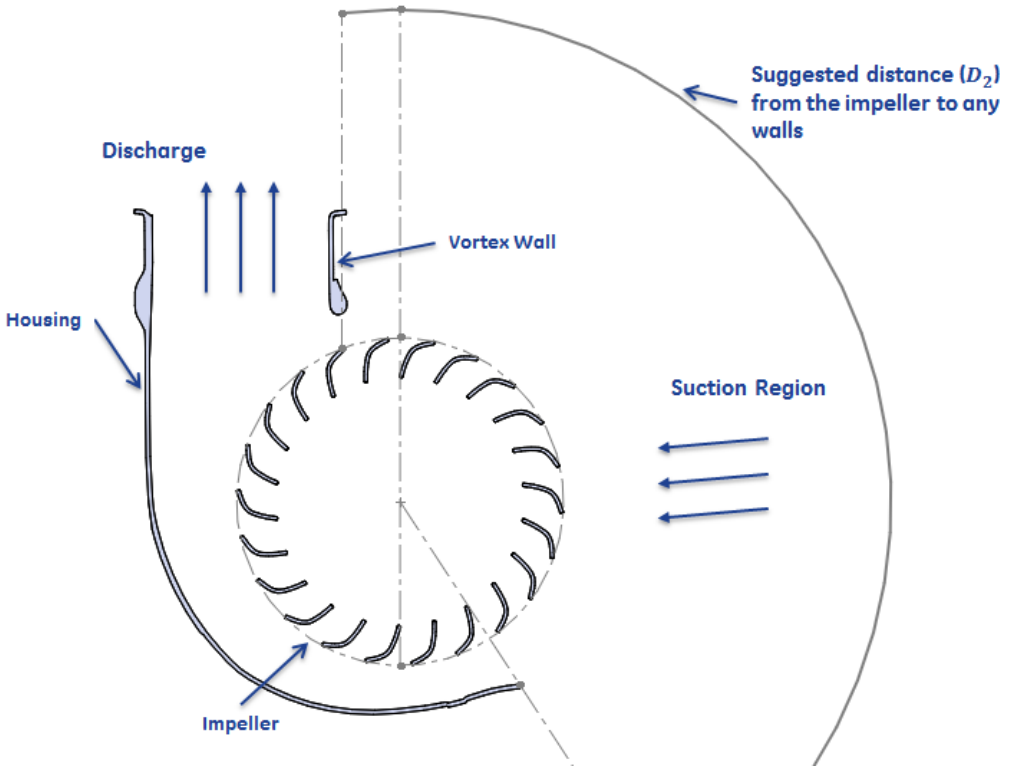

Figure 2-11 Suggested distance between impeller and any walls at inlet

There are many different types of flow visualization techniques; all have benefits and limitations. Every type of experimental flow visualization consists of at least three main parts: tracers, illumination, and image recording devices. The particles or small objects traveling with the flow are exposed by the illumination system while the camera records the flow. This is true for all the flow visualization techniques that are available including; particle image velocimetry (PIV), water tunnels with dye or flow particles, and wind tunnels with smoke or neutrally buoyant objects. Some of these techniques only offer qualitative information, while others, like the technique used in this study of fan geometries, offer quantitative data of the airflow velocity field. The process of computing a velocity field from a set of images is known as image velocimetry.

2.4.1. Image Velocimetry Methods

The most commonly used technique for flow velocimetry is PIV. The term PIV appeared in literature during the 1980's. During the last three decades, PIV evolved thanks to huge improvements made to video recording devices, illumination techniques, and computer software (Cao et al., 2014). Another flow velocimetry method is the Lagrangian or particle tracking velocimetry (PTV). The specific requirements, benefits, and limitations of each one of these methods are discussed in this section.

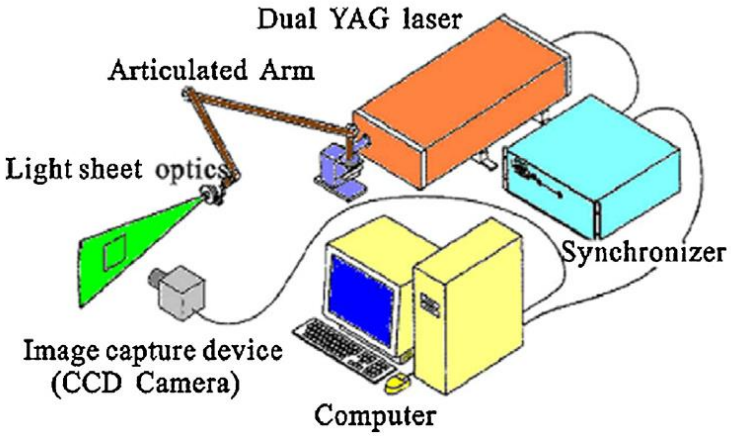

Figure 2-12 Schematic of a 2D PIV system (2014)

A typical PIV system consists of a tracer generator and a computer that simultaneously controls a multi-pulsed laser and one or more cameras. Usually, a double-pulsed Nd:YAG laser system that generates a green light sheet with a wavelength of 532 nm is used as illumination (see Figure 2-12). As tracers, either oil or aerosols containing Di-Ethyl-Hexyl-Sebacat (DEHS) are used for small-scale turbulence, while theatrical fog is used for continuous local flows. The recording device is either a coupled charged devices (CCD) camera or a complementary metal oxide semiconductor (CMOS) camera. The main difference between the two is that CCD has higher pixel resolution and is less

sensitive to noise, while CMOS is better for high-speed recording, which is needed for accurate turbulent information (Cao et al., 2014).

The PTV, similar to the PIV method, uses a light sheet, a CCD or a CMOS camera, tracer particles, and a specific evaluation algorithm. However, for the PTV method a bigger particle size and a lower particle density are preferred. These conditions provide an additional benefit because they allow the use of conventional light sources, like LEDs, instead of laser sheets. In addition, CMOS high-speed cameras are preferred for lower tracer particle density because a smaller time interval is more important than the high resolution provided by CCD cameras.

The PTV method determines the velocity field by analyzing each particle image, locating particle centroids, and connecting image tracks (Fu et al., 2015). The simplest way to achieve this is to threshold the image to separate pixels belonging to particles and pixels belonging to the background (Rezig et al., 2015). The particle centroid is found from the resultant binary image. A regression analysis is used to pair the particle centroids with their respective tracks. In comparison, the preferred evaluation method for PIV is performing a cross-correlation analysis using two separate fames. This analysis is known as adaptive correlation. Adaptive correlation is an algorithm that uses high-resolution pictures of high-density particles to calculate velocity vectors (Cao et al., 2014).

There are many PIV systems that are commercially available including open-source software for adaptive correlation. This is an advantage over PTV. However, the overall cost of a PIV system is considerably higher than the cost of a PTV system. In addition, the double-pulsed laser system used in PIV creates a light sheet that is between

0.04” and 0.12” thin (Cao et al., 2014). This is a limitation in cases when measuring a strong three-dimensional flow field. On the other hand, the threshold process used in PTV is very susceptible to noise and illumination issues. In conclusion, both systems can provide accurate velocity fields that will be very hard to measure otherwise.

Helium Bubbles as Particle Traces

Helium filled bubbles are used as tracers for PTV measurements because of their neutrally buoyant properties, relative suitable size, higher scattering efficiency, and relatively suitable lifetime (Fu et al., 2015). The diameter of the helium bubbles ranges from 0.03” to 0.18”. Kerho and Bragg (1994) showed that neutrally buoyant helium bubbles follow the flow. They also noticed that the helium bubble generator removes the helium bubbles that are heavier than air, but they do nothing to eliminate the lighter than air bubbles. These buoyant helium bubble deviate somewhat from the flow-field streamlines depending on the density ratio and the magnitude of the local pressure gradient. As a result, precise calibration of the helium bubble generator is required to reduce the number of buoyant bubbles.

The Stokes number can be used to estimate the behavior of tracer particle, in this case the helium bubbles, in the airflow. Equation 12 is the Stokes number, or the non-dimensional response time for a round tracking particle.

$$St = \frac{2}{9}\frac{\rho_p}{\rho_f}\left(\frac{a}{L}\right)^2 Re_{duct} \tag{12}$$

where ρ_p is the average bubble density, ρ_f is the density of the surrounding fluid, St is the Stokes number, a is the bubble radius, L is the duct hydraulic diameter, and Re is the duct Reynolds Number of the flow (Re_{duct}).

Equation 12 can be used to evaluate the quality of a tracer. For example, if $St < 1$ the bubbles follow the flow-field closely and if $St < 0.1$ the tracing accuracy errors are below 1%. On the other hand, if $St \gg 1$, bubbles will detach from the flow-field; therefore, they should not be used as a tracer. In general, the smaller the Stokes Number the better the bubbles follow the flow-field.

In a neutrally buoyant helium bubble, the ratio bubble density to fluid density (ρ_p/ρ_f) is equal to one. Since the helium bubble generator produces both, neutrally buoyant and buoyant bubbles, Kerho and Bragg suggested the use of a lower than one value for the density ratio, around 0.8, to determine if the buoyant bubbles are following the flow or not.

2.4.2. Matlab: Computer Vision and Kalman Filter

Matlab's Image Processing and Computer Vision toolbox are very powerful tools that can be used for all kinds of image and video processing. This is particularly useful for PIV and PTV measurement. Not surprisingly, there are multiple open source programs that perform PIV calculations using Matlab. The most commonly known is PIVlab. However, PIVlab uses adaptive correlation and, as mentioned in Section 2.4.1, this method requires images of high density of particles moving with the flow-field which are common for PIV measurements, but not for PTV measurements.

PTV measurements require tracking individual particles through the flow-field and this is achieved with a regression algorithm. As a result, the test has to be run with low tracer particle density. The Computer Vision toolbox has a built-in example that tracks multiple objects in motion simultaneously from a video file. This example uses a Kalman filter regression algorithm to track the objects moving in the video. As discussed

by Rezig (2015), the Kalman filter algorithm can be used to optimally estimate the new position of the object based on their actual position. The algorithm for motion-based multiple object tracking can be modified to perform PTV measurements by estimating the location of the particles and tracking their velocity and direction.

2.5. Summary

A review of the literature on cross-flow fans shows that there is agreement between the authors in terms of the design parameters that are critical to the cross-flow fan performance. In particular, there is agreement that the ratio of the vortex wall distance to the impeller outer diameter (ε_2/D_2) is the main contributor to the cross-flow fan performance. In addition, there is agreement that the fan performance is directly related to the size and location of the eccentric vortex.

There is agreement between most researchers that flow visualization is required to characterize the flow field. Most of the studies reviewed used water tunnels for flow visualization. However, recent technological advancements in the growing field of Particle Tracking Velocimetry (PTV) suggests that a PTV system using helium bubbles as tracers can be developed, validated, and used to study the suction region of a cross-flow fan.

Due to the eccentric vortex and turbulent nature of the cross-flow fan, most studies have been focused on characterizing the flow field and optimizing the fan parameters using ideal inlet and outlet conditions. This assumption of ideal inlet conditions is the reason why there is no published research about the inlet geometry effect on the cross-flow fan performance.

3. METHODOLOGY

The work conducted for this cross-flow fan study consisted of two main components. The first was to determine the fan performance and efficiency curves. This required measuring fan performance attributes such as volumetric flow rate, static pressure, fan speed, etc., for each one of the fan-inlet configurations. Static performance and static efficiency curves were developed for each case studied.

The second was to develop a particle tracking velocimetry (PTV) system to measure the velocity flow-field in the suction region of the cross-flow fan. A test fixture was developed that combined capabilities required for typical fan tests (like measuring static pressure, airflow rate, and fan speed) with features required for particle tracking velocimetry (like illumination and clear acrylic walls). This PTV system uses helium filled soap bubbles as tracers, the Sony RX100 VI CMOS camera, and a simple white LED light sheet. The ability of tracer particles to follow the flow was evaluated to demonstrate the validity of this method for the given flow-field. In addition, a Matlab program was developed that measures the flow field from the high frame rate videos recorded. The program combines multiple objects tracking with a Kalman filter regression algorithm to accurately measure the particles position, velocity and direction. The information obtained was used to determine a velocity vector field and a streamlines plot. These plots were used to identify flow structures that influence the fan performance and will aid in developing design guidelines for inlet geometries to ensure good fan performance.

3.1. Design of Test Fixture

A test fixture was designed to effectively measure the fan performance and the flow field. This fixture simulated a cross-flow fan operating inside a restricted duct and it included features like clear acrylic walls and illumination to perform the flow field measurements using particle tracking velocimetry. In addition, the fixture was designed to facilitate the evaluation of various inlet geometries of the fan. The following sections discuss the design and construction of the principal components of the test fixture.

3.1.1. Cross-Flow Fan

Figure 3-1 Cross-flow fan used for the experiment

The cross-flow fan used is shown in Figure 3-1. This fan is affordable and very common in the appliance industry. The impeller has a 60mm (2.36”) diameter, and it is made out of steel. The housing is also made out of steel. The motor is an AC two-speed motor, and it can be installed at either side of the housing with a twist-lock mechanism.

All measurements were made using only the high speed configuration to simplify the analysis.

An ATOS Core 185 3D scanner was used to accurately determine the fan dimensions. Figure 3-2 shows a fan cross-section with all the parameters of the fan. These parameters are within the acceptable limits of the fan discussed in Section 2.

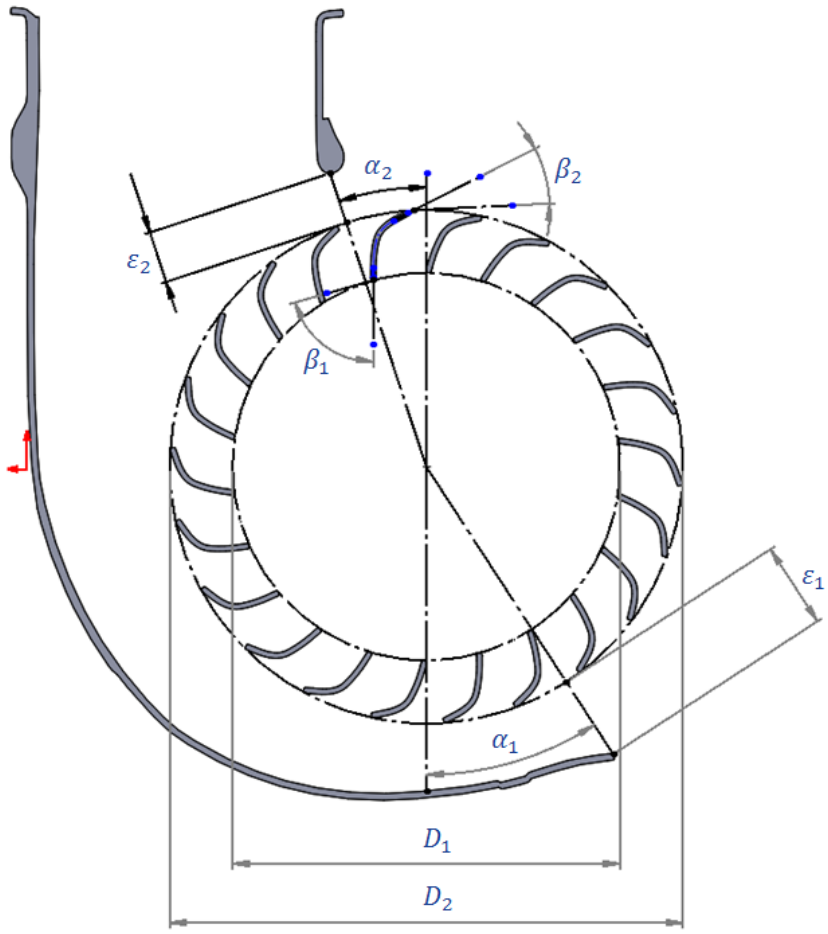

β_2	24.12°
β_1	74.10°
α_1	33.04°
α_2	18.18°
D_1	1.823"
D_2	2.415"
ε_1	0.404"
ε_2	0.244"
D_1/D_2	0.755
ε_1/D_2	16.73%
ε_2/D_2	10.12%

Figure 3-2 Cross-flow fan design parameters

3.1.2. Inlet Geometries and Design Variables

As discussed in Section 2.2.1, the operating point of the fan is defined at the intersection of the fan performance curve and the system curve. Changes in the inlet

geometry affect the fan performance curve; therefore, changing a parameter of the inlet geometry shifts the operating point. Four design variables of the inlet geometry were studied (Figure 3-3). These design variables correspond to geometry features that are easy to manufacture and could still accommodate the cross-flow fan when operating in limited space.

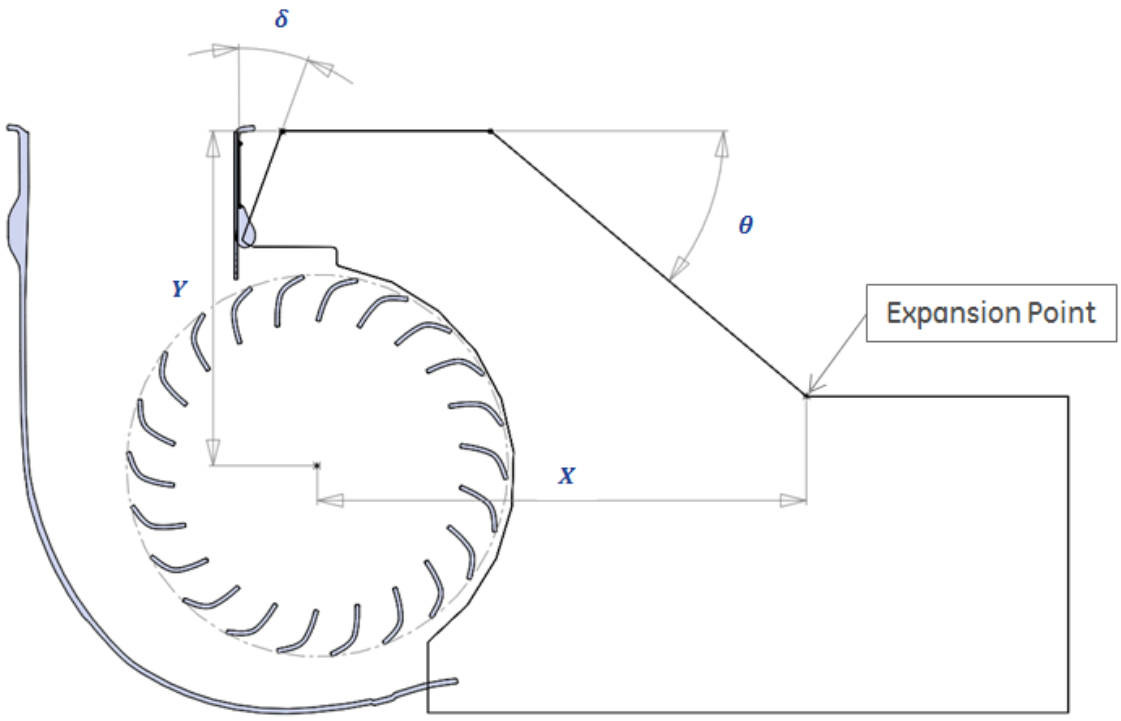

Figure 3-3 Side view of inlet geometry 16 with the design variables

The four design variables were defined as shown in the Figure 3-3. The first design variable (θ) aims to understand the effect produced by changing the expansion angle. This angle is defined from a point of the top wall. This point is located at 0.50" from the vortex wall and the top wall 2.114" from the center of the impeller. This means that when θ is modified, Y, and δ will remain constant, but X changes (see Figure 3-4).

The design variable θ was defined this way because the limited space in a duct application constrains the overall size of the inlet geometry.

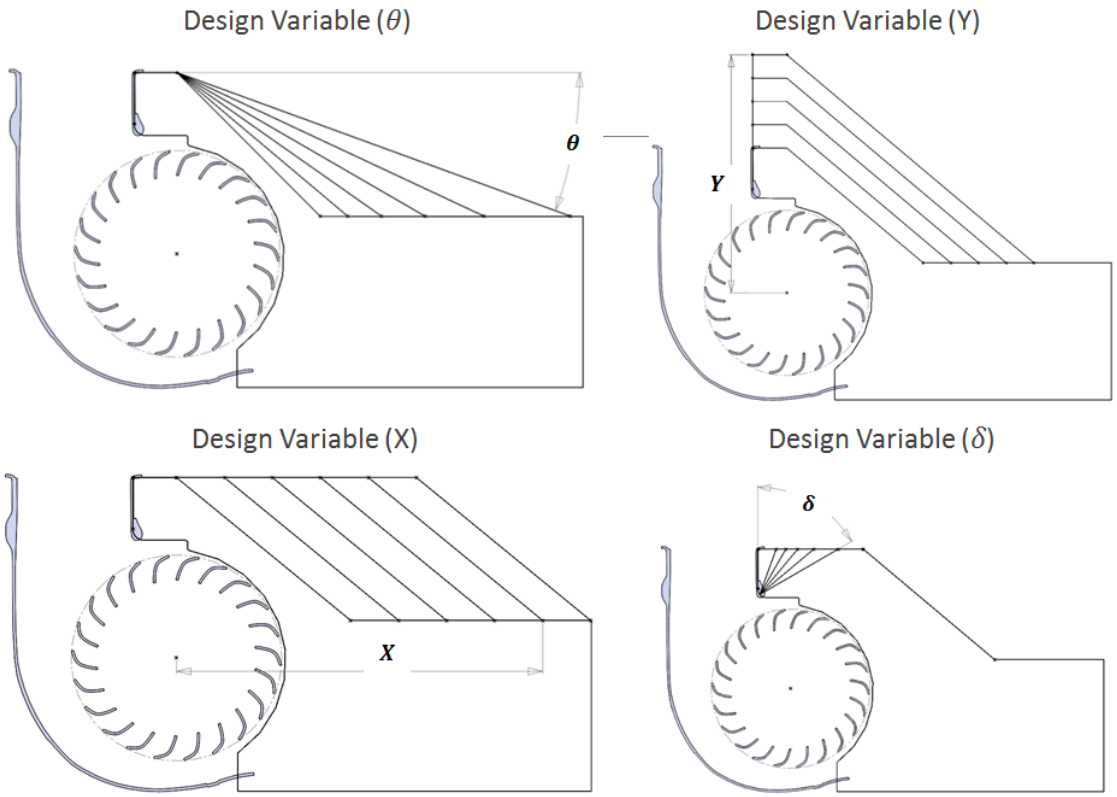

Figure 3-4 Inlet geometries studied for every design variables

The design variable X aims to understand the effect of moving the expansion point away from the fan. In this case, when X is modified, θ, Y, and δ will remain constant. Design variable Y studies the effect of increasing the distance from the fan impeller to the top wall of the inlet geometry. Design variable δ studies the effect of changing the angle of a vane guide near the vortex wall. Table 3-1 shows the values of each design variable for the 21 inlet geometries studied.

Table 3-1 Design variables for each inlet geometry

	Design Variables			
Inlet Geometry	Θ [degrees]	X [inches]	Y [inches]	δ [degrees]
0	25	4.845	2.114	0
1	20	4.605	2.114	0
2	25	3.595	2.114	0
3	30	2.903	2.114	0
4	35	2.394	2.114	0
5	40	1.998	2.114	0
6	45	1.677	2.114	0
7	40	2.548	2.114	0
8	40	3.098	2.114	0
9	40	3.648	2.114	0
10	40	4.198	2.114	0
11	40	4.748	2.114	0
12	40	2.403	2.454	0
13	40	2.808	2.794	0
14	40	3.213	3.134	0
15	40	3.619	3.474	0
16	40	3.098	2.114	20
17	40	3.098	2.114	30
18	40	3.098	2.114	40
19	40	3.098	2.114	50
20	40	3.098	2.114	60

The range of angles studied for the expansion angle θ correspond to the range of angles found in some applications. The range of values used for X and Y were defined around the one impeller diameter requirement suggested by cross-flow fan manufacturers. The range of values used for variable δ corresponds to the range of values studied by Fukutomi and Nakamura (2005).

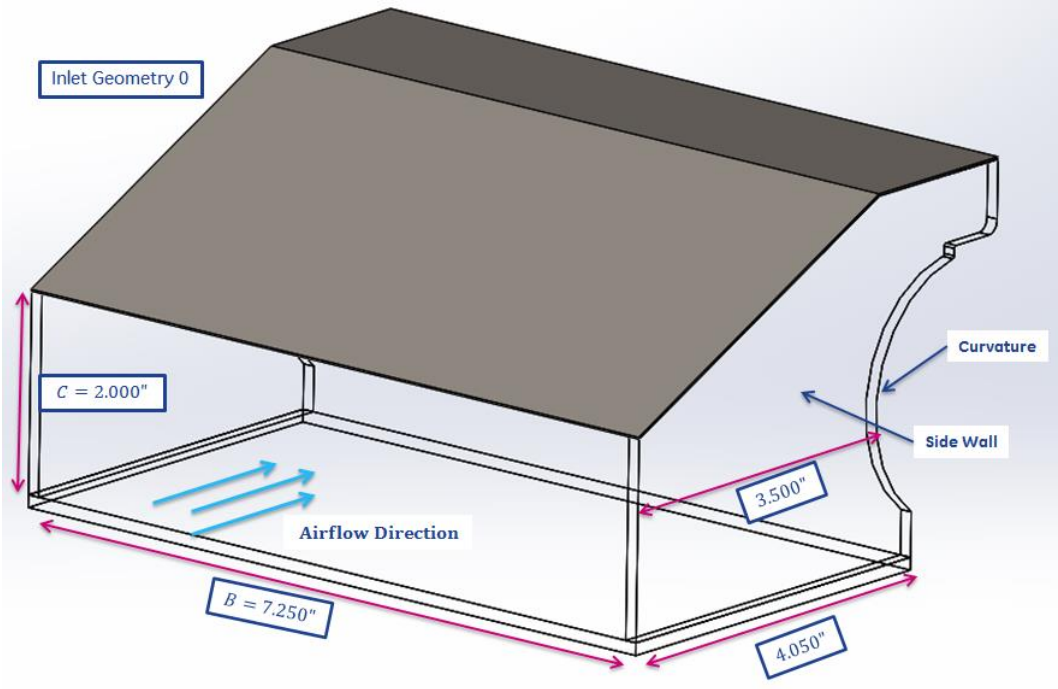

Figure 3-5 Dimensions kept constant for all inlet geometries studied

As shown in Figure 3-5, all the inlet geometries studied have dimensions in common. One of the most critical dimensions is the height $C = 2.00"$ at the entrance of the inlet geometry. This dimension was determined by studying the applications where a cross-flow fan (Section 3.1.1) is typically used. In most cases, a height of about 2" is the maximum space available for the fan inlet. The curvature of the clear side wall was added to match the side wall of the housing of the fan, so that the inlet geometry can be easily attached to the fan and sealed.

3.1.3. Fan-Duct System

Since there should not be an area change in the transition from the duct to the inlet geometry, the inlet duct was made with a height of 2.00" (Figure 3-5). The width "B" of the duct also matches the inlet geometry width shown in Figure 3-5 which corresponds to

the width of the fan. As a result, the inlet duct was designed with a height of 2.00” and a width of 7.25”.

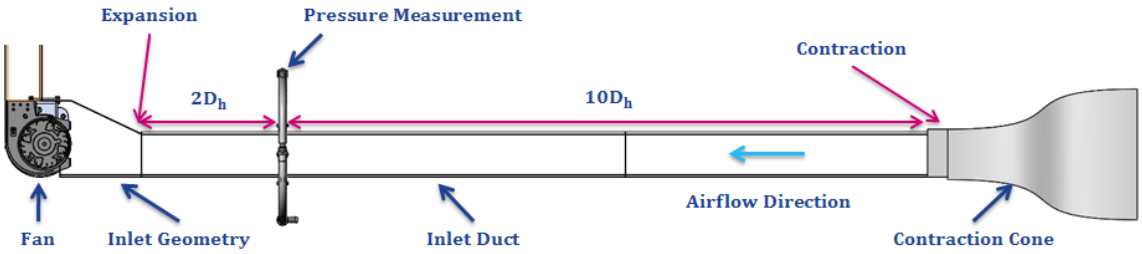

Figure 3-6 CAD model of a section of the test fixture

The length of the ducts was determined using the rule of thumb discussed in Section 2.3 (see Figure 2.10). This rule of thumb says that the location of the pressure measurement should be 10 hydraulic diameters downstream and 2 hydraulic diameters upstream from any change in the duct (see Figure 3-6). With this in mind, the location of the pressure measurements was determined by calculating the hydraulic diameter of the inlet duct ($D_{h\ inlet} = 3.14"$), and used to determine a minimum total duct length ($Length_{min} = 37.62" = 12D_h$). The values shown above are the minimum required length of the inlet duct and the minimum required distance to the measurement location; the actual total inlet duct length was 39” and the pressure taps were made at 32”.

The same process was used to calculate the outlet duct length. The only difference is that the fan discharge geometry is 1.57” by 7.25” resulting in $D_h = 2.58"$. The outlet duct was made to match this outlet geometry. This ensured that there were no losses due to a sudden expansion in the fan outlet. For the outlet duct the minimum length was found to be $Length_{min} = 30.97"$. The outlet duct was made with a total length of 32”.

The design and construction of both the inlet geometries and the ducts was similar. They were modeled using Solidworks and then cut out of extruded clear acrylic sheets using the ILS12.75 laser cutter machine from Universal Laser Systems (Universal Laser Systems, 2011). Clear acrylic has a very smooth wall which will keep friction losses low, and flow visualization could be performed in every section of the duct if necessary.

The use of a laser cutter added its own set of challenges. One of the challenges of using a laser cutter machine instead of traditional manufacturing processes is the kerf. The kerf is the amount of material that is burnt away by the laser cutter. This means that all the part dimensions that are cut with a laser cutter have to be offset by a specific amount. The amount is half the kerf, and the kerf changes depending on the type of material and the material thickness used. For the ducts and inlet geometries, 0.125" thick acrylic was used. The typical kerf for an acrylic sheet with that thickness is 0.007". Using this value, the tap orifice sizes and the duct walls dimensions were adjusted. After accounting for kerf, the precision of the dimensions was within the range of ±0.005".

The duct sections were attached using epoxy, and the edges were covered with Permagum and painters tape to minimize air leakage. Permagum, a sealing gum that can be easily manipulated and adheres to most clean surfaces allowing for use with a wide variety of materials, is commonly used in sealed systems including refrigeration and air-conditioning. Using a smoke pen, the ducts were checked to ensure no air leakage.

Contraction Cone

One of the most important components of an airflow test fixture is the entrance or contraction cone. The contraction cone modifies the entrance conditions by reducing the

losses and stabilizing the flow inside the duct. In this region, the flow accelerates from zero velocity in the surroundings to the velocity inside the duct as it increases dynamic pressure and reduces the static pressure. The loss coefficient for a duct without a contraction cone flow will be in the order of $K_L = 0.90$. By comparison, a notched entrance and a converging entrance have loss coefficients in the range of $K_L = 0.05$ (see Figure 3-7). A contraction cone has features similar to both the notched entrance and the converging entrance.

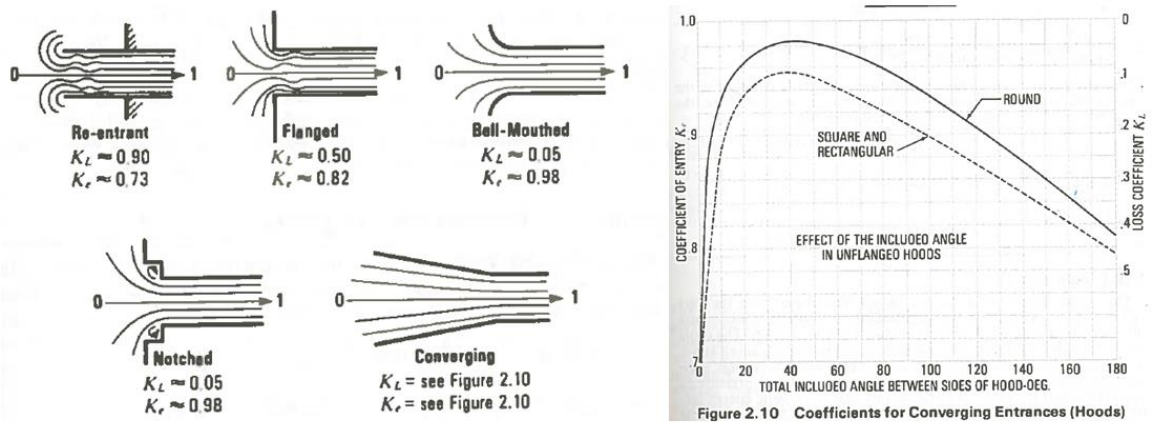

Figure 3-7 Loss coefficients for a set of entrance conditions (Jorgensen, 1983)

Bradshaw and Metha (1979) suggested designing the contraction cone as two segments of a third degree polynomial. In addition, an area ratio between 4 and 6 should be sufficient for airflow velocities expected in this thesis work. "When both of the contraction semi-angles, $\alpha/2$ and $\beta/2$, take the values in the order of 12 degrees, the contraction has a reasonable length and a good fluid dynamic behavior." (Gonzalez Hernandez et al., 2013)

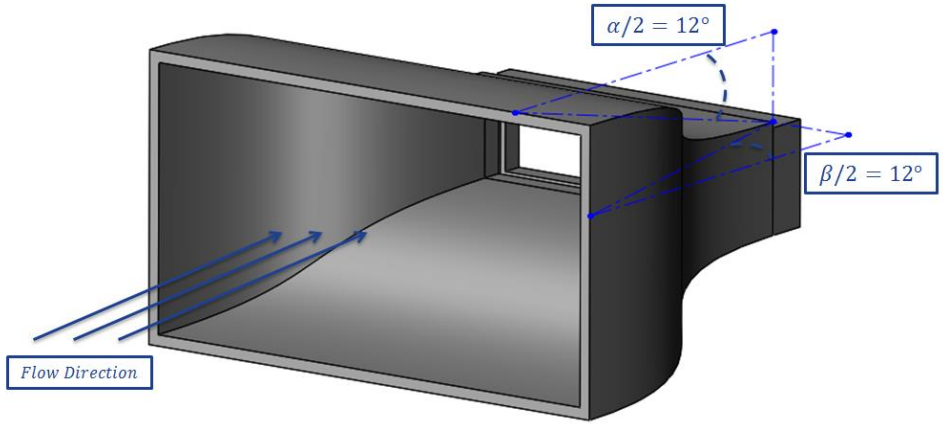

Figure 3-8 Contraction cone showing semi-angles

The contraction cone for the inlet of the fan test setup was designed with an area ratio (A_{in}/A_{out}) of 4.65 and an angle of 12 degrees (see Figure 3-8). The part was designed in Solidworks and built using a Fotus400 3D printer. The Fotus400 prints with a resolution as high as 0.005" per layer. Figure 3-9 shows a side view of the contraction cone (left) and the completed part installed on the duct inlet (right). The contraction cone was attached to the inlet duct using the same method used for the inlet geometries and the duct.

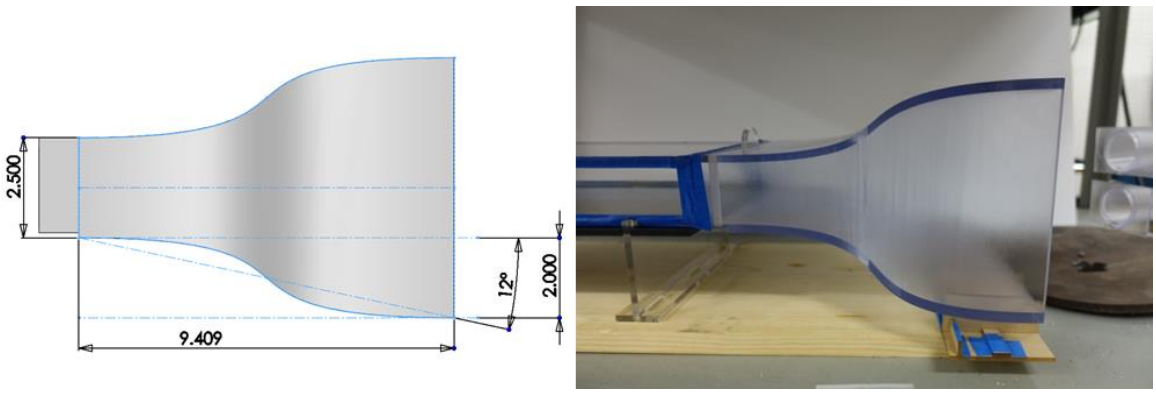

Figure 3-9 Contraction cone: CAD model (left) and 3D printed part (right)

3.1.4. Measurement Systems

As discussed in Section 2.3, a fan performance curve is determined by measuring the static pressure and the volumetric flow rate across the fan. The following sections explain the methodology followed to ensure that accurate pressure measurements were made.

Pressure Drop across the Fan

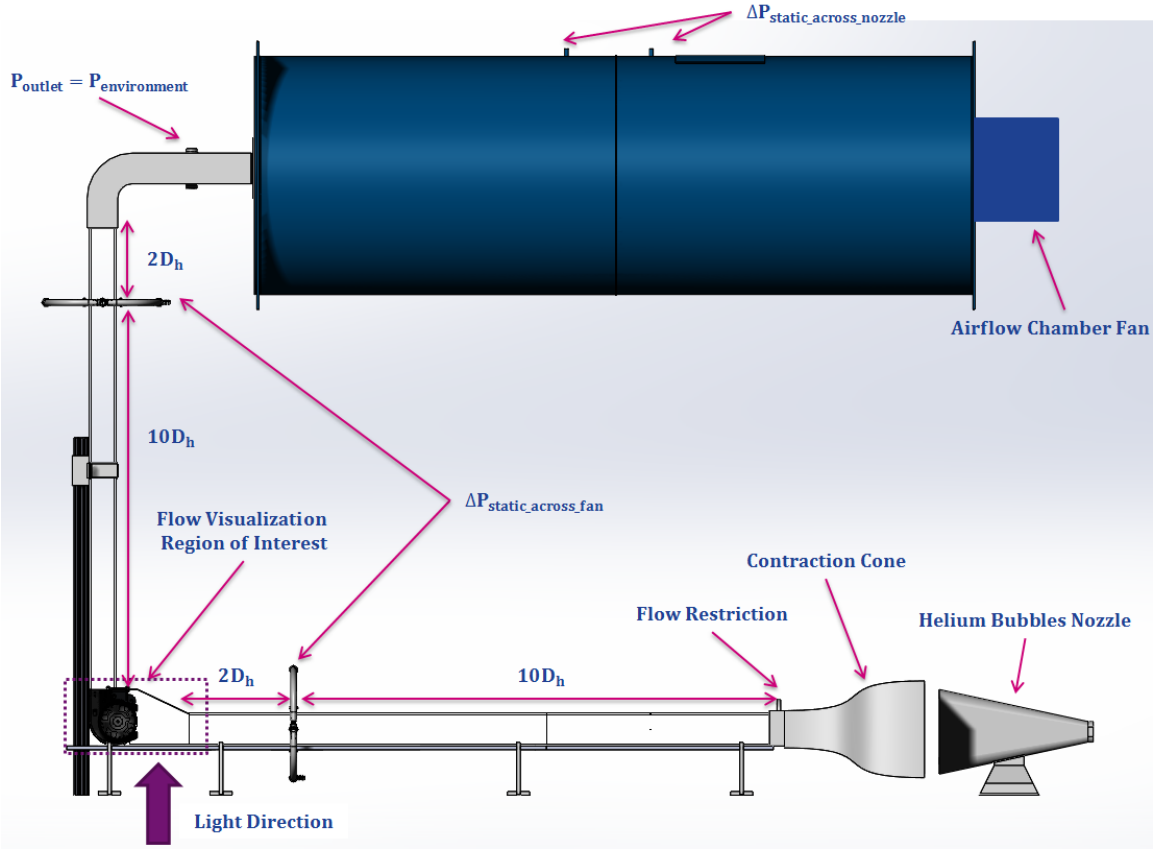

Figure 3-10 Full CAD model of the test fixture

The locations of the pressure measurements across the fan were discussed in Section 3.1.3. This resulted in the static pressure across the fan being measured 7 inches

from the inlet geometry and 26 inches after the fan outlet. Figure 3-10 shows the diagram of the test fixture built.

As discussed in Section 2.3, these locations ensure that the pressure measurement is stable. Nonetheless, finding the right location does not ensure accurate measurements. It is very important to have both the correct design and proper manufacturing of the pressure taps.

Pressure Taps Design and Construction

In Section 2.3 some of the parameters to consider when manufacturing a pressure tap were discussed. One recommended condition was to make the pressure tap orifice smaller than 0.01 duct diameters. For this condition to be valid, the pressure tap orifice diameter in the outlet duct has to be less than 0.026".

A rule of thumb for pressure taps is shown in Figure 3-11. As we can see from Figure 3-11, there is a relationship between the thickness of the wall and the diameter of the orifice. Based on the acrylic wall thickness, the desired tap orifice size is estimated to be in the range from 0.02" to 0.25". A pressure tap orifice diameter of 0.04" was defined, which is within that range, but above the 0.026" as detailed in the previous paragraph. The main reason behind this selection was the barb fittings available to maintain the ratio of the brass fitting inside diameter to orifice diameter closer to 2. By increasing slightly the orifice diameter, the ratio ($D_{fitting}/D_{orifice}$) was reduced from 7.17 to 4.625. This increases the error due to orifice size to about 3%, but reduces the error due to a sudden expansion in the interface between the brass fitting and the orifice.

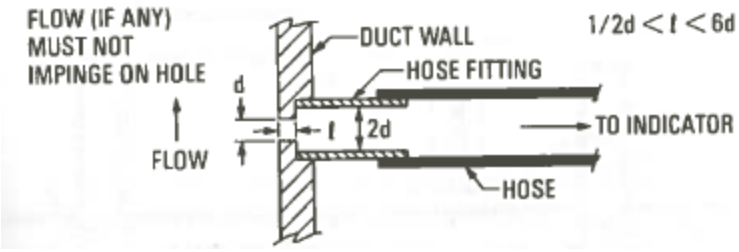

Figure 3-11 Design guidelines for a pressure tap (Jorgensen, 1983)

As discussed in Section 2.3, static pressure taps have to be carefully made to avoid significant sources of error; therefore, a laser cutter machine was used. Laser cutter machines, when used correctly, are a very useful way to reduce manufacturing errors.

Brass adapters, 1/4" barb by 1/8" NPT, were used to connect the pressure hoses to the pressure tap. For each pressure tap, 3" by 3" pieces of acrylic with 1/8" NPT female threads were attached to each of the four orifice walls using a thick layer of epoxy. The brass fittings were installed using Teflon tape to ensure airtight attachment. In addition to carefully locating and correctly designing the pressure taps, a physical way to average the pressure was implemented in order to reduce measurement error, as discussed next.

Physical Average of Pressure

The physical average of the static pressure was made with the purpose of reducing error. It was designed based on a feature of the airflow chamber. The airflow chamber has pressure measurements on each of the four walls around the duct and at the same downstream position. Each location is defined by a brass barb fitting that connects to the manometer by means of a flexible hose. Inside the chamber, each barb is connected to a T-shape brass fitting connecting a hose that goes around that section of the wall (see Figure 3-12). The hose creates a physical average of the static pressure using multiple very small diameter holes perpendicular to the flow, similar to pressure taps.

Figure 3-12 Airflow chamber exterior (left), interior (right)

Following the same principle, four pressure orifices were made at the location previously calculated in Section 3.1.3 in the midline of each wall. Using flexible hoses and barb tees, all taps were connected to a circular hose around the duct that is the average pressure of the four pressure taps (see Figure 3-13). Finally, the digital manometer was connected to the hose to get the average pressure measurement at that duct location. While these series of steps ensure quality pressure measurements, this accounts for only a portion of the information needed to complete the performance and efficiency curves of the fan.

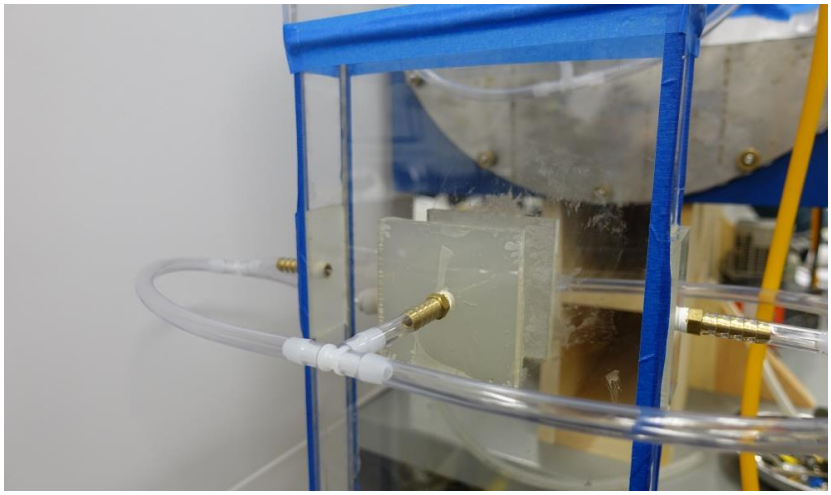

Figure 3-13 Physical average of static pressure on outlet duct

Airflow Measurement

There are many ways of measuring the volumetric flow rate passing through a fan. The classical method uses multiple velocity measurements in specific locations of the duct to get the profile and then integrate over the area. The velocity measurements can be made with either a Pitot tube or a hot-wire anemometer. Other methods use flow through a controlled orifice to estimate the total flow. The critical component of this method is that the orifice has to be manufactured with very good accuracy. If that is the case, then the average flow rate is found by measuring the air temperature, the pressure across the orifice, and the orifice size. Airflow chambers built following the ANSI/AMCA 210 use this method to measure the average flow rate. This section discusses both methods and the reason for selecting the nozzle air-flow chamber method.

Flow Rate Measurement: Hot-Wire Anemometer

Two methods of estimating the flow rate by velocity transverse were discussed in Section 2.3. A comparison test between these methods is here discussed. Figure 3-14 shows the equal area regions and the centroid of each region, which correspond to the Centroids of Equal Areas method.

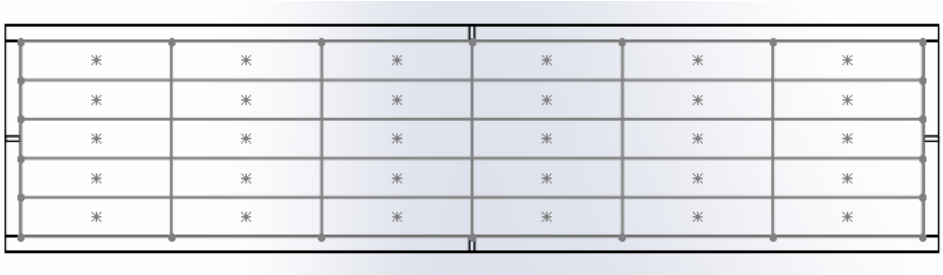

Figure 3-14 Measurement locations for Centroids of Equal Area method

Using a hot-wire anemometer, the air velocity in feet per minute was measured at each one of the locations shown above. The measurements were taken at the end of the outlet duct. Each value was measured by carefully locating the center of the sensing head of the hot-wire anemometer in the centroid of each area and recording the value. The flow rate is calculated by averaging all the local velocities and multiplying it by the total area of the duct cross-section. Table 3-2 shows the values measured at each location and the average velocities calculated.

Table 3-2 Velocity transverse measured with Centroids of Equal Area Method

Centroids of Equal Area Method					
Local Velocity (ft/s)					
537	579	673	688	578	513
562	620	736	685	620	551
562	661	779	744	692	570
564	688	765	736	655	535
535	594	694	672	666	556
Volume Flow Rate (CFM)					
50.09					

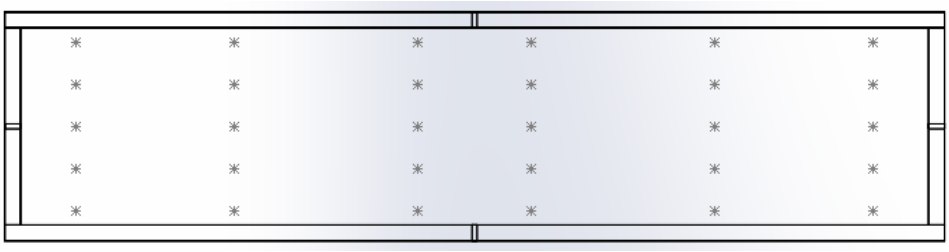

Figure 3-15 Measurement locations for Log-Tchebycheff method

The second method discussed to measure the flow rate by velocity traverses is the Log-Tchebycheff Method. Figure 3-15 shows the locations used for this method. The measurements taken and the average velocities calculated are shown in Table 3-3.

Table 3-3 Velocity transverse measured with Log-Tchebycheff Method

Log-Tchebycheff Method					
Local Velocity (ft/s)					
498	536	582	586	519	503
537	662	734	710	580	519
546	726	784	771	642	514
525	635	746	721	561	509
539	628	720	708	546	499
Volume Flow Rate (CFM)					
48.18					

A significant difference between these methods was found. A comparison between these methods and the airflow chamber measurement showed that both methods can be used to predict the flow with an estimated error of around 4%.

Both of these methods are time consuming. These types of measurements require carefully positioning of the hot-wire anemometer at each location and ensuring that its sensing head is facing into the flow. Hot-wire anemometers are very accurate, with the typical error in the vicinity of 3%, but in most cases a small error in positioning can generate a significant measurement error. For example, an error of 8 degrees will add 1% error, but an error of 16 degrees will add 4% error. Similarly, if 5 out of the 25 measurements are taken just 0.1" away from the centroid location showed in Figure 3-14 and Figure 3-15, the error in the velocity estimation could be around 2%.

Flow Rate Measurement: Airflow Chamber

The second method used to obtain the volumetric flow rate passing through the fan was discussed in Section 2.2.1. The method, which is described in the international standard ANSI/AMCA 210, consists of connecting the fan to an airflow chamber. All the airflow that passes through the fan also passes through the nozzle inside the airflow chamber. As a result, the pressure across the nozzle provides a measurement of the

volumetric flow rate passing through the fan. In this setup, it is important to find an equilibrium position between the airflow passing through the cross-flow fan and the airflow pulled by the airflow chamber fan through the nozzle. This is done by ensuring that the pressure at the duct outlet, before entering in the airflow chamber, is equal to the pressure of the environment. In other words, if a positive pressure is measured at this location, the airflow chamber is not pulling enough air, which is similar to blocking the outlet duct. On the other hand, if the pressure measure is negative, the airflow chamber fan will be pulling more air than required, which will also disturb the operation of the cross-flow fan.

The same operating conditions used for the hot-wire anemometer measurements were used for the airflow chamber measurements. The measurement locations are shown in Figure 3-10. The temperature ($Temp(F)$), the static pressure at the duct outlet (ΔP_{0-3}), and the static pressure across the nozzle (ΔP_{4-5}) measured in this experiment are shown in Table 3-4. Using equations 1 to 6 as described in Section 2.2.1 and the values from Table 3-4, the airflow measured was equal to 50.04 CFM.

Table 3-4 Set of values to calculate flow rate with an airflow chamber

Volumetric Airflow using Airflow Chamber				
Nozzle Diameter (in)	Temp (F)	ΔP4-5 (inH2O)	ΔP0-3 (inH2O)	Volume Flow Rate (CFM)
1.6	72.0	0.853	0.000	50.04

This experiment showed that this airflow chamber measurement method agrees with the Centroids of Equal Areas methods, but it is not as good a match with the Log-Tchebycheff method. The difference in the airflow measured using the Airflow Chamber

and the Centroids of Equal Area method was less than 0.1%. Also, the difference with respect to the Log-Tchebycheff Method was 3.9%. In addition to being a very accurate way of measuring the airflow, this method eliminates any errors due to hot-wire positioning. As a result, the airflow chamber was used for the airflow measurements during all experiments.

Power Supply

Another important step to ensure valid data is connecting the fan to a controlled power supply. The fan performance is directly related to the motor performance. If the voltage supplied to the fan increases or decreases, the fan curve will shift from its original position. In other words, the fan behavior is directly related to the power supplied to the motor; therefore, the voltage is a variable that has to be controlled in order to get reliable data from the test. The fan was connected to a Kikusui PCR 4000W power supply. This power supply maintains the voltage load with a tolerance of ±0.15V. Another advantage of the Kikusui PCR 4000W is that it measures the average power with an accuracy of ±1%.

3.2. Fan Characterization Methodology

3.2.1. Pressure and Volumetric Flow Rate Measurement

For all pressure measurements two Fluke 922 digital manometers were used (see Figure 3-16). These manometers measure the air pressure with a resolution of $0.001\ inH_2O$ and an accuracy of $\pm 1\%$ and the temperature with a resolution of $0.1°F$ and an accuracy of $\pm 1\%$ (Fluke Corporation, 2006).

Figure 3-16 Fluke 922 digital manometer

The first measurement is between measurement location 3 and the ambient pressure (see Figure 3-17). This pressure difference needs to be zero before any other pressure measurement is made. Reaching this equilibrium requires adjusting the speed of the airflow chamber fan to match the airflow discharged by the cross-flow fan. Once this value reaches zero, the static pressure across the fan is measured by connecting the manometer to measurement locations 1 and 2. The pressure across 4 and 5 and the temperature of the air is measured using the second manometer. The airflow was calculated from the static pressure and the air temperature measured across the nozzle in the airflow chamber using the method described in Section 2.2.1. The temperature is required to determine the density of the air.

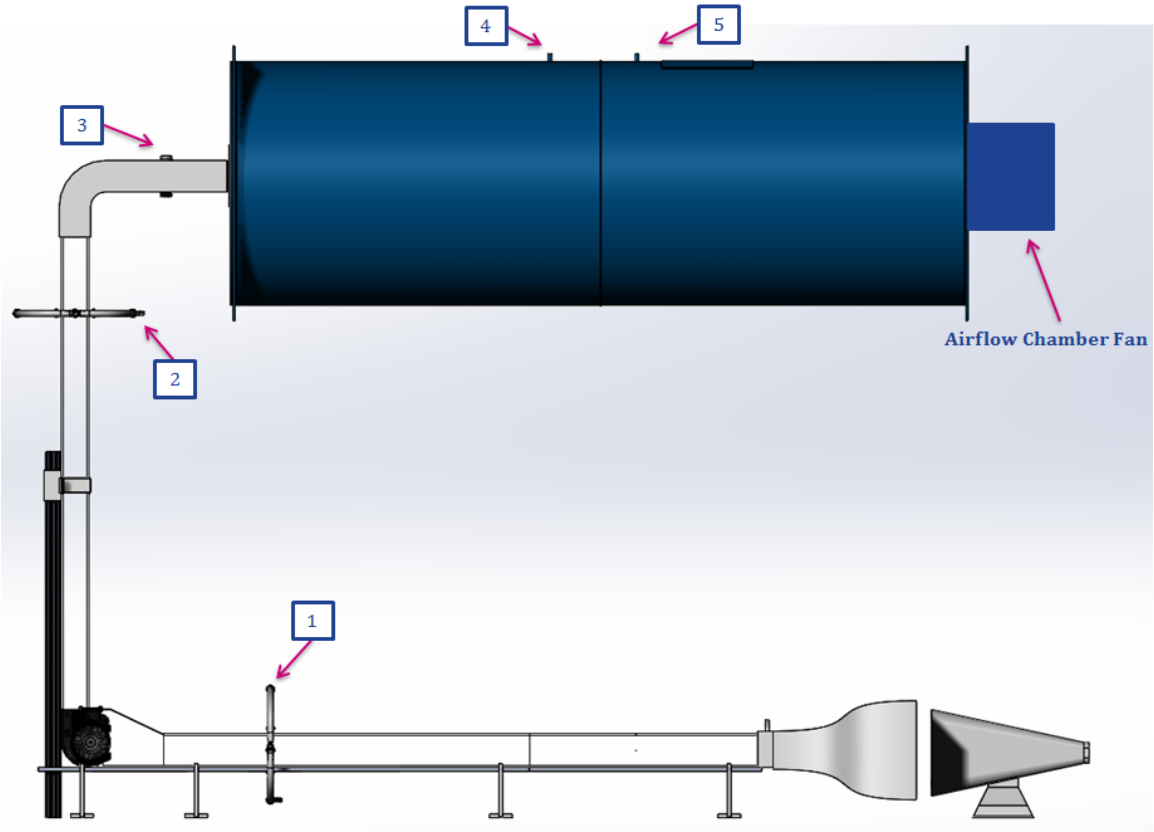

Figure 3-17 Static pressure measurement locations

3.2.2. Fan Speed Measurement

The fan speed, in revolutions per minute (RPM), was measured using a hand held, non-contact tachometer. The tachometer used was a CDT-1000HD. This type of tachometer has an accuracy of 0.02% with a resolution of 0.01 RPM (Electromatic Equipment Co., Inc., 2007). Although this is a high accuracy tachometer, during normal operation the fan speed varies due to the nature of airflow turbulence. The typical reading variation was ±20 RPM for a fan speeds between 2500 RPM and 3100 RPM (< 2% error). As a result, the fan speed was determined by averaging three consecutive readings.

Non-contact tachometers are useful because they do not introduce friction to the system and can be used with just a few minor changes to the fan housing. The left side of

the fan housing was replaced by an optically clear piece of acrylic. In addition, the side of the fan impeller was painted black and a small square piece of reflective tape was attached to it. These modifications allowed increasing the accuracy of the measurements while making it easy to get a value without disrupting the fan operation. Figure 3-18 shows the fan used for the experiment and the modifications made to it.

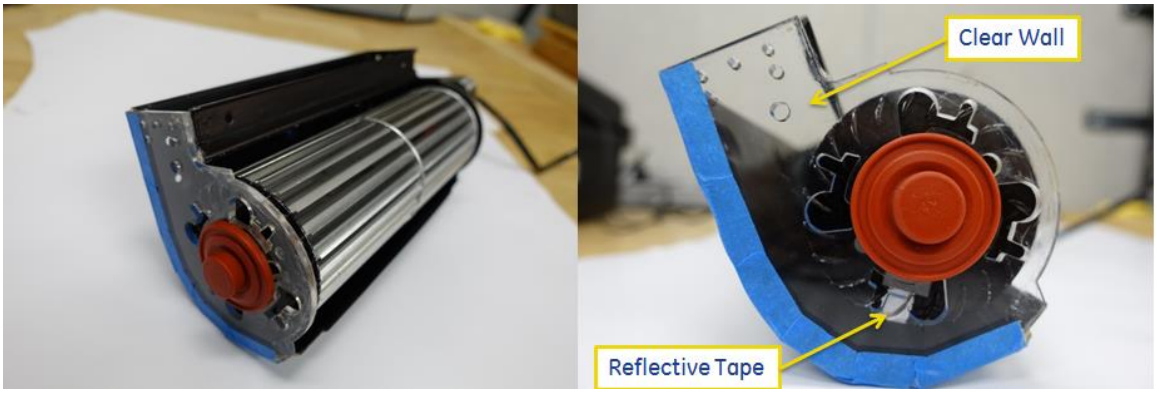

Figure 3-18 Cross-flow fan used in the experiment

3.2.3. Fan Performance and Efficiency Curves

As discussed in Section 2.2, a fan performance curve is generated by at least eight point measurements going from zero flow condition to maximum flow condition. Changing the flow condition typically consists of adding restrictions to the airflow chamber exit, or to the suction region of the fan. Since one of the objectives is to measure the flow field in the inlet geometry, the restrictions were added to the suction region. This ensures that the flow field will behave similar to the way it behaves under typical operation conditions for this fan-duct system. Figure 3-10 on page 36 shows the location of the flow restriction just downstream of the contraction cone. Following the rule of thumb for static pressure measurements, the restriction was placed ten hydraulic diameters upstream of the pressure tap locations.

For each measurement point the methodology described in Section 3.2.1 for pressure and volumetric flow rate measurement was completed. The first performance curve measured with the fixture was the fan without any inlet geometry. This specific case does not require inlet geometry; therefore, the contraction cone, the inlet duct and the fan inlet geometry were removed to measure the characteristics curve of the fan. The flow restrictions required to measure the fan curve from zero flow to maximum flow were added to airflow chamber fan as suggested by the ANSI/AMCA Standard 210 (2000). Figure 3-19 shows the static pressure and the static efficiency for the cross-flow fan used in this research work.

As discussed in Section 2.2.1, the efficiency is calculated from Equation 7 where $\dot{P}_{out}$ is determined from Equation 8, and $\dot{P}_{in}$ is measured experimentally. The difference between the total efficiency η_T and the static efficiency η_{static} is that the latter only depends on the static pressure. As a result, Equation 7 becomes $\eta_{static} = \frac{\Delta P_{static} * \dot{Q}}{\dot{P}_{in}}$. Since the fan is a dynamic system, the static pressure across the fan is less than or equal to the total pressure across the fan ($\Delta P_{total} = \Delta P_{static} + \Delta P_{dynamic}$). As a result, the static efficiency is smaller than the real total efficiency of the fan, particularly at high volumetric flow rates. Since the dynamic pressure is typically less than 20% of the total pressure and it can be really variable depending on the location of the measurement, it is common practice to use the static efficiency of the fan instead of the total efficiency.

The performance curve of the fan shows a steep drop in static pressure starting at about 70 CFM. This is a very interesting characteristic for this specific fan. It was also noticed at high volumetric flow rates that reaching the equilibrium point between the fan and the airflow chamber was very difficult. As a result, that operating region of the fan

was avoided when testing different inlet geometries. The measurements were limited to the typical operating range of the fan which is between 10 CFM and 65 CFM.

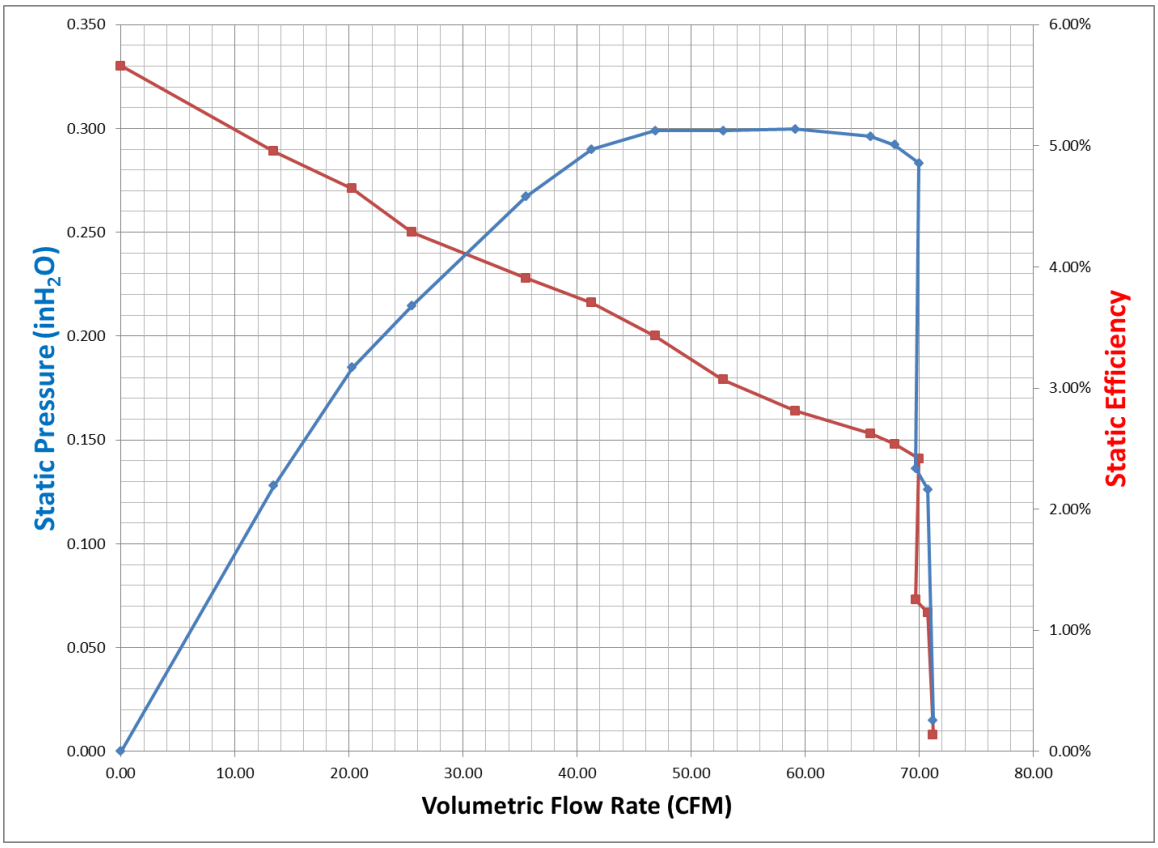

Figure 3-19 Static performance and efficiency curves for the cross-flow fan

A good way of comparing the performance and efficiency of the fan is by using dimensionless coefficients. In Section 2.2.2 the flow coefficient and the pressure coefficient were discussed, and Equations 9 and 10 were used to calculate the flow coefficient (ϕ) and the pressure coefficient (ψ). Figure 3-20 shows the performance and efficiency curves using dimensionless coefficients. This is valuable information when comparing different fans, but when comparing different inlet geometries using one specific fan the static pressure performance curve is the more convenient method.

Nonetheless, performance curves using dimensionless coefficients are provided in Appendix C with the purpose of comparing different fans in future studies.

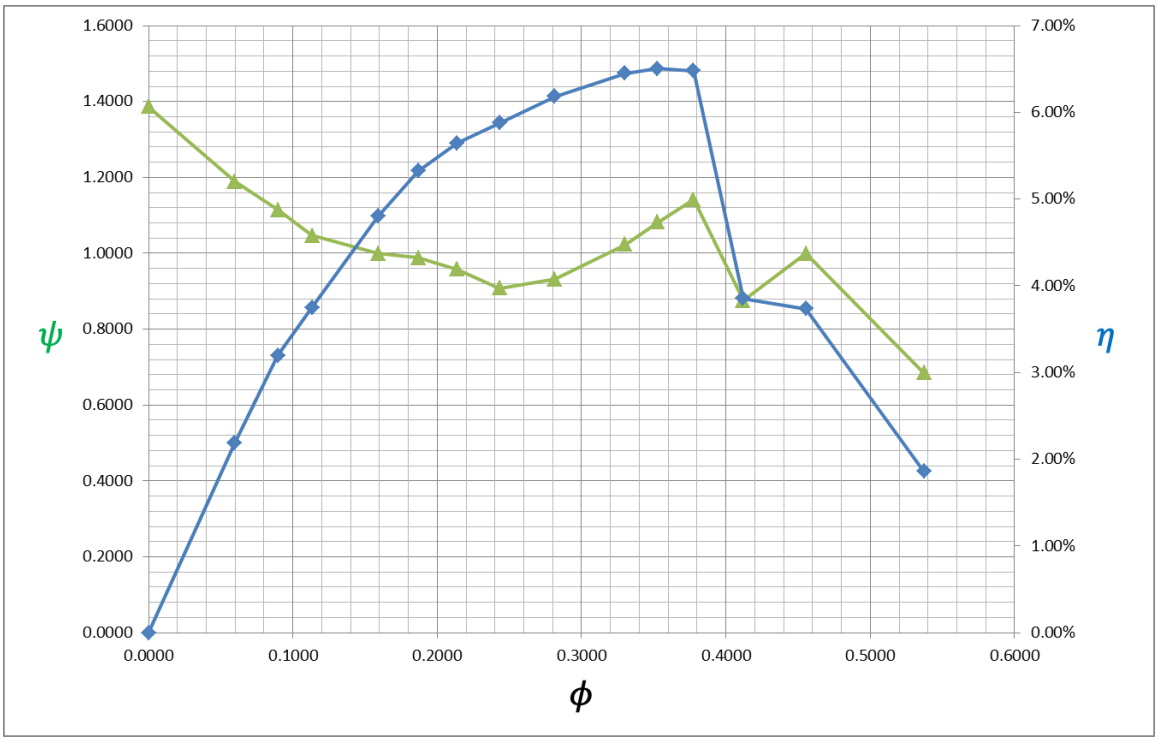

Figure 3-20 Dimensionless performance and efficiency curves

3.2.4. Flow Rate Comparison

All the visualization studies discussed in Section 2.1 used a constant impeller speed condition. Those studies focused on either characterizing the fan parameters or optimizing the fan performance; therefore, they removed the effect of the motor curve by keeping the fan speed constant. This allowed the identification of the best parameters under ideal conditions and allowed them to improve the fan impeller. However, in normal operating conditions the fan speed changes depending on the torque produced by the resistance the airflow puts on the impeller. The speed of the fan is the result of the torque applied in the impeller and the torque-speed curve of the motor. In other words, the

aerodynamics of the flow-field directly affects the speed of the fan. As a result, the fan speed was not held constant in this study and instead, three specific volumetric flow rates were held constant. These constant flow rate conditions simplify the comparison between the different inlet geometries. For each case studied measurements were made at 25, 40 and 55 CFM.

To reach these constant volumetric flow rate points, it is required to find equilibrium between the airflow restriction and the power supplied to the airflow chamber fan while the static pressure at the duct outlet (ΔP_{0-3}) is equal to zero. Since the flow rate is measured with the airflow chamber, a target pressure across the nozzle was calculated to facilitate the process of finding each equilibrium point. These values were calculated for the airflow chamber used, with a nozzle diameter of 1.6", and an air temperature of 72°F. The target pressure across the nozzle (ΔP_{4-5}) that correspond to 25, 40 and 55 CFM are $0.218, 0.549,$ and 1.030 inH_2O respectively.

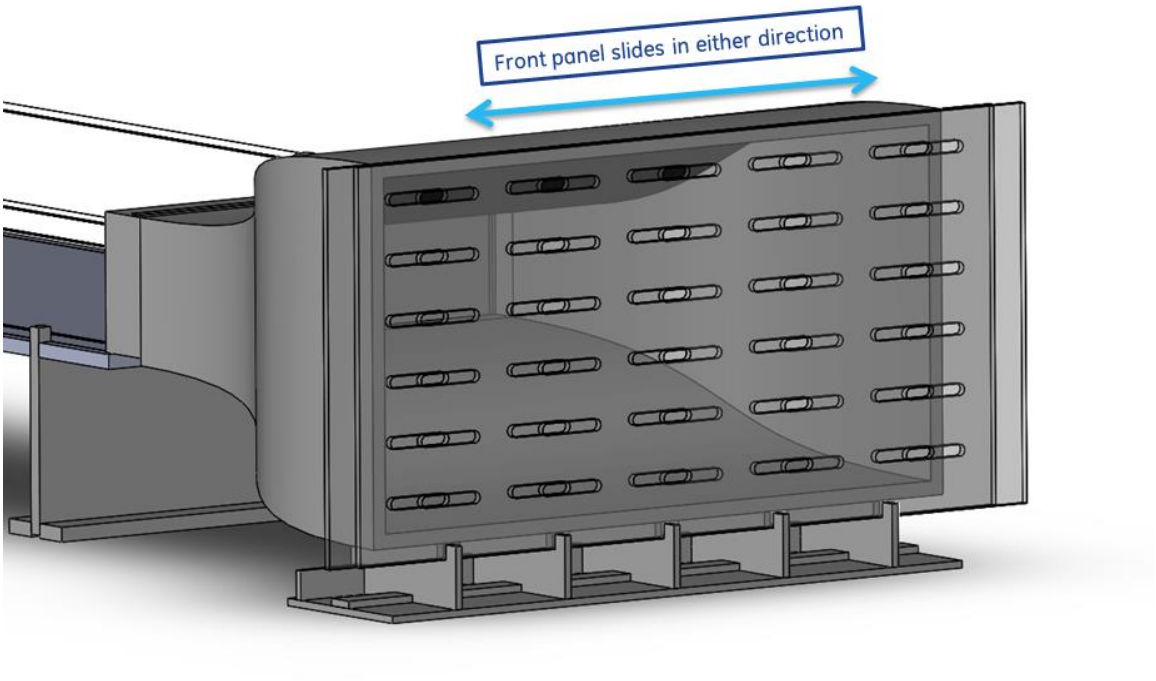

Figure 3-21 Airflow restriction for constant flow rate measurements

As shown in Figure 3-21, the duct restriction designed consists of two identical panels with an array of slotted holes. The airflow is regulated by sliding one of the panels relative to the other. This method is similar to the method to measure the performance curve; the difference is that usually it is more sensitive and it may take longer to find equilibrium.

3.2.5. Measurement Uncertainty

Uncertainties were calculated following the methodology discussed in Appendix E of the ANSI/AMCA 210 (2000). The measurement uncertainties of the nozzle discharge coefficient e_C and the area e_A of the airflow chamber, as discussed in Section 2.2.1, were assumed to be equal to those provided in the standard (see Table 3-5). Other measurement uncertainties were needed such as the fan speed $e_N = 2\%$ and the

barometric pressure $e_b = 1\%$. The standard proposes an equation to calculate the uncertainty of the air volume e_V that requires the measurement of the dry-bulb and wet-bulb temperatures. However, the temperature was measured with a Fluke 922 digital manometer that provides a temperature reading with an uncertainty of $e_{Temp} = 1\%$. As a result, the uncertainty of the air volume was assumed as $e_V = 1\%$ which is significantly higher than the actual value. The uncertainty of the pressure measurement for determining the flow rate e_f and the pressure measurement for determining the fan pressure e_g were calculated using the equations given in the ANSI/AMCA Standard (ANSI/AMCA, 2000). These equations assume that the tolerance is 1% of the maximum flow rate Q_{max} or maximum pressure P_{max} measured during the experiment.

Table 3-5 Measurement and combined uncertainties

Measurement and Combined Uncertainties											
Q_{max} (CFM)	P_{max} (inH2O)	e_b	e_V	e_A	e_N	e_C	e_f	e_g	e_ρ	e_Q	e_P
71.22	0.33	1.00%	1.00%	0.50%	2.00%	1.20%	1.39%	2.55%	1.73%	2.63%	5.05%

The combined uncertainties of the density e_ρ, the airflow rate e_Q, and the fan pressure e_P were found using equations Eq. E-13, Eq. E-15A, and Eq. E-16A respectively (ANSI/AMCA, 2000). As shown in Table 3-5, the maximum uncertainty in the airflow rate was ±2.63% and the maximum uncertainty in the fan pressure was 5.05%. As shown in Figure 3-22, the resultant upper and lower boundaries follow closely the fan characteristic curve measure.

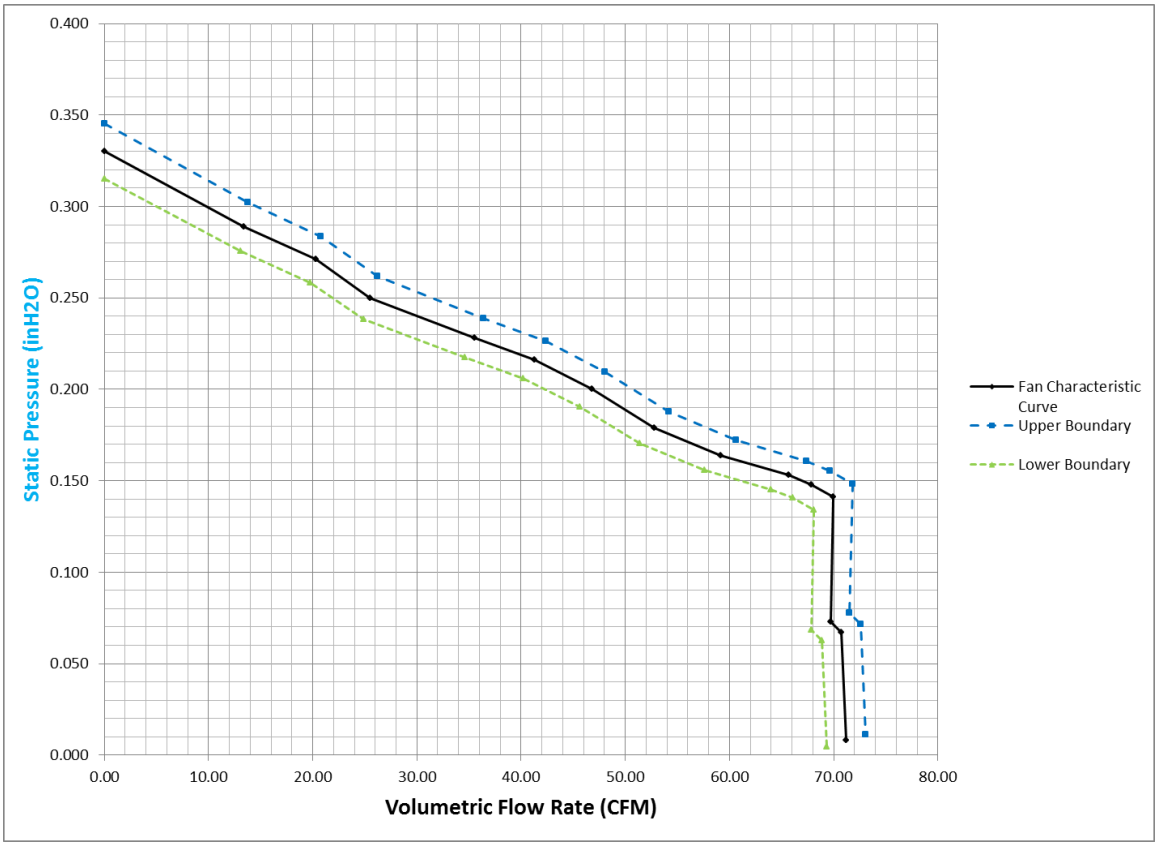

Figure 3-22 Fan characteristic curve with upper and lower uncertainty curves

3.3. Airflow Visualization

For this study a low cost PTV type system was developed to measure the flow field velocity in the suction region of a cross-flow fan. The system developed uses helium filled bubbles as tracers, a sheet of light made with white LEDs as illumination system, and the Sony RX100 VI CMOS camera as recording device. The measurements are made using a Matlab program that was developed by the author. This program uses a Kalman Filter multi-object tracker algorithm as described in Section 2.4.2. The tracers are generated with the Helium Bubble Generator Console Model 5 (Figure 3-23).

3.3.1. Helium Bubble Generator

The Helium Bubble Generator Console Model 5 is manufactured and distributed by the company Sage Action INC. This machine creates neutrally buoyant helium bubbles that allow airflow visualization. The bubbles have an average lifetime of 2 minutes, providing enough time for flow visualization. This machine produces up to 400 bubbles, of about 0.04” diameter, per second; therefore, it produces sufficient bubble density for a variety of airflow visualization applications, including the study of fans and near fan regions, HVAC design, and many types of studies in wind tunnels. The diameter of the neutrally buoyant helium bubbles can be adjusted within the range of 0.03” to 0.18” (Fu et al., 2015).

Figure 3-23 Helium Bubble Generator Model 5 (Sage Action, 2016)

This machine uses three things to generate the bubbles: compressed air, SAI 1035 or Bubble Fluid Solution (BFS), and helium. The air and the helium are externally supplied while the BFS is supplied internally through a small PVC tank which is filled

and closed before using the machine. The air is supplied through a ¼" female quick connect fitting at controlled pressure in the range of 30 to 60 psi. Similarly, the helium is supplied through a ¼" female quick connect fitting at a controlled pressure of 20 psi. Neutrally buoyant helium bubbles are generated by supplying the right amount of helium, air and BFS. Three micro-metering valves (see Figure 3-24) are used to regulate the flow of each constituent to the plug-in head. The right combination is determined experimentally (see Section 3.3.5) and will change if the pressure of air or helium changes.

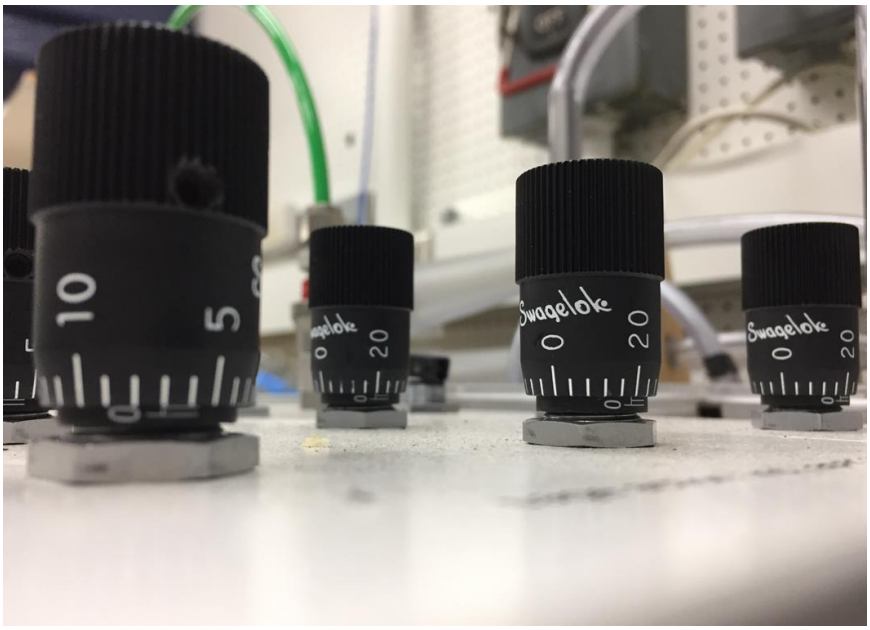

Figure 3-24 Helium Bubble Generator: micro-metering valves

The bubbles are generated inside the plug-in heads. The plug-in heads are a concentric arrangement of two stainless steel hypodermic tubes, one inside the other, attached in a cantilever fashion to a cylindrical manifold. The helium passes through the smaller tube when it comes out gets surrounded by the BFS, which travels through the channel between both tubes, forming a bubble. A larger jet of air then pushes the bubbles

out of the plug-in head and into the Mini-Vortex Filter. Once in the filter, the bubbles progress into fast rotational motion around the Mini-Vortex Filter Axis. The bubbles that are too heavy will separate during motion allowing only the neutrally buoyant and buoyant bubbles to be released into the hose. In other words, the neutrally buoyant bubbles and the bubbles lighter than air are released into the test section.

A hose connects the Mini-Vortex Filter to an expansion nozzle that reduces the bubble stream velocity to that of the environment. The two expansion hoses were placed in front of the contraction cone on the test fixture (see Figure 3-10). As a result, the bubbles were released at almost zero velocity in the region where the air starts accelerating into the contraction cone. The bubbles pass through the inlet duct, through the inlet geometry and into the fan.

The helium bubbles generated with this machine "have been shown to trace airflow patterns at speeds as high as 200 ft/s" (Sage Action, Inc., 2008). For this specific study, and for this cross-flow fan, the local air speed is less than 25 ft/s. As a result, for the air velocities in this study, the helium bubbles should be high quality tracers.

3.3.2. Illumination and Background

An important aspect of flow visualization is illumination and background. This combination of illumination and background is what produces the contrast necessary to observe the flow in the region of study. In the case of helium bubbles, it is even more important due to the transparent appearance, almost similar to glass. Dark field lighting is commonly used for glass photography because it perfectly defines the edges of clear objects such as helium bubbles. A dark field light is a light source that is illuminating the

region of interest with an incidence range between 45° to 90° angle. For this specific study, the light was placed at a 90° angle. An acrylic sheet painted using flat black paint was used as background. Similarly, the fan housing was painted flat black to reduce reflections that introduce errors during post-processing.

It has become common practice to use high power laser sheets in flow visualization testing. However, high power lasers can be dangerous if misused and they tend to be very expensive. Laser sheets are thinner than the average diameter of a helium bubble. This is particularly problematic for PTV because the laser sheet does not illuminate the full bubble. Instead, it reflects just a portion of the helium bubble. On the other hand, dark field LED lights provide a wider light sheet that can fully illuminate the helium bubbles. For these reasons a light sheet using white LED lights was designed.

LED Light Sheet Design

The objective of the illumination was to clearly define the helium bubbles that are passing through a plane in the inlet geometry, while keeping the background dark and free of noise. White LED strips were used to design a light box that can effectively produce a light sheet of white light. Lasers use optical lenses to focus the light into a point or to create a sheet of light. Lenses are expensive, especially for this kind of application that requires a customized lens. A more traditional way of dealing with illumination issues is controlling the field of view of LED lighting with geometry. Figure 3-25 shows the LED strip position with respect to the rectangular opening on the box and the projected field of view of the light.

As seen in Figure 3-25, the light sheet is defined by three dimensions: the distance from the LED lights to the rectangular opening, the width of the box opening, and LED

light diameter. The LED lights have a diameter of 0.25” and cannot be changed without damaging the light functionality. The maximum distance from the LED to the box opening is limited by the distance from the floor to the inlet geometry which in this case was set at 3”. The box design is simple, with a rectangular box containing the LEDs and a top piece that regulates the box opening. The rectangular box has a length of 5.75”, a width of 0.5”, and a height of 3”. The top piece has an opening with the same length of the box and 0.2” wide. Both parts were 3D printed.

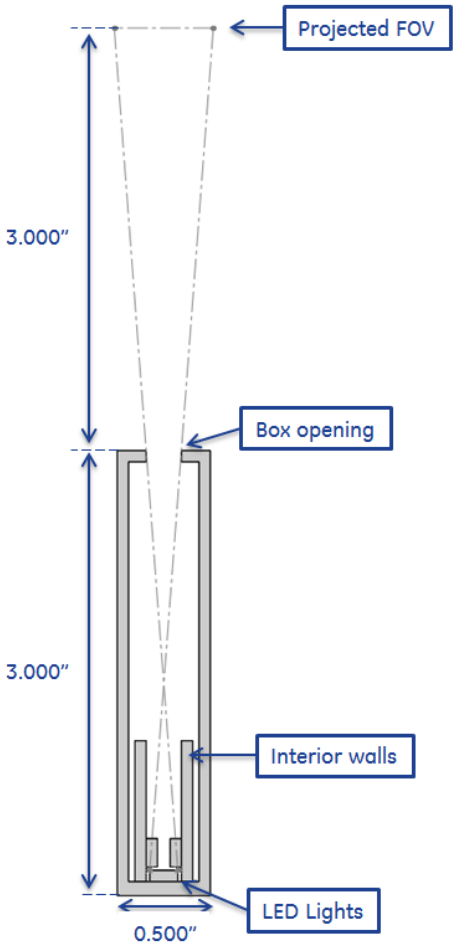

Figure 3-25 Projected field of view of the LED light sheet (CAD Model)

Even though the overall width of the box was 0.5” two internal walls were added to constrain the LED strip (see Figure 3-25). This not only reduced the amount of light that was reflected from the interior face of the box walls, but also it concentrated the light in a smaller volume increasing its intensity. In addition, a total of three LED strips were used inside the box, one on the bottom of the box and one on each side wall. This combination increased the lumens considerably. Using LED lights provide multiple advantages. LED strips are easily installed to any surface using common adhesives. They are light weight and produce bright clean light with only 12V.

While easy to manufacture and cost effective, this illumination method is not error free. As we can see from Figure 3-25, the light sheet gets wider as it gets farther away from the box. This issue can be controlled by moving the LED lights father away from the opening, but increasing the box size is not always possible due to setup constraints. Another way of reducing the error is by making the opening smaller, but this will reduce the light sheet width and thereby reduce the visibility of the helium bubbles. The light box designed, manufactured, and used for this study produces a light sheet that is about two times wider on the top of the duct than on the bottom of it. Although the error introduced from this could be significant, it can be accounted for using a combination of proper light location and post processing techniques.

The advantage of laser sheets is that they show an exact plane. If a particle’s motion is tridimensional, the particle will be visible only as it passes through the sheet. In comparison, in a widening light sheet particles could travel in or out of the plane of interest, but they will still be visualized as 2D flow as long as they remain inside the area illuminated. However, if the airflow is stable and primarily two-dimensional in the

illuminated region, the error introduced by a widening light sheet will be insignificant. The following analysis was completed to determine the light sheet location where the flow behavior was mostly two-dimensional.

Light Location Analysis

As explained in the previous section, it is important that the light is placed in a stable region where the fluid travels mostly two-dimensionally. A good way to determine the stability of the flow in the plane is by running a qualitative test using flow visualization. Such a test was completed using Inlet Geometry 0 at 55 CFM (Table 3-1). In the test the light was placed at three locations. Figure 3-26 shows the three locations at which the light was placed.

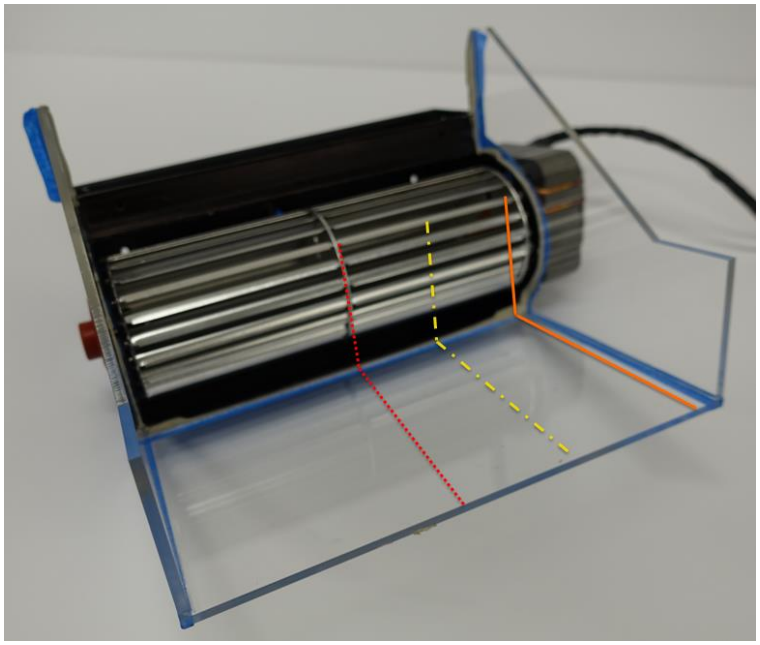

Figure 3-26 Light analysis locations

The test results show that the less stable region is the 2D plane in the center of the duct. Although less turbulent, similar unstable results were found while observing the

flow in the 2D plane near the wall (orange solid line). The 2D plane where the flow observed had a behavior closest to two-dimensional flow is the plane shown in yellow dot-dash line in Figure 3-26. The light was placed at this location for all the visualizations performed in this study.

3.3.3. High Speed Video

A critical step of any type of flow visualization is having clear sight to observe or to record the flow. While observing the airflow can provide relevant information, recording the flow is necessary to obtain more detailed analysis of the flow. As a result, recording a video of the experiment and using software to post-process has become common practice. For example, PIV, which is one of the most common methods, uses high-speed cameras to record the flow and then uses software to analyze the video to produce a map of the 2D or 3D flow in the region. Typically, for this type of experiment, a high-speed video camera is needed.

The need for high speed recordings used to be one of the limitations of flow visualization, but high-speed video cameras have become common in today's world. A clear example of this is the IPhone 6, which allows recording slow motion videos of up to 240 frames per second. In comparison, the frame rate of movies and television in the US is 30 frames per second and 4K high definition movies use 60 frames per second. This means that a slow-motion video recorded using the IPhone 6 has eight times more frames than a regular video. However, depending on the flow velocity 60 frames per second may not be enough for proper visualization. To determine the proper frame rate the following analysis was completed.

Based on the fan performance curve shown in Figure 3-19, the maximum volumetric flow rate is around 70 CFM. The cross-sectional area of the inlet duct is $0.101 ft^2$; therefore, the average velocity of the air is $V_{average} = 138.61 \frac{in}{sec}$. Since a video made using the IPhone 6 Slow Motion Camera has 240 frames per second, the average displacement of each bubble can be estimated as $S_{average} = 0.577 \frac{in}{frame}$. This distance is really significant since the total length of the inlet is about 3". Figure 3-27 shows four consecutive frames of a slow motion video taken with the IPhone 6 Slow Motion Camera. The video was taken at 42 CFM and a fan speed of about 1000 RPM. At these conditions the average distance traveled is $0.346 \frac{in}{frame}$.

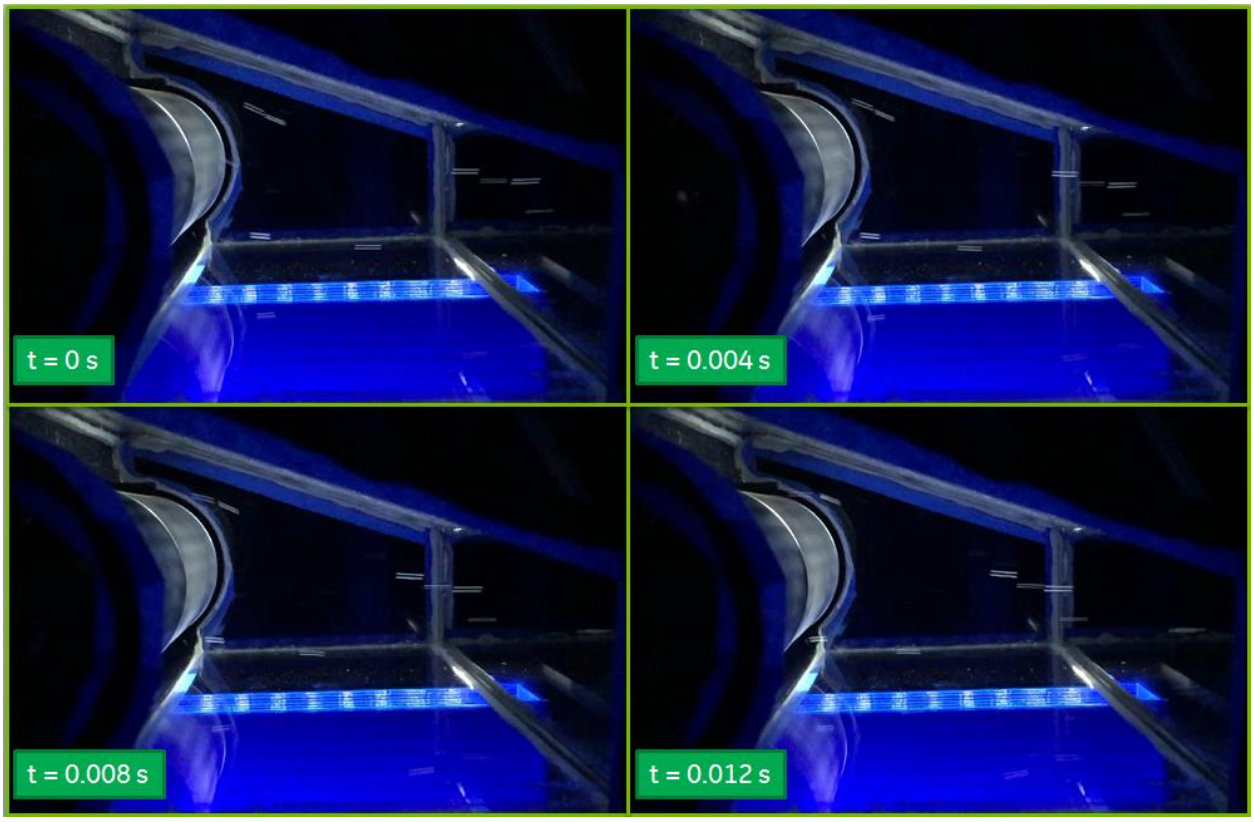

Figure 3-27 Four consecutive video frames (Iphone 6 @240 fps)

As shown in Figure 3-27, each bubble is depicted by the camera as a line, and while this does not interfere with tracking the path made by the bubble, it does interfere with calculating the position and the velocity. As a result, using this camera it is impossible to measure the flow field; therefore, another camera with higher frame rate was used for recording the videos.

The Sony RX100 IV is an affordable camera priced around $1000 in consumer electronics stores. It has a higher resolution than the IPhone and allows recording high speed videos up to 960 frames per second or four times faster. This means that the distance traveled under the same volumetric airflow of 42 CFM will be only about $0.086\ \frac{in}{frame}$ and $0.144\ \frac{in}{frame}$ at 70 CFM. In comparison, the diameter of the helium bubbles lays in the range from 0.03" to 0.18". This resolution allows tracking the neutrally-buoyant helium bubbles with precision because, on average, the bubble should only travel a distance equal to its own diameter from frame to frame. Figure 3-28 shows four consecutives frames using the same inlet geometry 1, volumetric airflow, and fan speed as used in Figure 3-27. The bubbles are visualized as perfectly round, and the distance traveled between frames is very small.

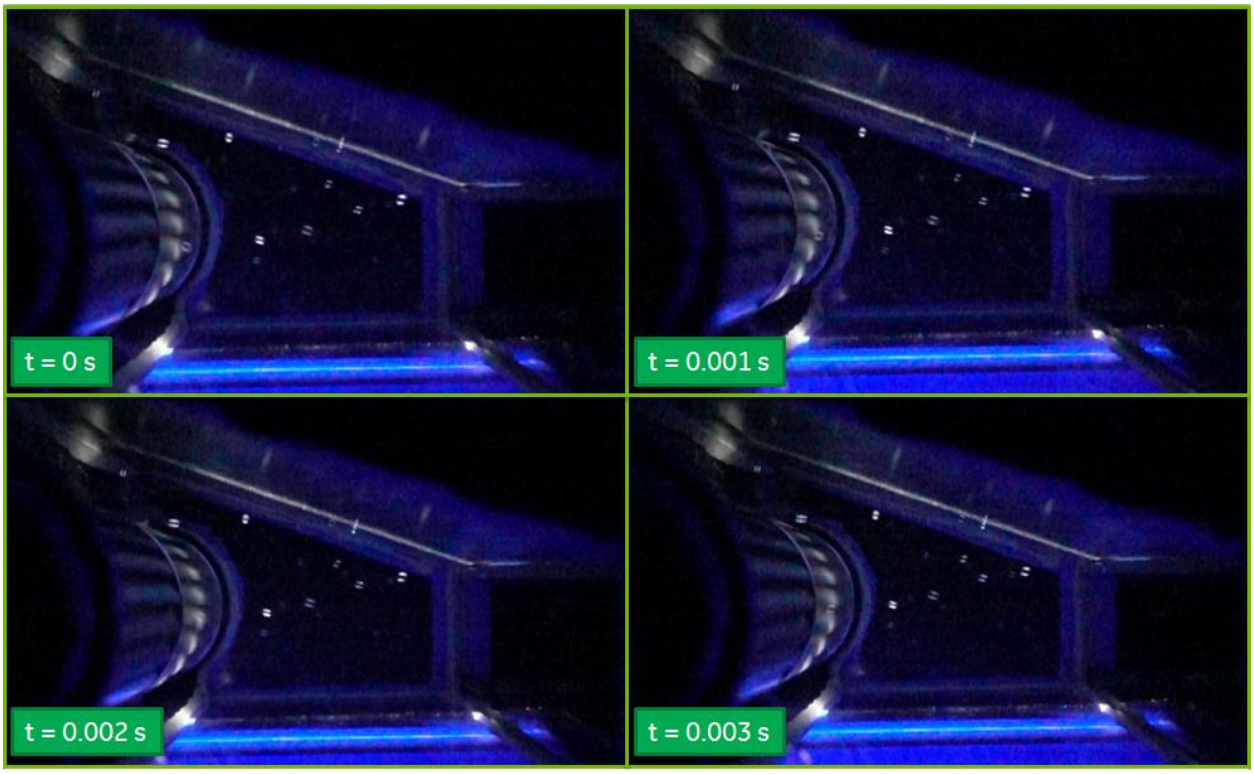

Figure 3-28 Four consecutive video frames (Sony RX100IV @960 fps)

The video quality that can be achieved with the Sony RX100 IV is sufficient to accurately visualize the bubbles at the velocities required for this research work. In order to measure the flow-field it is necessary to extract precise information from these videos. A post-processing technique was developed using Matlab.

3.3.4. Post-Processing: Matlab Program

A digital image is defined by a bitmap which is a matrix where the product of the number of rows and columns is equal to the number of pixels of the image. Each pixel has a numeric value that corresponds to a color or a combination of colors. Typically, the matrix is either 2D if the image is black and white (grayscale) or 3D if the image is in colors. Color images are defined by a combination of red, green and blue colors; therefore, they are 3D matrices where the information corresponding to each color is

stored in a different level of the matrix. A digital video is a series of images (frames) that were taken at constant rate; therefore, with the proper software, it can be divided into frames.

These frames have to be processed in order to extract the information needed for PTV measurements. Since processing 2D matrices is much easier than processing 3D matrices, usually the first step is to convert the color image into a grayscale. The information of grayscale images is stored in 8 bits which results in 256 states going from 0 to 255. A basic method used to process the resultant grayscale images is the threshold. The simplest version of the threshold replaces the pixel values that are lower than a set value to zero and sets all other pixel values to one. This creates a binary matrix where the regions of ones, also known as blobs, correspond to the objects of interest. The centroid, the area and other similar information can be obtained by using mathematical models to analyze these regions.

Matlab has many of these mathematical models built-in, many of them more complex than the simple threshold method. As discussed in Section 2.4.2, the Computer Vision toolbox has a Kalman filter regression algorithm that tracks objects by predicting their future location based on their current and previous locations. This program uses a dynamic background created by processing and adding from three to five previous frames, and it subtracts the current frame from this dynamic background to obtain the binary image. The PTV program was developed using the Matlab Image Processing package and the Computer Vision toolbox.

Computer Vision: Multiple Object Tracking

The center piece of the program used to calculate velocity fields in this study is a modification of one of the examples from Matlab Computer Vision toolbox that is named Motion-Based Multiple Object Tracking (MBMOT). The MBMOT program analyzes a video file and identifies all moving objects in it (Mathworks, 2015). Appendix A shows the program logic diagram with the Matlab MBMOT program shown in red. Since this example program is designed to track people moving, some changes had to be made in order to track helium filled bubbles. Some of the most important changes and additions are explained in this section.

First, a user interface (UI) was added to allow the user to select any video from the computer and prompts the user to provide the required information such as the video frame rate and the reference dimension (see Figure 3-29). The reference dimension is a known distance supplied by the user and based on two points that are easily identifiable in the first video frame. The frame rate and reference dimensions are used to convert the velocity from pixels per frame to inches per second.

Second, changes were made to the objects detection parameters. The minimum area was changed from a specific value to a variable. Also, the maximum area was added as a parameter. Adding the maximum and minimum area as thresholds to the detection algorithm ensures that all the detections correspond to bubbles or objects similar to bubbles and limits detections of light reflections or the movement of the impeller. The diameter of the helium bubbles ranges from 0.03” to 0.18”. However, the minimum and maximum area are calculated using a minimum diameter of 0.02” and a maximum diameter of 0.2” respectively to account for errors due to reference dimensions, proper

illumination, etc. The resultant area in pixels is the value of each variable used for object detection. Both of these variables depend on the reference distance, so the distance from the camera to the helium bubbles does not affect the detection range.

Third, the morphological operations were changed to improve object detection by reducing noise. The MBMOT program adjusted the detections into rectangular blobs, and this was changed into circular blobs of smaller size to better match the bubble edges. Also, the example used the Kalman filter algorithm to track the object even after it is no longer visible. This portion was removed because measurements can only be made by analyzing the actual trajectory of the helium bubbles. These changes improved the detection of helium bubbles and established the base for the velocity measurements.

Velocity Estimation

The program calculates the location of the blob centroid, and this location is written into a matrix that contains all the trajectories of all objects detected. Each column of the matrix corresponds to a bubble while each row is the location at each frame. After two or more rows are populated, the displacement, velocity, and angular direction are calculated. These values are saved in similar matrices. The loop is repeated for every frame of the video.

Once the entire video has been processed, the objects detected for less than eight consecutive frames are removed from the matrix. This clean-up process was added to ensure that the noise picked up for just a couple of consecutive frames does not affect the measurement. This is very common when bubbles are traveling just at the edge of the plane or when 3D vortices are present. The resultant data is averaged using all the data points, detected in a period of 2 seconds, inside each region and stored in new matrices.

These regions are small boxes of equal area and the centroids are defined by the user (see Figure 3-29). The purpose of these small regions is to average the vectors over the region, and the resultant vectors are used to make a map of the flow-field. The resultant matrices can be used to map the flow-field.

The user interface of the program developed is shown in the lower portion of Figure 3-29. As shown, the first frame of the video is loaded for the user to pick the reference points. After selecting the points, the user has to input the frame rate of the video and the distance between the reference points. The centroids of the regions are defined by the number in the vector grid box. A vector grid equal to 50 produces 2500 regions of equal area.

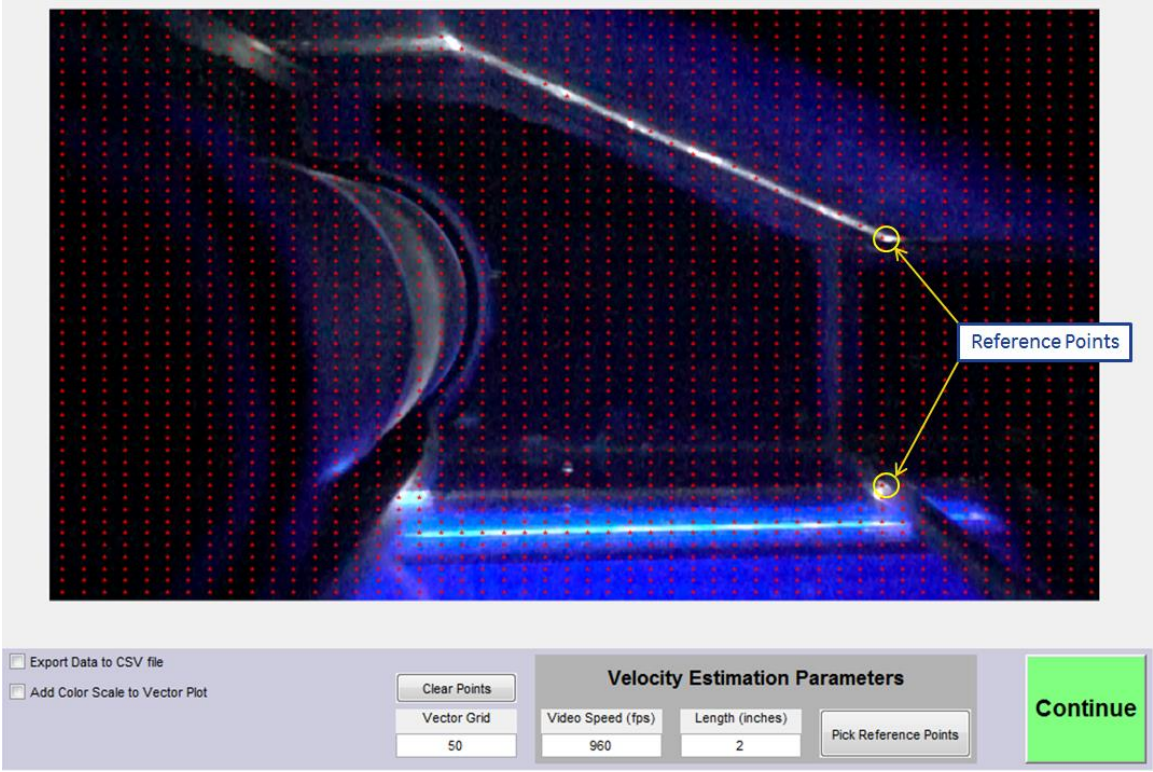

Figure 3-29 User interface

This method has an uncertainty in the vector scale due to the process of selecting the points. While this uncertainty can be significant for velocity estimation, the error introduced is the same for all vectors measured. As a result, the uncertainty of the streamlines plots is not as significant as the uncertainty of the vector plots.

Velocity Vector and Streamlines Plots

From the measured data, two plots were created to map the flow field: velocity vector and streamline. The velocity vector plot shows a vector with the average local velocity and the average velocity direction detected in each region. A color scale was added to this plot indicating the maximum velocity in red to the minimum velocity in blue. The streamline plot is very useful to visualize airflow patterns like vortices or recirculation. Figure 3-30 shows an example of both a velocity vector plot and a streamline plot.

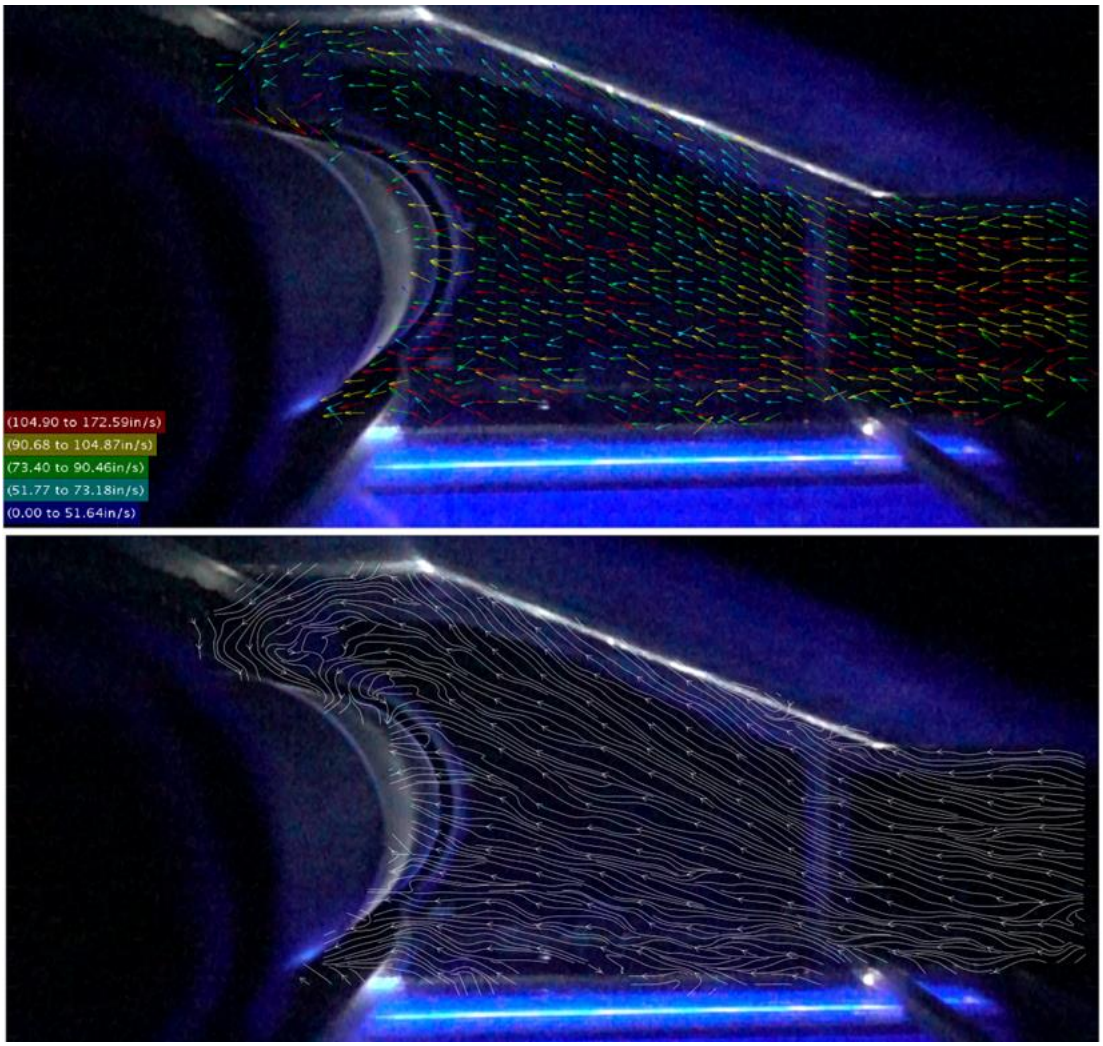

Figure 3-30 Velocity vector plot and streamlines plot for IG 0 at 55 CFM

3.3.5. PTV System Calibration Test

Two tests were completed in order to demonstrate the validity of the PTV system designed. The first test assessed the suitability of the helium bubbles as tracers for this specific application. Section 2.4.1 discussed the neutrally buoyancy of the helium bubbles and their quality as tracers. The Stokes number (Equation 13) based on the hydraulic diameter was used to estimate whether a round particle traveling with the airflow behaves as a tracer or not.

$$St = \frac{2}{9} * \frac{\rho_p}{\rho_f} * \left(\frac{a}{L}\right)^2 * Re_{duct} \quad (13)$$

The condition is that if $St < 1$ the particles follow the flow-field closely. This first test consists of changing the helium micro-metering valve while leaving the air and BFS unchanged. The micro-metering valve that controls the supply of BFS and air was set at 0.04". The helium valve was set at 0.003" which is the lowest set point possible where bubbles are generated. The test fixture was prepared with Inlet Geometry 0 (Table 3-1) with no restriction added to the system, and the LED light sheet was turned on. Two high speed videos were recorded for each helium valve set point going from 0.003" to 0.012" with increments of 0.001".

The videos were processed with the PTV program. The areas of all the bubbles detected were used to calculate the radius of each bubble (a). The duct Reynolds Number (Re_{duct}) was calculated using the equation $Re_{duct} = \rho V D_h/\mu$. In a duct the characteristic length (L) is the hydraulic diameter D_h. The density ratio (ρ_p/ρ_f) in St (Equation 13) was assumed to be 0.8, which is consistent with findings discussed by Kerho and Bragg (1994). Using this assumption, Equation 13 was used to calculate the maximum bubble radius at the volumetric flow rates of interest for a Stokes number of 1. The probability that the radius of each helium bubble is smaller than the maximum bubble radius for $S_t < 1$ was calculated for each case. Figure 3-31 shows the probability calculated for each configuration. At 25 CFM the probability that the helium bubbles are following the flow is close to 100%. At 40 CFM the probability drops to around 90% and at 55 CFM is closer to 80%. Similarly, the average Stoke numbers for each flow condition were estimated as $St_{55CFM} = 0.576,\ St_{40CFM} = 0.419,$ and $St_{25CFM} = 0.262$.

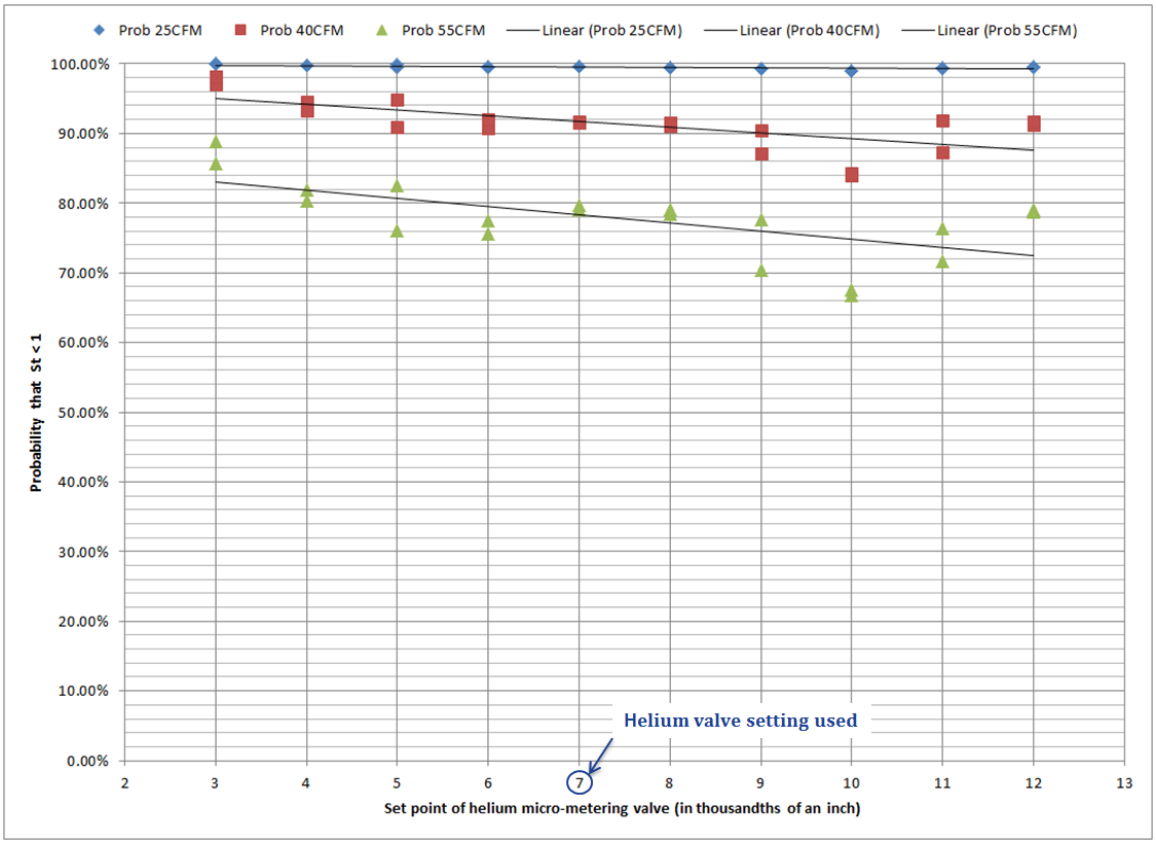

Figure 3-31 Probability that St < 1 for different helium valve set points

Although setting the helium valve to 0.003” produces bubbles that follow the flow-field closely, it does not produce the bubble density required for a good PTV measurement. Less than one hundred bubbles were detected with this helium valve setting versus more than six hundred with the valve at 0.007”. As a result, the helium valve was set at 0.007” for all other PTV measurements. Similarly, the BFS and the air were set at 0.04”. This valve setting reduces slightly the probability that the helium bubbles follow the flow from 80% to 78%, but increases considerably the number of bubbles produced by the generator. In conclusion, this test not only demonstrated that the helium bubbles will follow the flow in this application, but also helped determine the calibration used for testing.

The second test assessed the effect that mesh size used to analyze the flow-field has on the results. This was a qualitative test where a single video was measured multiple times with the PTV program. The mesh size was the only parameter changed between runs. The velocity vector plot and the streamlines plot were analyzed to determine which mesh produces the best results. This analysis showed that a 50 by 50 mesh produces a high quality velocity field. As shown in Figure 3-30, a 50 by 50 mesh produced between 45 and 72 vectors per square inch, which was enough detail to characterize the volume studied.

4. RESULTS

4.1. Performance and Efficiency Curves

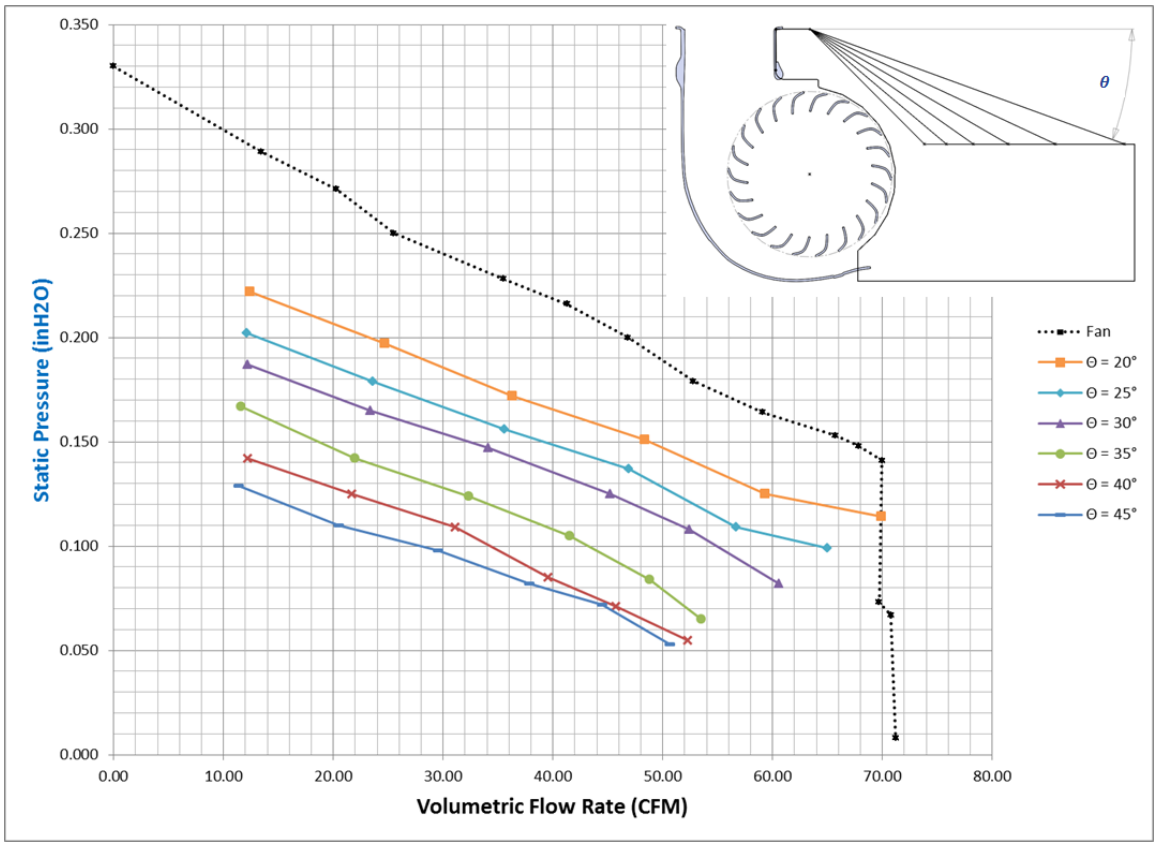

Figure 4-1 Static performance: θ = expansion angle

Figure 4-1 shows the static performance curves measured to study design variable θ (from Figure 3-3). As shown, the maximum volumetric flow rate increases at a rate close to 4.5 CFM for every 5° of angular increment, going from 52.2 CFM for θ = 40° to 70 CFM for θ = 20°. The first observation suggests that reducing the expansion angle increases the performance on the fan. However, reducing the angle also increases the

distance from the center of the impeller to the expansion point. The effect of both parameters has to be analyzed independently before reaching any conclusions. In order to understand the effect of the expansion angle θ, it is necessary to compare two or more inlet geometries that share the expansion point location, but have different expansion angle.

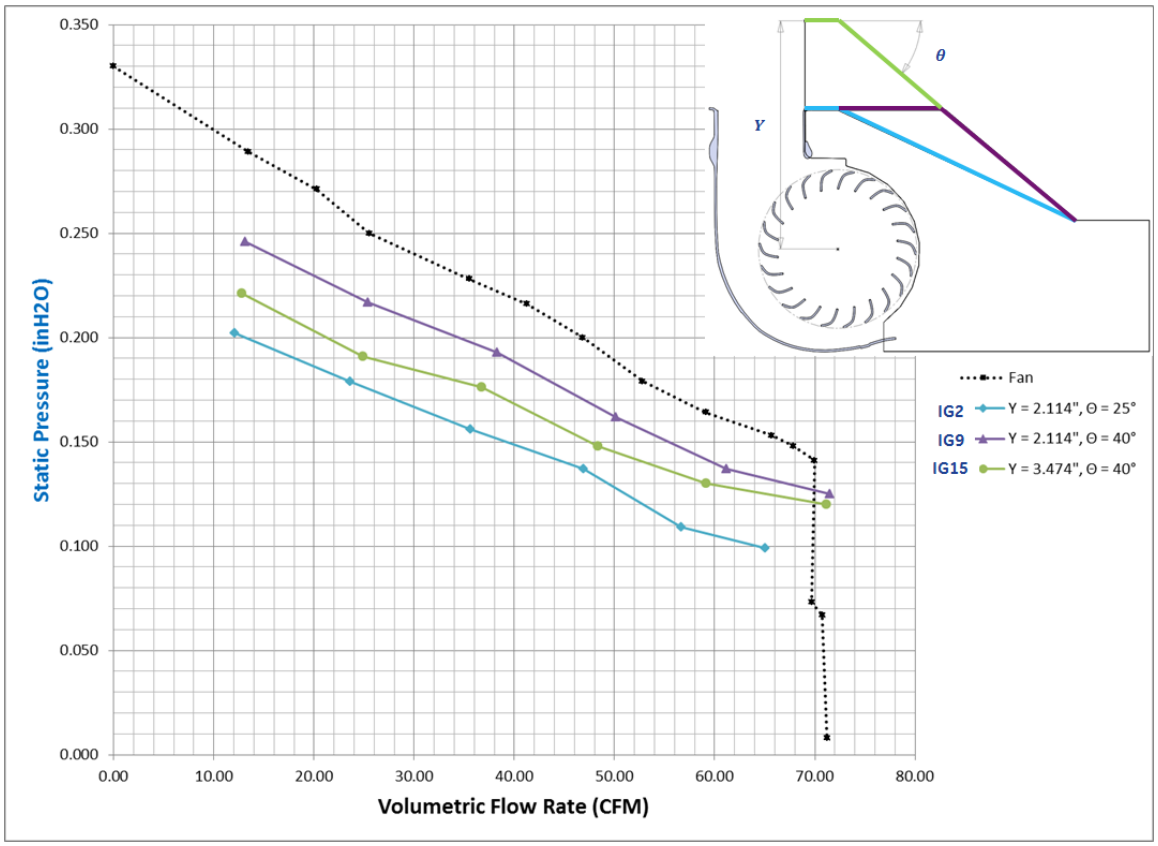

Figure 4-2 Static performance for inlet geometries 2, 9, and 15

The performance curves measured for three inlet geometries with nearly the same expansion point location are shown in Figure 4-2. Each one of these inlet geometries corresponds to one of the design variables studied. The difference between the performance curves of inlet geometry 2 (Y = 2.114", θ = 25°) and inlet geometry 9 (Y = 2.114", θ = 40°) indicates that a small angle, θ, reduces the fan performance. This

conclusion was confirmed by comparing inlet geometry 1 (X = 4.605" and θ = 20°) to inlet geometry 9 (X = 3.648" and θ = 40°). The comparison is shown in Figure 4-3. The gap between the expansion points of these two geometries is $X_1 - X_9 = 0.957"$. However, the fan performance with inlet geometry 9, with an expansion point that is closer to the impeller, is better. This indicates that the fan performance improvements shown in Figure 4-1 are due to the increase in the distance to the expansion point (X) and not due to the expansion angle (θ).

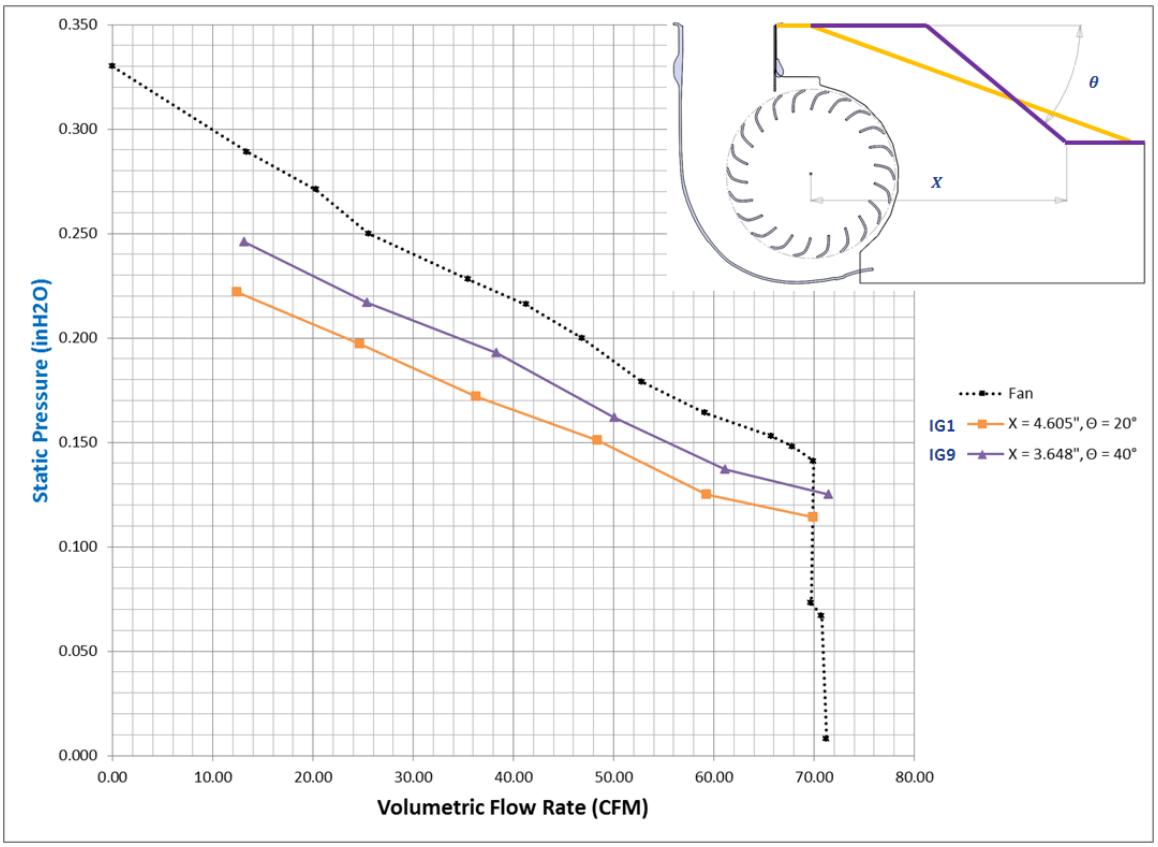

Figure 4-3 Static performance for inlet geometries 1 and 9

As discussed in Section 3.1.2, design variable X (from Figure 3-3) aimed to understand the effect of moving the expansion point away from the fan. The graph shown in Figure 4-4 contains the static performance curves measured for the different inlet

geometries used to study this design variable. The graph shows that increasing the distance from the center of the impeller to the expansion point increases the performance of the fan. Also, that the performance at 3.648”, 4.198”, and 4.748” are similar and close to the static performance curve of the fan without inlet geometry. This indicates that an optimal distance exists in the range from 3.098” to 4.198”.

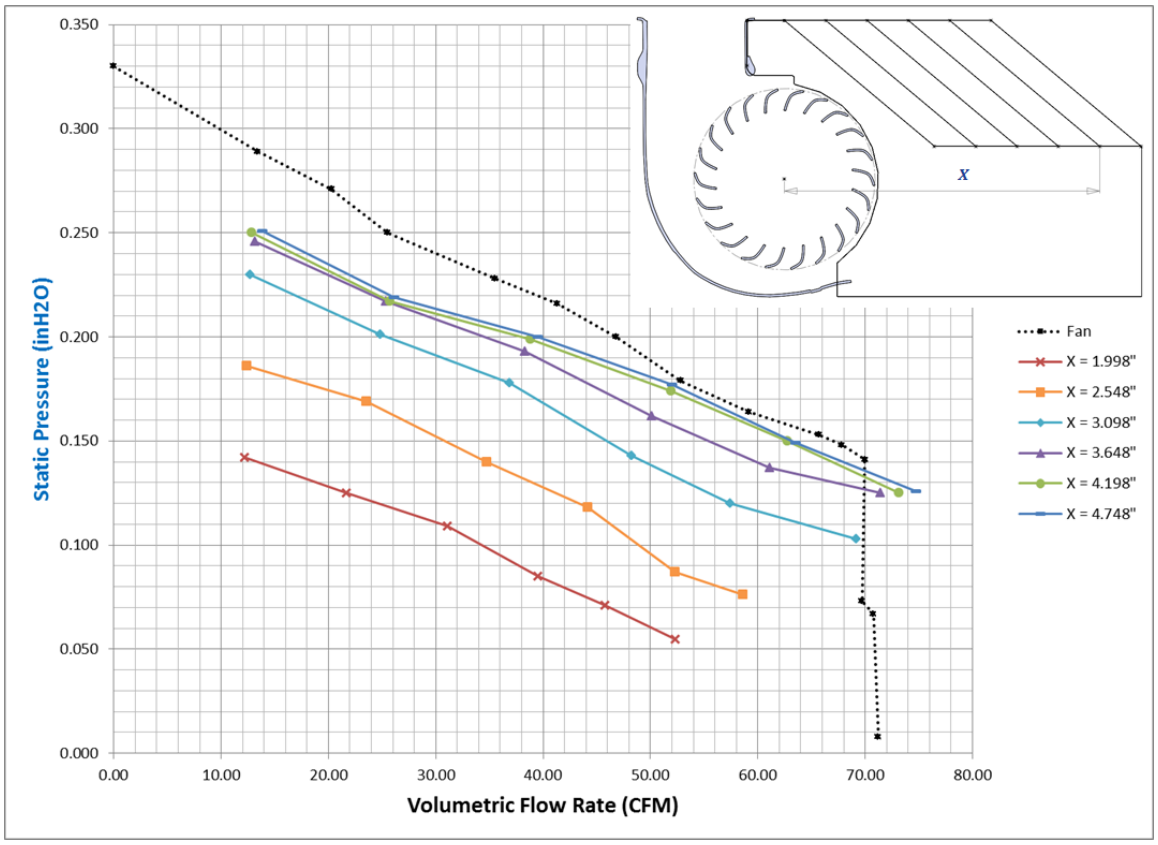

Figure 4-4 Static performance: X = distance to expansion point

Also shown in Figure 4-4, the maximum stable performance point measured increases from 0.055 inH_2O at 52.2 CFM for X = 1.998” to around 0.103 inH_2O at 70 CFM for X = 3.098”. This is a significant increase in fan performance for a 1.1” change.

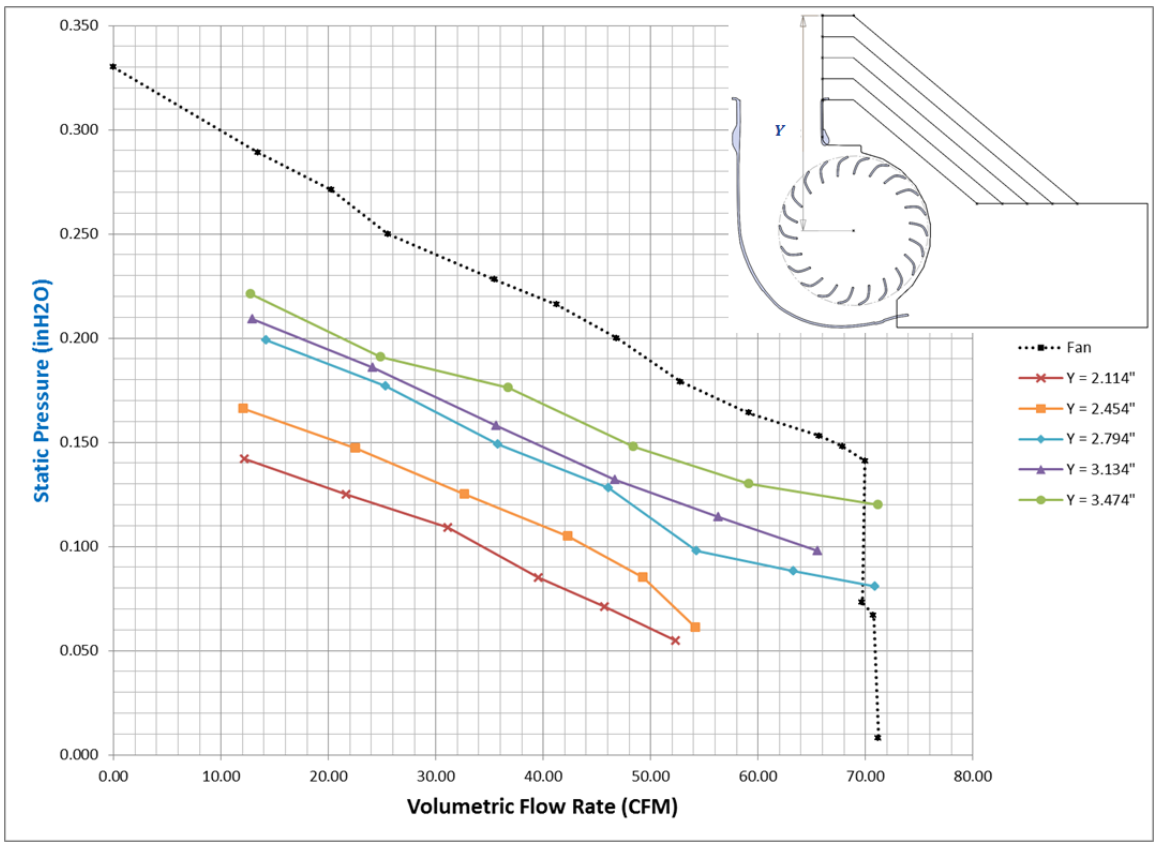

Figure 4-5 Static performance: Y = distance to top wall

The static performance curves measured to study design variable Y are shown in Figure 4-5. In this case, similar to θ, moving the top wall away from the impeller changes the distance to the expansion point; therefore, the following comparison was required to determine the positive or negative effect of increasing the distance from the impeller to the top wall. Inlet geometries 9 and 15 have the same expansion angle (40°), nearly the same distance to the expansion point (3.648" and 3.619" respectively), but different value for Y (2.114" and 3.474" respectively). The static performance curve measured for both of these inlet geometries is shown in Figure 4-6. As shown in the figure, inlet geometry 9 (X = 3.648", Y = 2.114") performs better than inlet geometry 15 (X = 3.619", Y = 3.474"). This indicates that increasing the distance from the impeller to the top wall (Y)

reduces the performance of the fan. As a result, for the set of inlet geometries tested (shown in Figure 4-5), the fan performance improvements are due to the increase in the distance from the impeller to the expansion point (X).

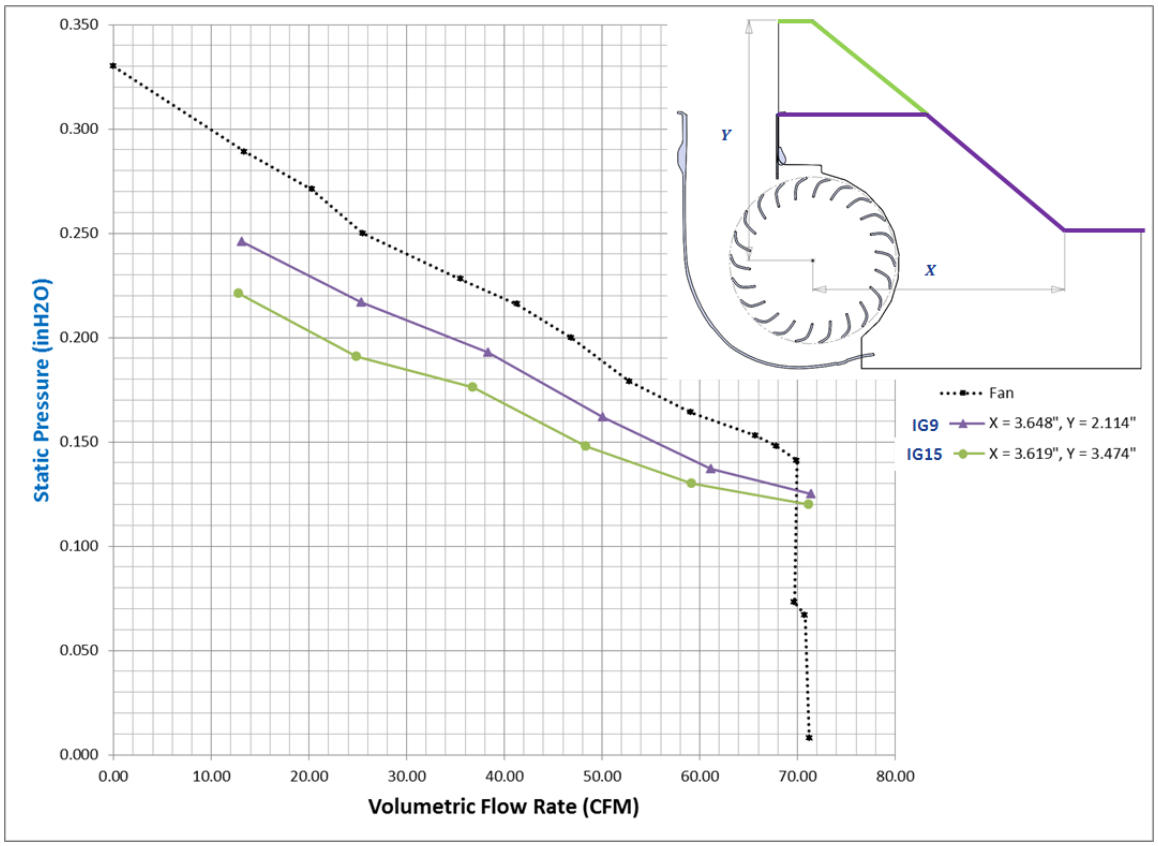

Figure 4-6 Static performance for inlet geometries 9 and 15

The static performance curves measured for six inlet geometries with different vortex wall angles (δ) are shown in Figure 4-7. This set of performance curves correspond to the design variable δ. As shown, this design variable has little effect on the fan performance. In addition, a slightly negative effect should be expected for an angle larger than 30 degrees. This negative effect can be seen by comparing $\delta = 0°$ to $\delta = 60°$ in Figure 4-7. In this figure, $\delta = 0°$ has a maximum flow of 69 CFM at 0.102 inH_2O, but

$\delta = 60°$ has a maximum flow of 64 CFM at 0.087 inH_2O. This design variable will not be discussed further in this study.

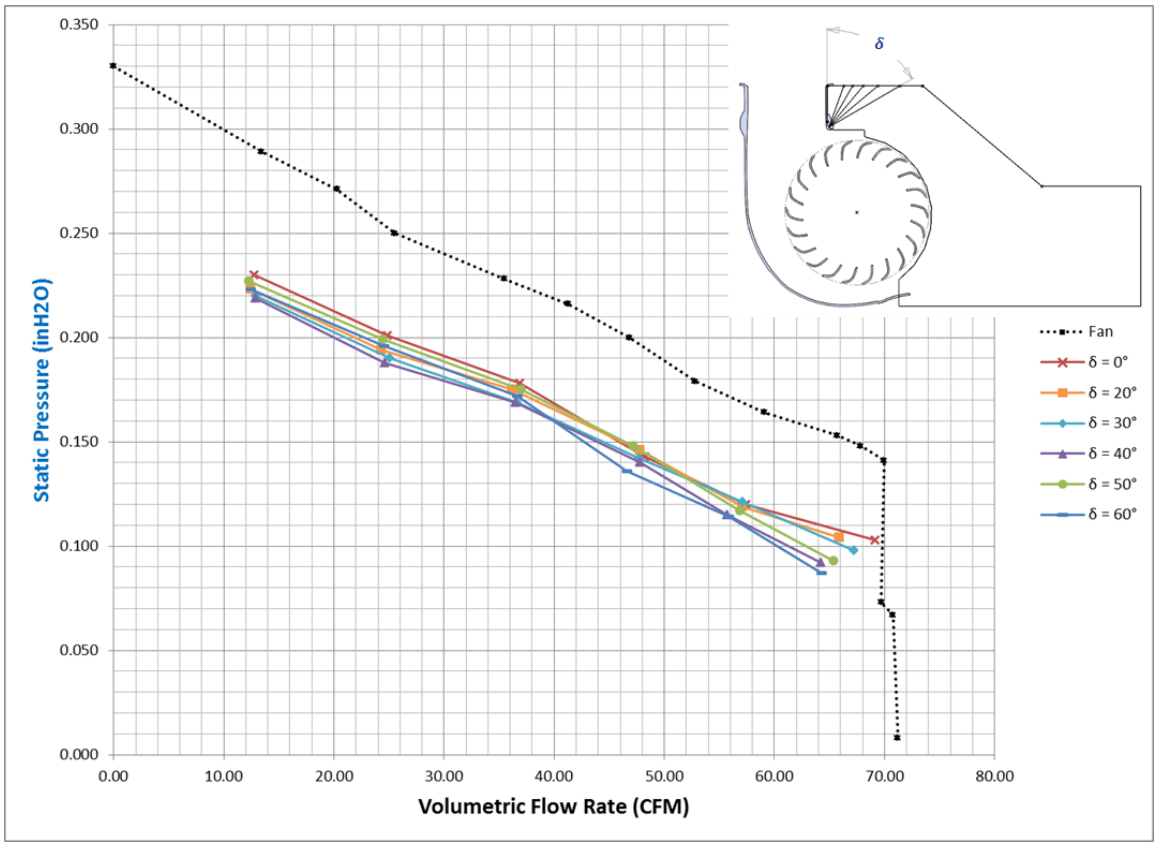

Figure 4-7 Static performance: δ = angle of guide vane near vortex wall

Appendix B contains all static efficiency curves measured during this study. In addition, dimensionless performance and efficiency curves were developed and can be found in Appendix C and D respectively.

4.2. Flow Visualization Results

A main objective in this study is to characterize the flow field inside the duct inlet to understand the effect of each design variable. The methodology explained in section 3.3 was followed to obtain velocity vector fields and streamlines plots for every geometry at two different volumetric flow rates. In order to facilitate the qualitative analysis of each design variable, the streamlines plot of three different inlet geometries are shown in the same figure.

Airflow visualization and flow-field measurements were completed at three constant flows rates (25 CFM, 40 CFM, and 55 CFM). The streamline plot measured at 25 CFM for inlet geometries 1, 3, and 5 are shown in Figure 4-8. In order to reach equilibrium between the airflow chamber fan and the cross-flow fan at 25 CFM, the airflow entering the contraction cone has to be restricted significantly. This reduction in the orifices area of the airflow restriction prevents many of the helium bubbles for entering the duct. As a result, the flow-field cannot be fully mapped because of the limited number of bubbles that can be tracked at this volumetric flow rate (see Figure 4-8). This means that at the flow visualization methodology developed in this study is not effective at 25 CFM; therefore, it will not be used for the discussion.

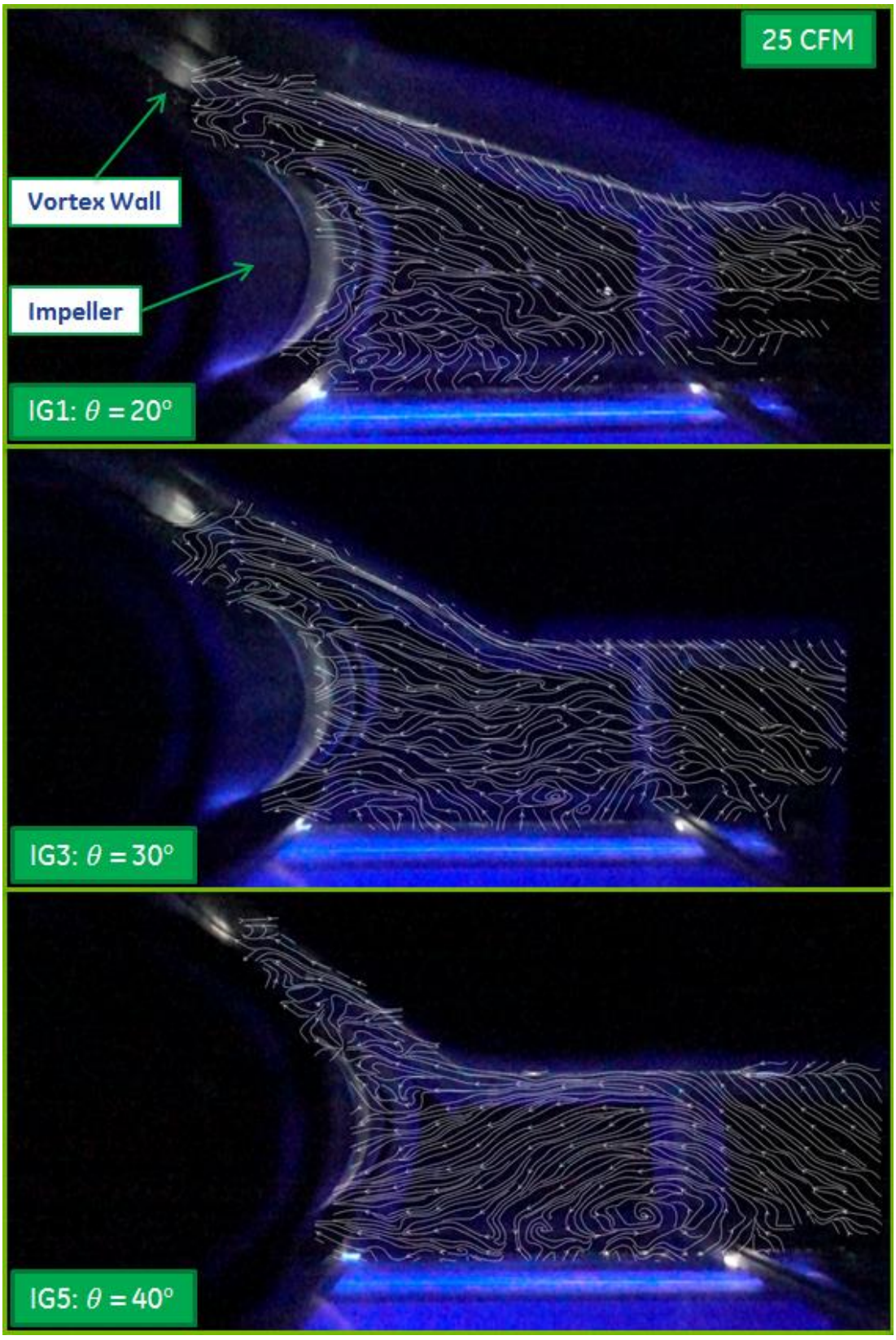

Figure 4-8 Streamlines: θ = expansion angle at 25 CFM

The streamlines plot obtained for expansion angles 20°, 30°, and 40° at 40 CFM are shown in Figure 4-9. These streamlines plots show that the flow near the expansion wall is different for each expansion angle. For example, the flow near the expansion wall for an expansion angle of 30° seems to be much more stable than for an angle of 20°. Another interesting characteristic is the vortex that appears on the bottom wall for an angle of 40°. This vortex is not present in the other two cases, but flow separation is present in the same location for the 30° geometry. Another vortex was found in front of the vortex wall and right above the impeller for the 20° and 30° cases. This vortex appears due to the location of the eccentric vortex (not visible in the streamlines plots) and the vortex wall distance (α_2).

The streamlines plot at 55 CFM for the same inlet geometries is shown in Figure 4-10. The figure shows that increasing the volumetric flow rate reduces the flow separation found at 40 CFM for the 20° geometry. Also, with the flow rate increase, the vortices in front of the vortex wall strengthen. This vortex does not occur for $\theta = 40°$. Instead, strong reversed flow characterizes the region. On the other hand, the vortex found on the bottom wall of the 40° geometry at 40 CFM is considerably reduced to a region of flow separation. These streamline plots show that the suction region of the impeller changes depending on the inlet geometry. For example, the suction region for the 20° geometry is about the full height of the impeller with very little air entering on the upper portion of the impeller near the vortex wall. The suction region is smaller for the 30° geometry reaching only about half the height of the impeller and even smaller for the 40° geometry with basically zero flow going into the upper half of the impeller.

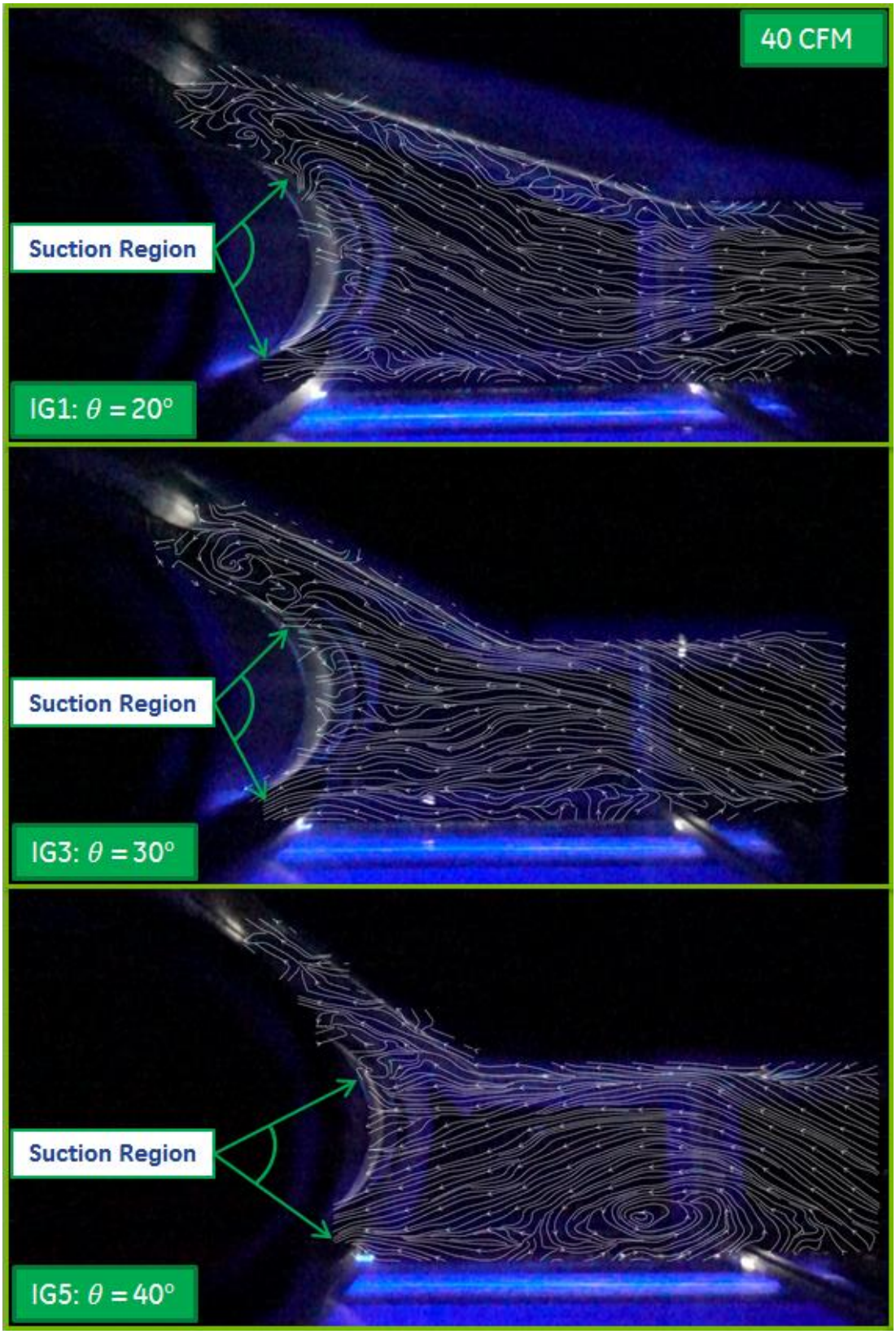

Figure 4-9 Streamlines: θ = expansion angle at 40 CFM

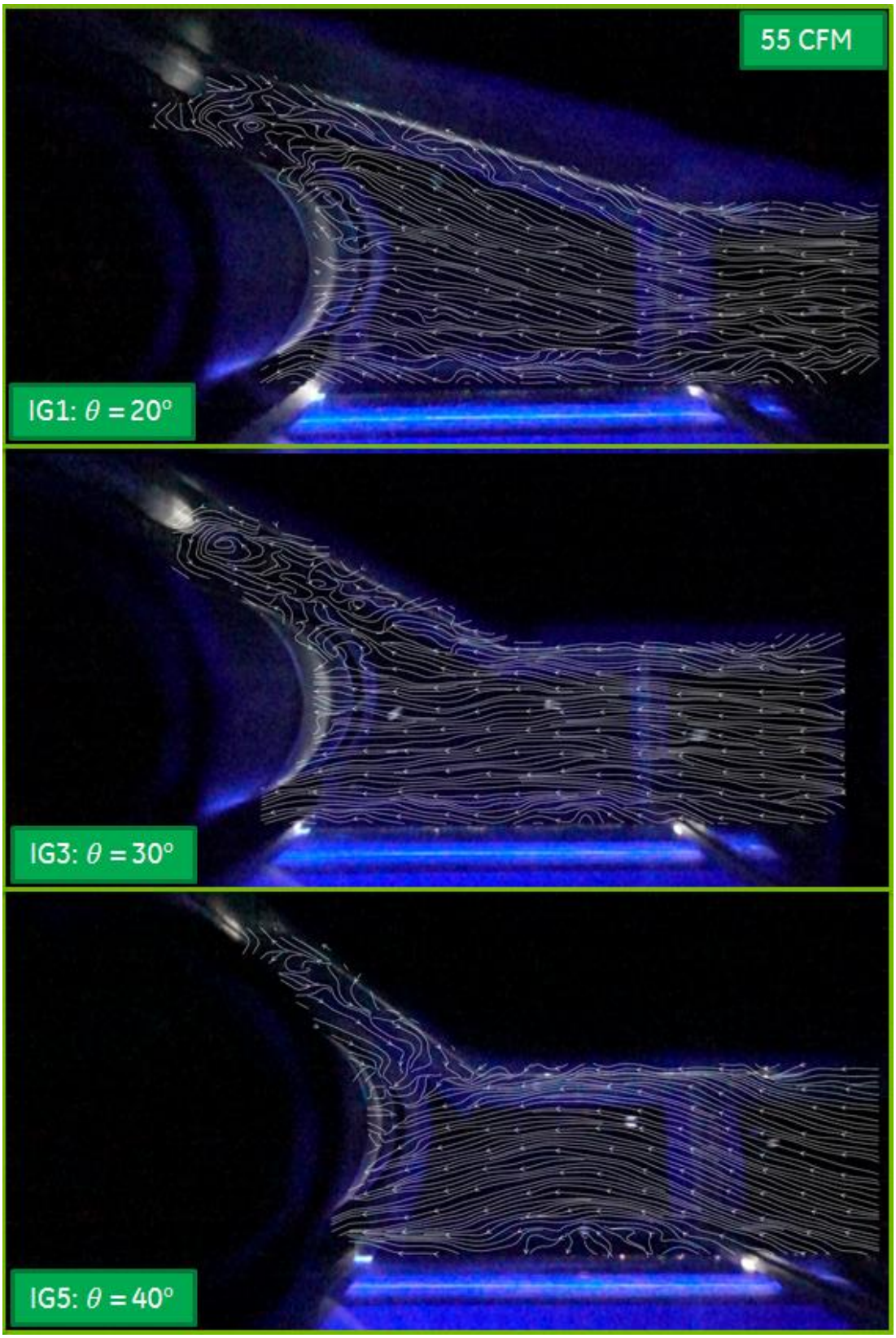

Figure 4-10 Streamlines: θ = expansion angle at 55 CFM

The streamlines plot for inlet geometries 5, 7, and 9 (for increasing X) at 40 CFM are shown in Figure 4-11. A comparison between these streamline plots shows that two vortices appear as the expansion point gets closer to the impeller. The first vortex is located on the bottom wall. This vortex is not present in geometry 9, but it grows and strengthens as the expansion point gets closer to the impeller (as X decreases). The second vortex is located above the impeller near the vortex wall. In this case, geometry 9 shows the flow changing direction in this area, but it is not fully formed. This is different in geometry 7 where the vortex is perfectly formed above the impeller. However, the streamlines plot for inlet geometry 5 show that this vortex disappears as the expansion point gets too close to the impeller.

The streamline plots for the same three inlet geometries at 55 CFM are shown in Figure 4-12. These plots show that at 55 CFM the vortex on the bottom wall reduces considerably. Also, the flow in the region above the expansion point becomes much more turbulent with multiple small vortices appearing. A comparison between Figure 4-11 and Figure 4-12 shows that the suction region in geometry 9 is about the same at 40 CFM and at 55 CFM. However, in geometry 7 and geometry 5 the effective suction region becomes smaller as the volumetric flow rate increases. This correlates to the drop in performance shown in Figure 4-4.

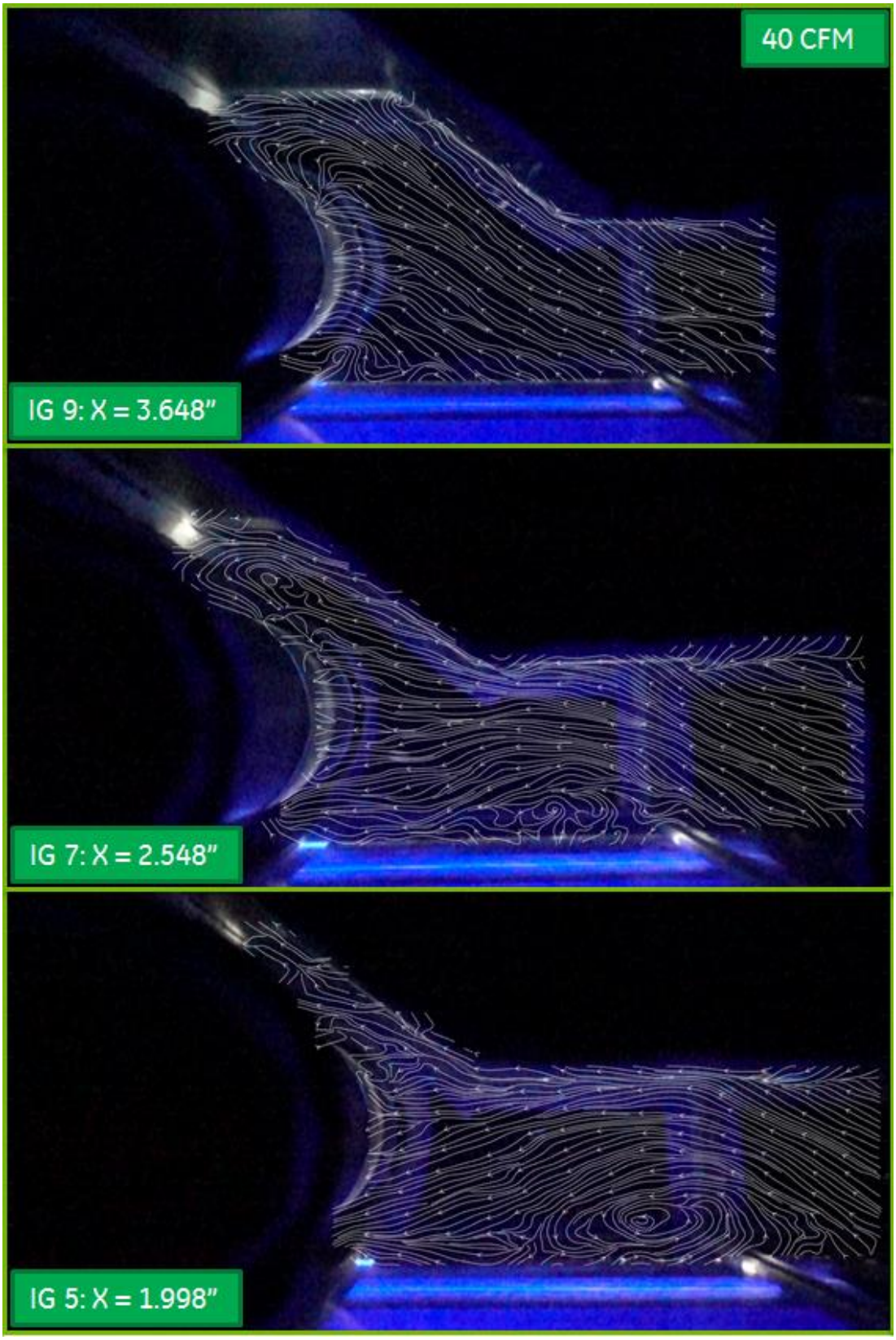

Figure 4-11 Streamlines: X = distance to expansion point at 40 CFM

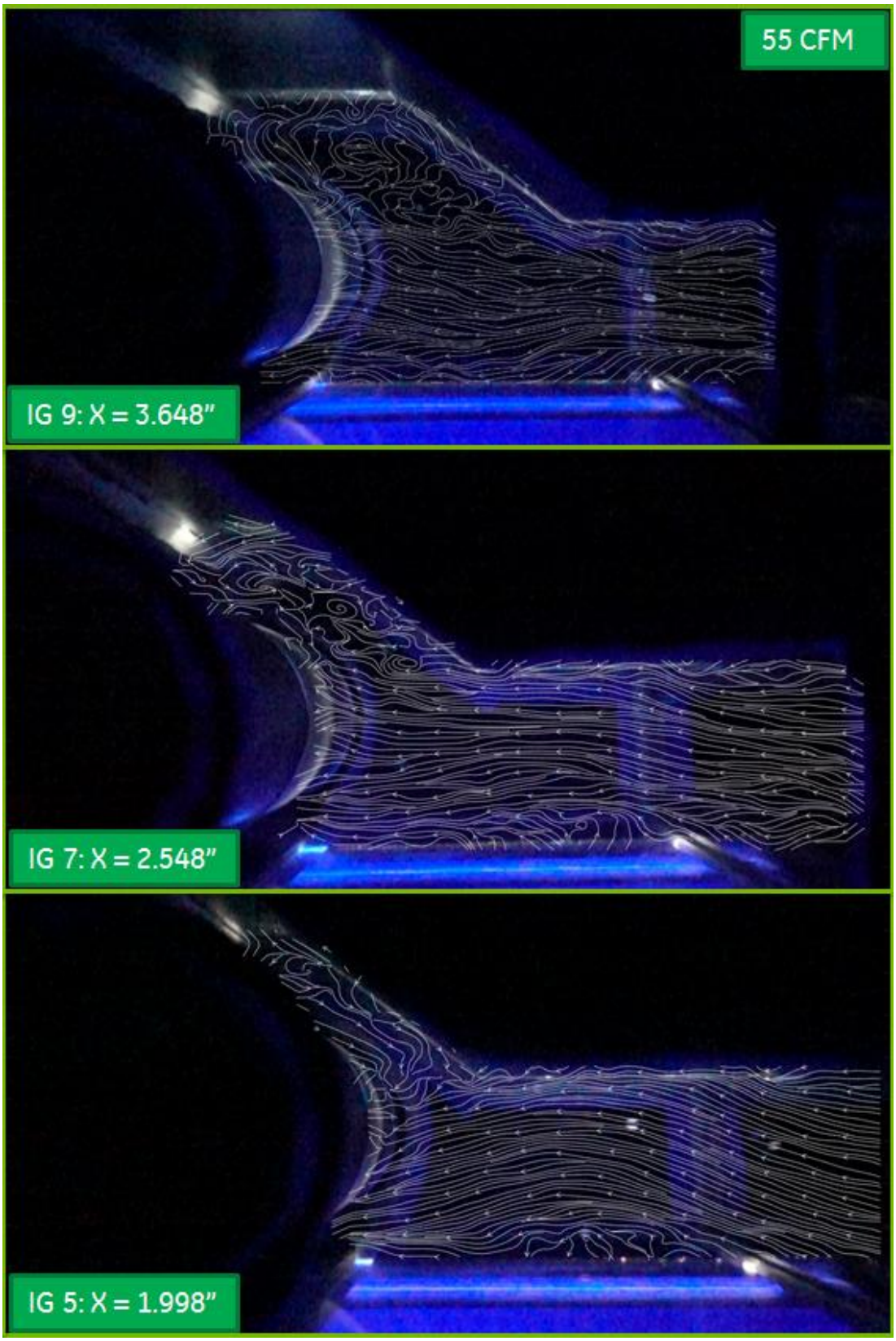

Figure 4-12 Streamlines: X = distance to expansion point at 55 CFM

Figure 4-13 and Figure 4-14 show the streamlines plot corresponding to three inlet geometries at 40 CFM and 55 CFM respectively. These three geometries have the same expansion angle, but their distance to the expansion point and their distance to the top wall are different. In this case, three characteristic vortices were found. Similar to the previous two cases discussed, as the expansion point gets closer to the impeller a vortex appears on the bottom wall of the inlet geometry. In addition, the previously discussed vortex right above the impeller and near the vortex wall is present. This vortex decreases as the expansion point gets closer to the vortex wall; therefore, it is not present in inlet geometry 5. The third vortex appears above the second vortex and slightly above the top portion of the vortex wall. This vortex grows and strengthens with an increase in either the distance from the center of the impeller to the top wall or the volumetric flow rate.

In Section 5.1, Figure 4-2 was used to analyze the effect of θ and Y. The streamlines plots for these same geometries at 40 CFM and 55 CFM are shown Figure 4-15 and Figure 4-16 respectively. Correlations were found between the differences in performance shown in Figure 4-2 and the streamlines plots shown in Figure 4-15 and Figure 4-16. For example, the streamlines in geometry 2 are unstable, and the effective suction region is smaller than those of geometries 9 and 15, which is consistent with the performance curves measured. On the other hand, the streamlines for geometries 15 and 9 are very similar. The main difference between the two is the vortex that appears above the impeller and right above vortex wall. This vortex indicates a negative pressure region that affects the flow entering the impeller. This can be observed at 55 CFM where the effective region is reduced considerably because the flow sliding above the impeller. As a

result, the performance of the fan with geometry 15 is lower than the performance of the fan with geometry 9, but higher than the performance measured with geometry 2.

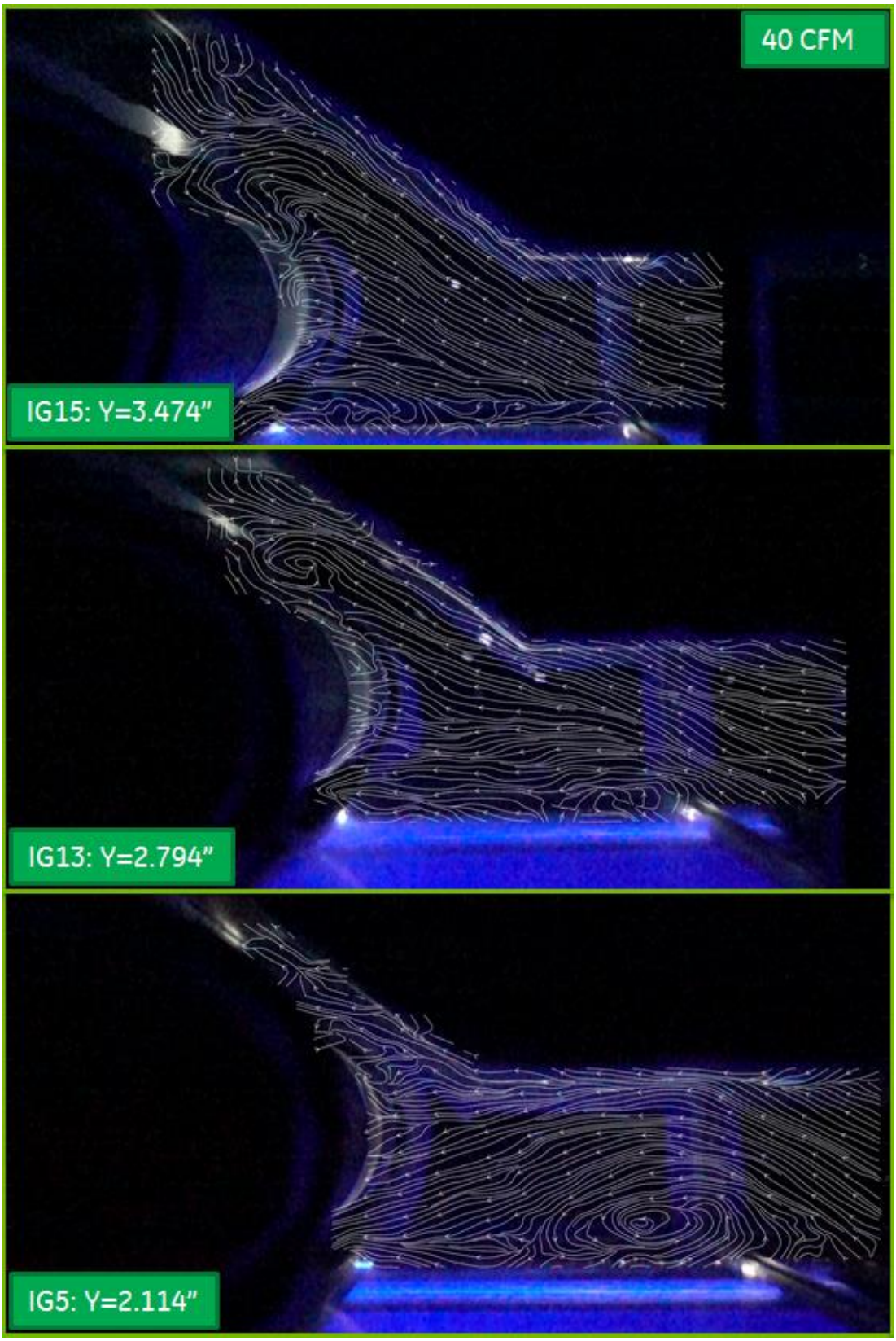

Figure 4-13 Streamlines: Y = distance to top wall at 40 CFM

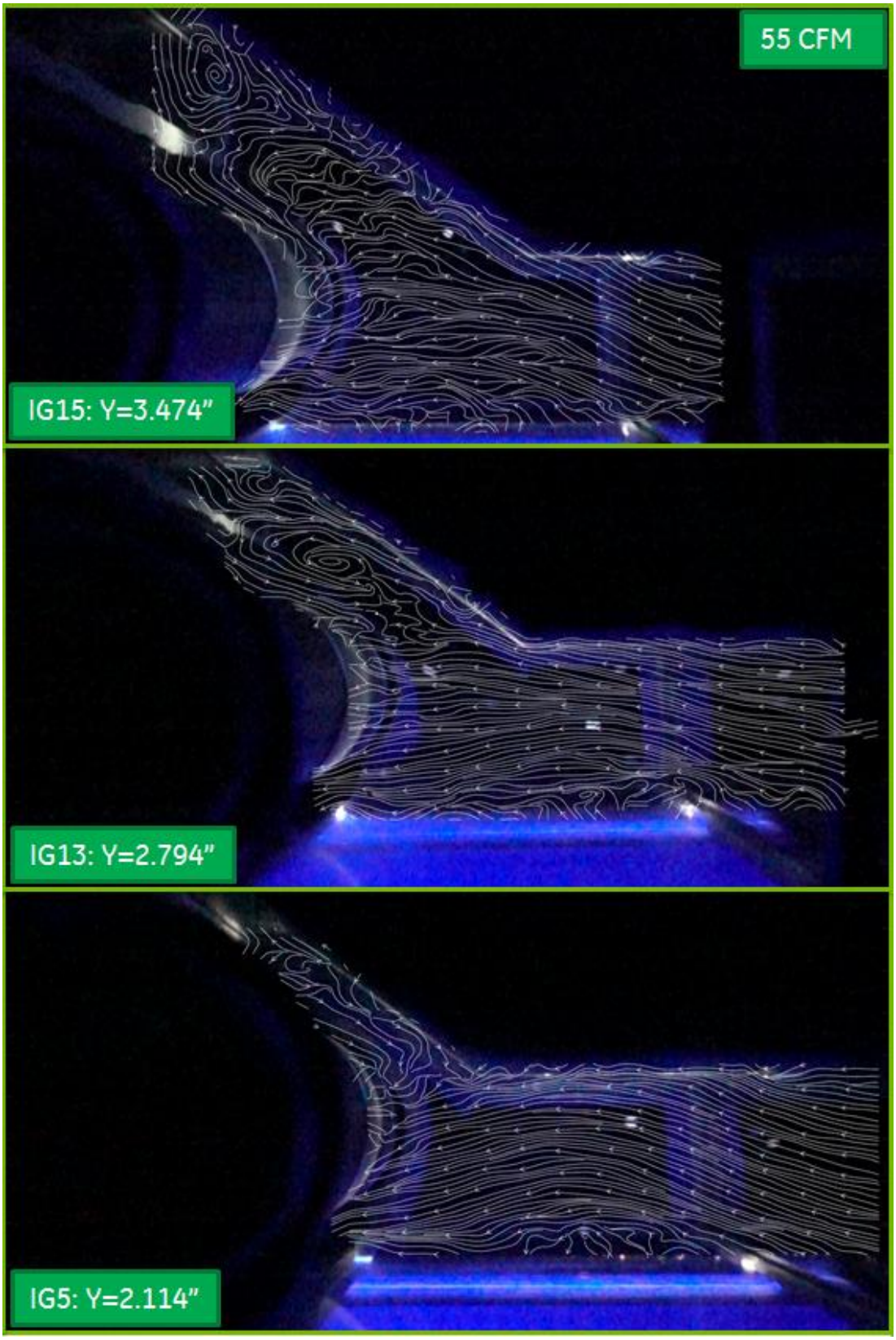

Figure 4-14 Streamlines: Y = distance to top wall at 55 CFM

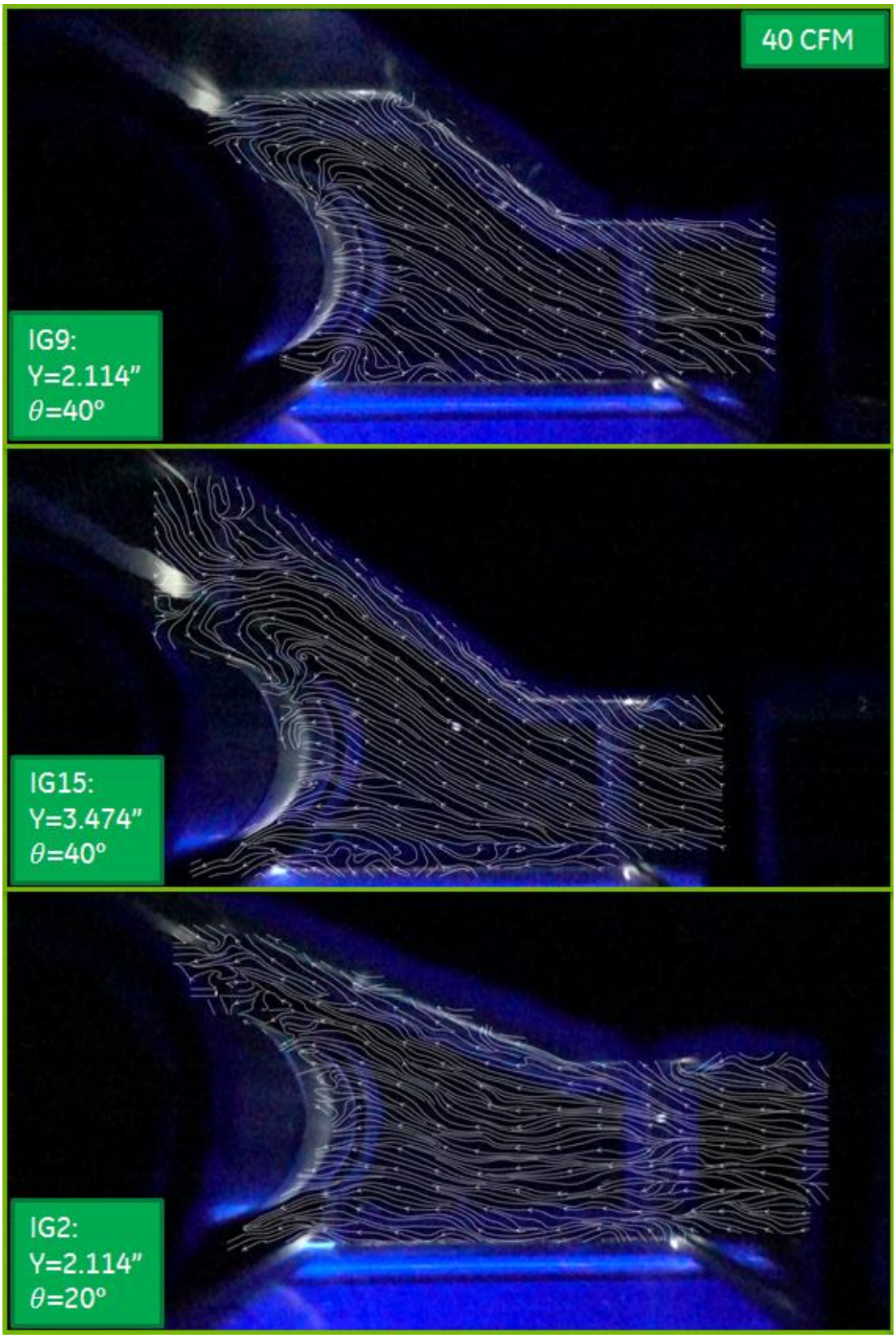

Figure 4-15 Streamlines: inlet geometries 2, 9, and 15 at 40 CFM

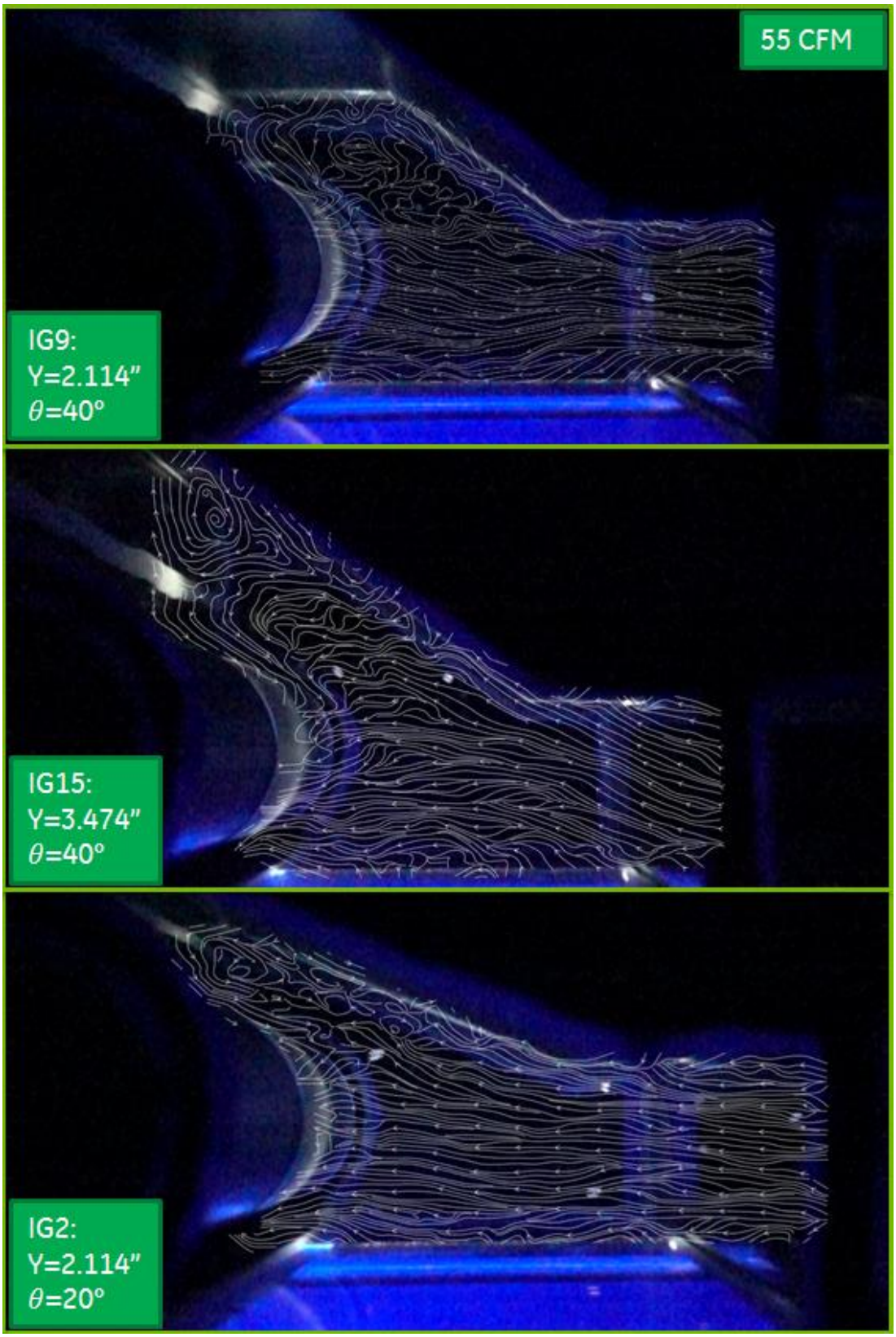

Figure 4-16 Streamlines: inlet geometries 2, 9, and 15 at 55 CFM

4.3. Discussion of the Results

The difference in static performance between inlet geometries 2, 9, and 15 was discussed in Sections 5.1 and 5.2. A direct comparison of their performance curves indicates that reducing the expansion angle or increasing the distance to the top wall reduces the performance of the fan. In addition, in Section 5.2 it was discussed that this drop in performance is related to either unstable flow in the case of geometry 2 or a vortex that appears right above the vortex wall and above the impeller. This comparison was relevant because it separated the effect of the distance from the impeller to the expansion point (X) from the effect of the expansion angle (θ) and the distance from the impeller to the top wall (Y).

Design variable X was different for all the inlet geometries studied. The relationship between this design variable (the distance to expansion point) and the fan performance at 40 CFM is shown in Figure 4-17. This graph shows that increasing Y or reducing θ decreases the performance of the fan; therefore, it confirms the findings discussed in Section 5.1 and Section 5.2.

The most significant flow field characteristics were discussed in Section 5.2. Although it varies in size and strength, the vortex above the impeller and near the vortex wall is present in all the inlet geometries studied. Also it was found that for all cases, reversed flow was found in the upper portion of the impeller near the vortex wall, especially with increased flow rate (see Figure 4-16). This is consistent with reversed flow between the vortex wall and the impeller from the discharge to the suction region. The interaction between this reversed flow and the flow in the suction region generates the vortex above the impeller.

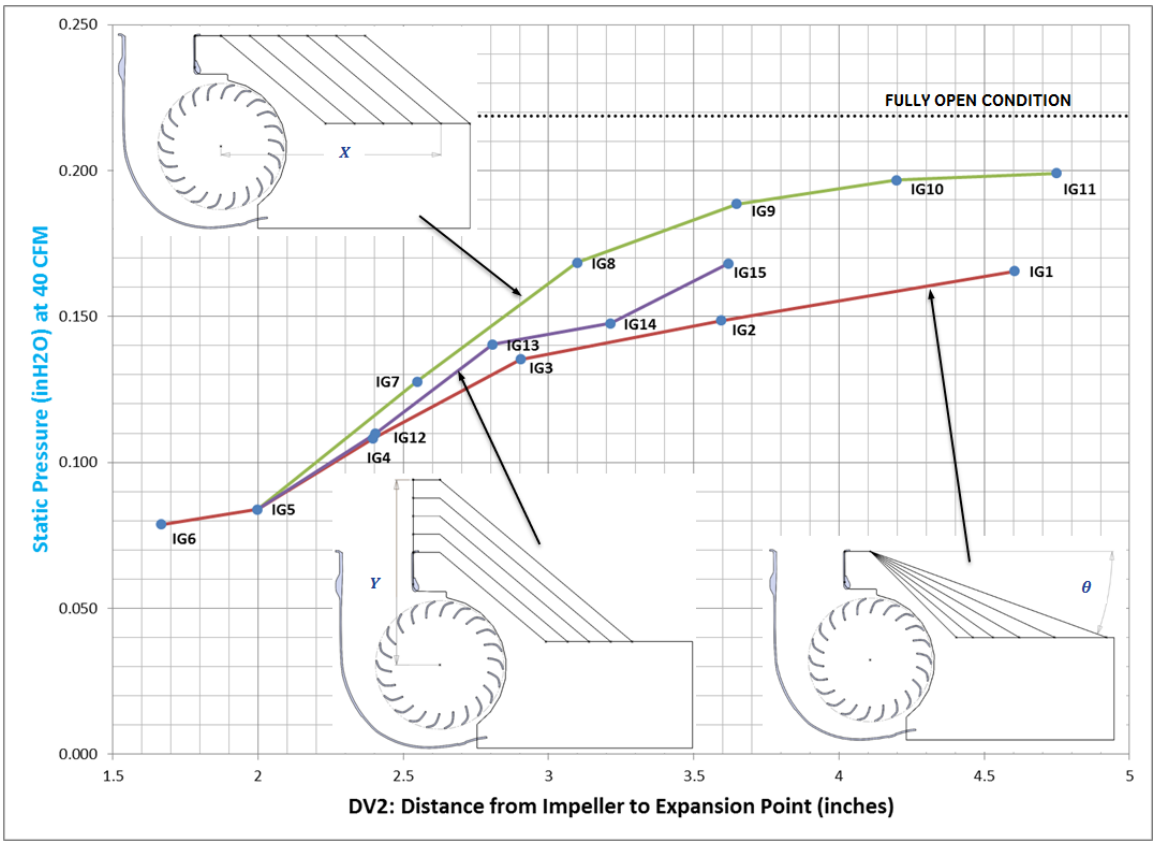

Figure 4-17 Relationship between X and static performance at 40 CFM

A factor that influences the appearance of this reversed flow is the ratio of vortex wall distance to impeller outer diameter (ε_2/D_2). As discussed in Chapter 4, ε_2 and D_2 were measured for this cross-flow fan using a 3D scanner, and the resultant value for ε_2/D_2 was 10.12%. This ratio is larger than the recommended limit of 7.5% discussed by Ikegami and Murata (1966); therefore, the vortex wall is not close enough to restrict the flow from going back from the discharge to the suction region. A representation of the flow is shown in Figure 4-18. In this figure, the expected flow based on the results of Tuckey (1983) and Eck (1973) is represented by dotted arrows (see Figure 2-3).

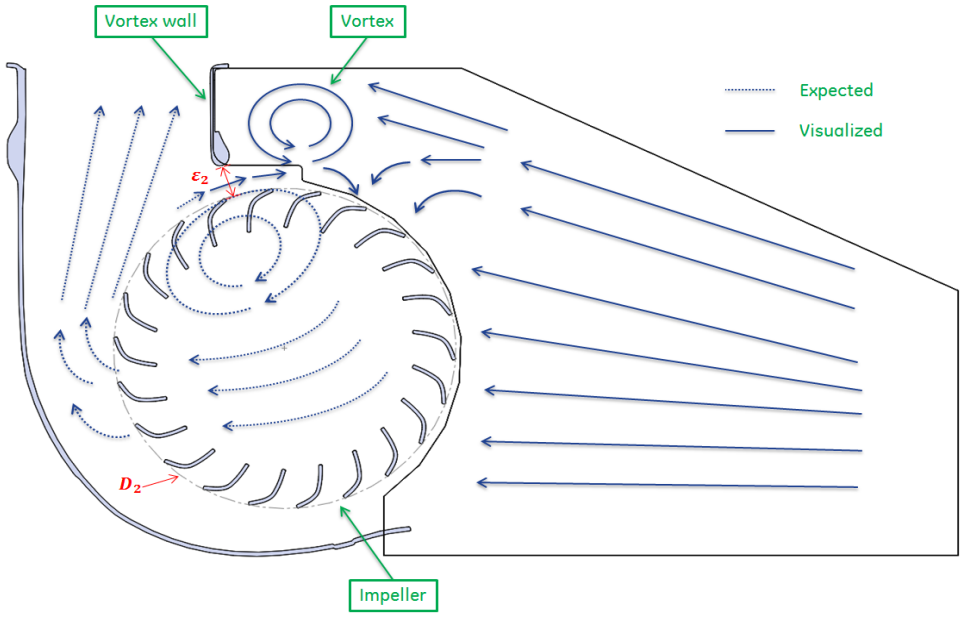

Figure 4-18 Representation of the flow field showing reversed flow

As discussed in Section 2.1, Ikegami and Murata (1966) also showed that reducing the ratio ε_2/D_2 increases the performance, but it also increases the noise and vibration of the fan. To investigate the impact of ε_2/D_2, a series of tests were completed where ε_2/D_2 was reduced by extending the vortex wall by increments of 0.04". Using inlet geometry 0 (Table 3-1), a total of six vortex wall lengths were tested. Table 4-1 shows the length added to the vortex wall (W), the resultant vortex wall position angle (α_2), and the resultant vortex wall distance to impeller outer diameter ratio (ε_2/D_2).

Figure 4-19 shows the performance curves measured. As shown, increasing the vortex wall length by 0.08" or more increases the performance of the fan. In other words, reducing the ratio of ε_2/D_2 to 7.66% or less improves the performance of the fan. It was also found that for small ε_2/D_2 ratios (ε_2/D_2 < 5%) the noise and vibration of the fan increases. These findings are consistent with the conclusions of Ikegami and Murata (1966). The graph in Figure 4-19 shows that as the vortex wall is elongated the fan

performance improves, but the maximum achievable volumetric flow rate deteriorates. This reduction of the volumetric flow rate is generated by the change in the vortex wall position angle (α_2). As α_2 increases the maximum volumetric flow rate decreases.

Table 4-1 Vortex wall length increment and resultant ratio (ε_2/D_2)

W (in)	α2	ε2 (in)	ε2/D2
0.000	18.18	0.244	10.12%
0.040	20.48	0.222	9.19%
0.080	21.06	0.185	7.66%
0.120	21.67	0.147	6.08%
0.160	22.32	0.110	4.55%
0.200	23.01	0.073	3.02%

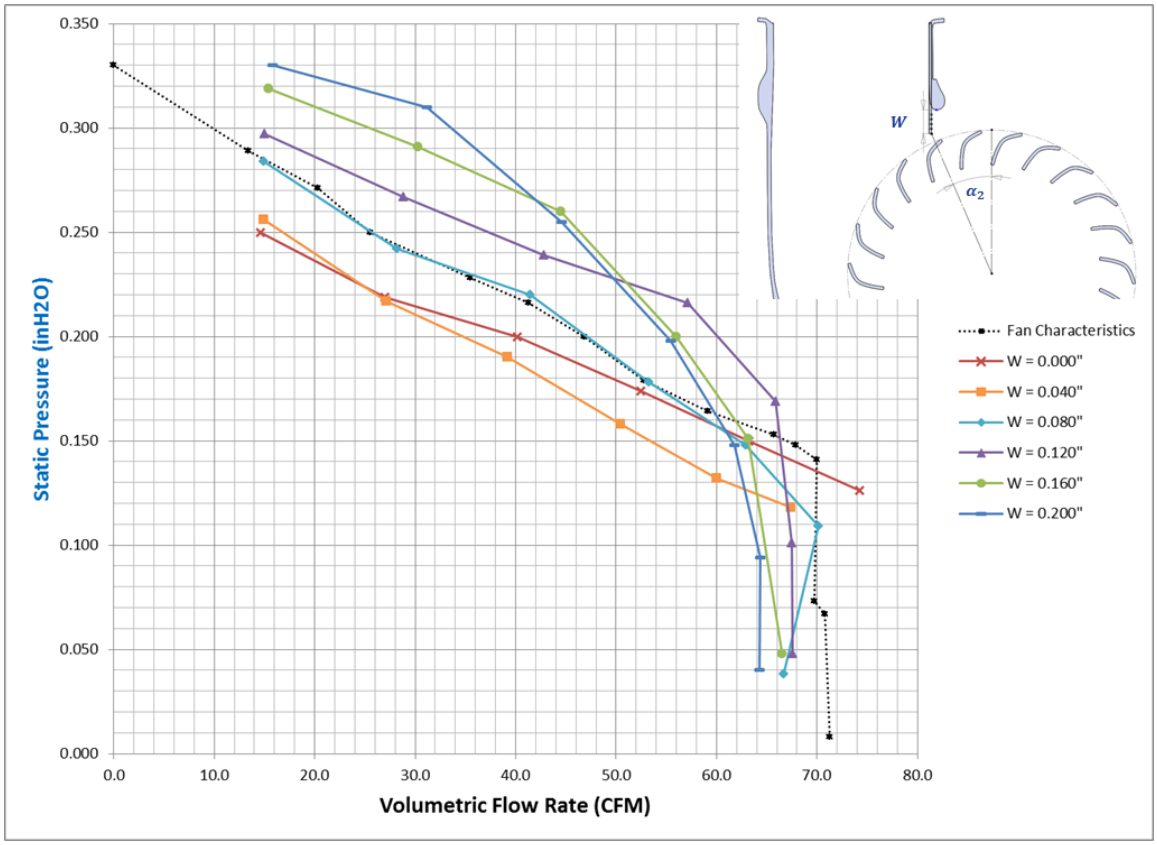

Figure 4-19 Static performance curves IG 0: W = length added to vortex wall

Some of the streamline plots obtained during this experiment are shown in Figure 4-20 and Figure 4-21. These plots show that the flow is more stable and the streamlines are closely packed as the gap between the vortex wall and the impeller is reduced. In Figure 4-20, W = 0.00" shows unstable behavior especially in the bottom half of the inlet geometry and near the duct. This unstable behavior worsens with an increase in the volumetric flow rate (see Figure 4-21). In comparison, the streamline plot for W = 0.12" shows stable flow with a strong vortex in the bottom half of inlet geometry near the impeller. The size of this vortex is reduced considerably at 55 CFM (see Figure 4-21). In the streamlines plot for W = 0.20" at 40 CFM there is a vortex in the bottom half of the inlet geometry near the impeller which is similar to the one found for W = 0.12", but smaller in size. However, at 55 CFM for W = 0.20" the vortex has grown significantly.

In addition, in both figures, for W = 0.00" reversed flow is visible above the impeller. This reversed flow reduces the effective suction region of the fan. Also, for W = 0.12" there are very little signs of reversed flow, and for W = 0.20" there are no visible signs. This confirms that reducing the ratio (ε_2/D_2) stops the flow from coming back from the discharge to the suction region which increases the overall static performance of the fan.

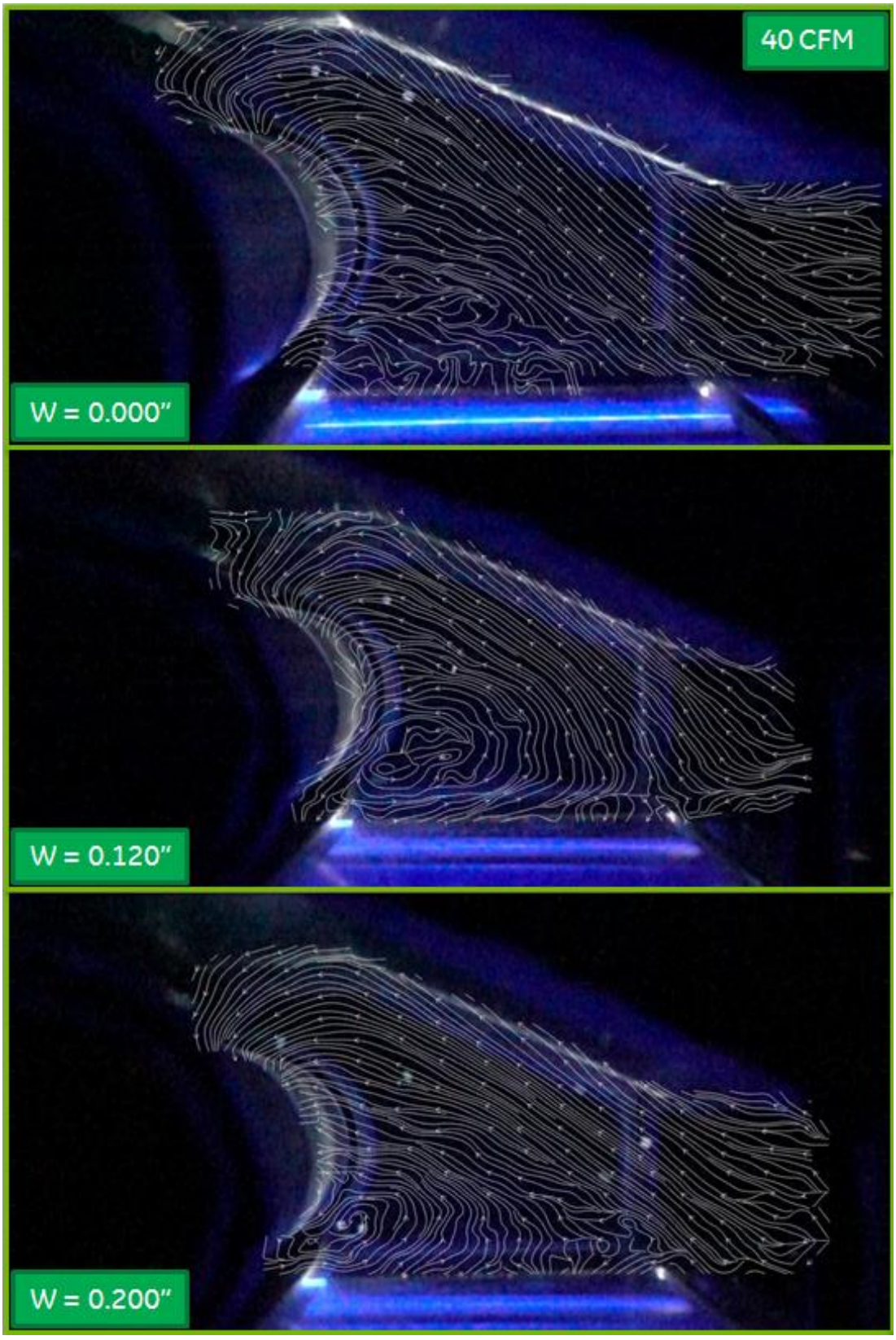

Figure 4-20 Streamlines plot IG 0: W = length added to vortex wall (40 CFM)

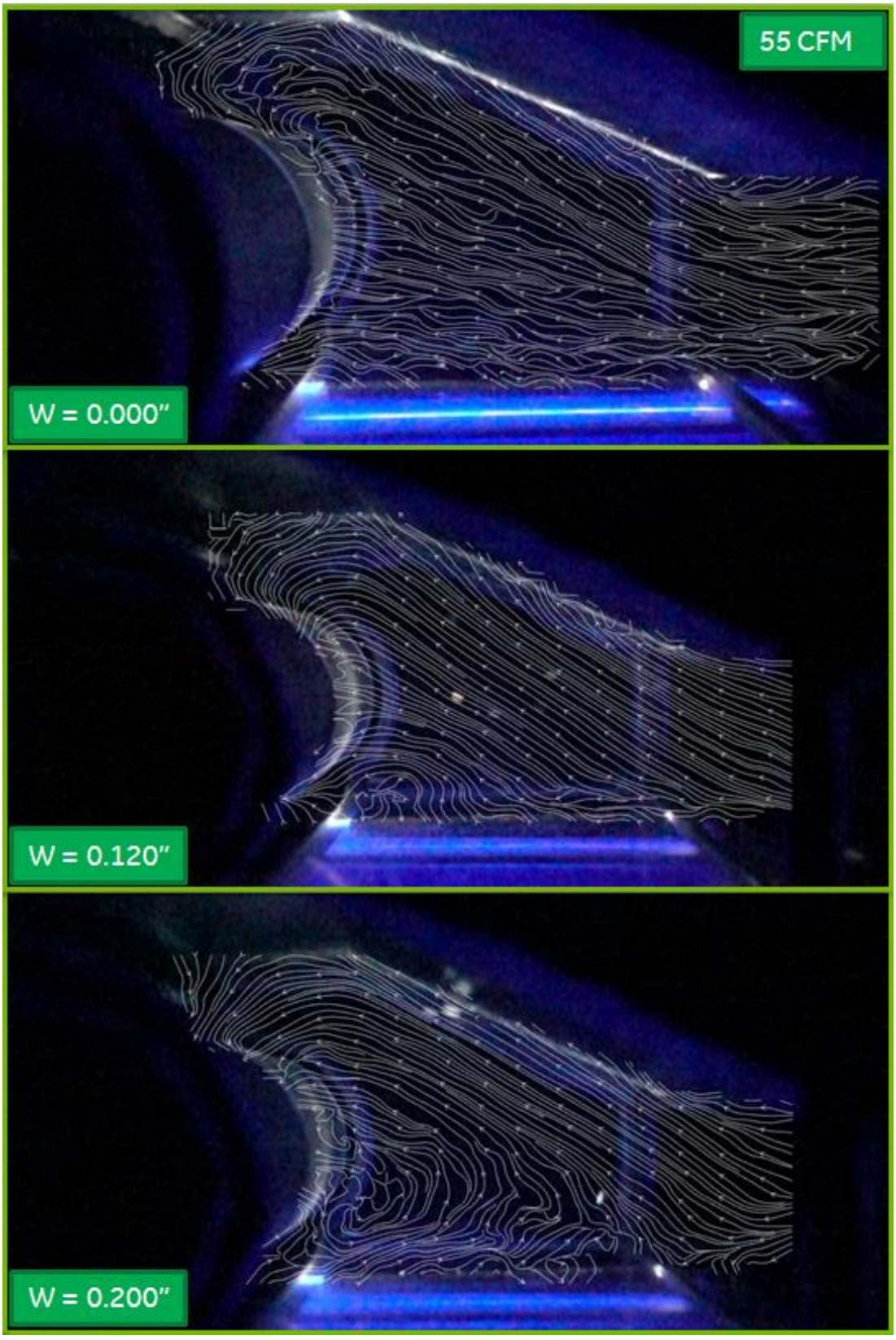

Figure 4-21 Streamlines plot IG 0: W = length added to vortex wall (55 CFM)

Overall, these streamline plots correlate with the static performance plot shown in Figure 4-19. For example, at 40 CFM, the highest performance was found for W = 0.20" and the corresponding streamline plot was more stable and presented a smaller vortex. Similarly, at 55 CFM, the highest performance was found for W = 0.12". Also, the corresponding streamline plot was more stable and presented the smaller vortex. This experiment proves that designing a fan inlet that reduces the ratio (ε_2/D_2) is a viable and simple way of improving performance for cross-flow fans.

In general if a given inlet geometry reduces fan performance by more than 25% compared to its performance with a fully open inlet, this will be considered undesirable. Another way to look at the drop in performance is to find the average performance relative to the performance of the fan with a fully open inlet. This was calculated for each case (see Table 4-2). The average performance relative to a fully open inlet was calculated from the static pressure at twelve points going from 15 to 70 CFM in increments of 5 CFM. These values were interpolated from the performance curves measured. The ratio of the static pressure with inlet geometry to the static pressure of the fully open inlet condition was calculated for each point, and the resultant ratios were averaged to obtain the average performance relative to the fan.

Table 4-2 Average relative performance for each inlet geometry

Inlet Geometry	Static Pressure (inH_2O) at given flow (CFM)												Average Performance Relative to the open Fan
	15 CFM	20 CFM	25 CFM	30 CFM	35 CFM	40 CFM	45 CFM	50 CFM	55 CFM	60 CFM	65 CFM	70 CFM	
IG 0	0.249	0.237	0.224	0.215	0.207	0.200	0.190	0.179	0.168	0.157	0.146	0.137	92%
IG 1	0.217	0.207	0.196	0.186	0.175	0.166	0.157	0.147	0.135	0.124	0.119	0.115	77%
IG 2	0.196	0.186	0.176	0.167	0.157	0.149	0.140	0.128	0.114	0.105	0.099		62%
IG 3	0.181	0.172	0.162	0.154	0.145	0.135	0.125	0.114	0.100	0.084			51%
IG 4	0.159	0.147	0.137	0.128	0.119	0.108	0.095	0.079					34%
IG 5	0.137	0.128	0.119	0.111	0.098	0.084	0.073	0.061					28%
IG 6	0.121	0.111	0.104	0.097	0.087	0.079	0.070	0.055					25%
IG 7	0.182	0.174	0.165	0.152	0.139	0.128	0.115	0.096	0.082				44%
IG 8	0.225	0.213	0.201	0.191	0.182	0.168	0.153	0.139	0.126	0.116	0.109	0.103	76%
IG 9	0.244	0.231	0.218	0.208	0.199	0.189	0.175	0.162	0.151	0.140	0.133	0.129	86%
IG 10	0.242	0.230	0.219	0.211	0.204	0.197	0.187	0.178	0.167	0.157	0.146	0.138	91%
IG 11	0.248	0.235	0.222	0.213	0.206	0.199	0.190	0.181	0.169	0.157	0.144	0.132	92%
IG 12	0.161	0.152	0.142	0.131	0.120	0.110	0.097	0.082					35%
IG 13	0.197	0.188	0.178	0.164	0.151	0.140	0.130	0.114	0.097	0.092	0.086	0.083	63%
IG 14	0.205	0.194	0.184	0.172	0.159	0.148	0.136	0.126	0.116	0.108	0.099	0.092	68%
IG 15	0.215	0.203	0.191	0.185	0.178	0.168	0.156	0.145	0.137	0.129	0.125	0.122	78%
Open Fan	0.285	0.272	0.252	0.240	0.229	0.219	0.205	0.189	0.174	0.163	0.154	0.144	100%

The inlet geometries that had a relative performance larger than 75% were considered appropriate solutions. From Table 4-2, only inlet geometries 0, 1, 8, 9, 10, 11, and 15 meet this condition; therefore, all other inlet geometries should be avoided. However, for this specific fan, the ratio (ε_2/D_2) is larger than 3.5%; therefore, reducing this ratio might allow the use of other inlet geometries as well.

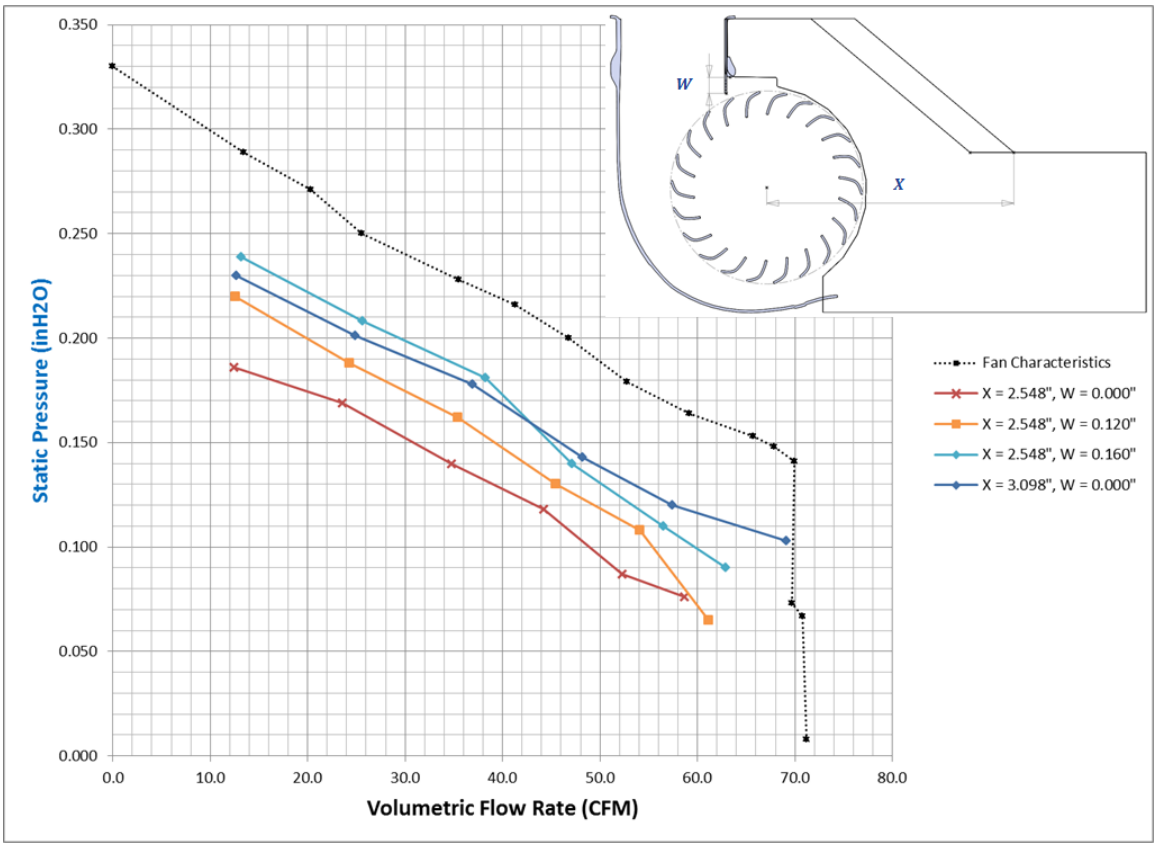

Figure 4-22 Static performance curves IG 7: W = length added to vortex wall

Inlet geometry 7 was used to validate this assumption. The experiment consisted of measuring the performance of the fan with inlet geometry 7 and different vortex wall lengths. The static performance curves measured in this experiment are shown in Figure 4-22. As shown, extending the vortex wall by 0.16" improves the performance of the fan considerably. This case shows slightly better static performance at lower flows than inlet geometry 8. The decrease in performance seen at higher volumetric flow rate is consistent with increasing the vortex wall position angle (α_2). However, the average performance relative to the open fan curve improved from 65% to above 77% which is considered acceptable.

Reducing the ε_2/D_2 ratio should improve the performance of inlet geometries 2, 3, 13, and 14 to above the 75% threshold. However, as the ratio ε_2/D_2 decreases, the noise of the fan increases. This is consistent with the findings of Ikegami and Murata (1966) and should be investigated in depth in future studies.

5. CONCLUSIONS AND RECOMMENDATIONS

In this study it was demonstrated that visualization analysis can be used to correlate the performance losses in the suction region of a cross-flow fan. It was demonstrated that features like instability of the streamlines, effective suction area, vortex location and size, angle of flow entering the impeller, and others can be determined from the airflow visualization and that they can be related to cross-flow fan performance. The following conclusions were drawn from the fan-inlet combinations studied.

First, the distance to the expansion point (X) should be at least 3.1" from the center of the impeller or $0.811D_2$ from the outside diameter of the impeller. The optimal range, for the cross-flow fan studied, was found between 3.1" and 3.7". However, if the ratio ε_2/D_2 is reduced, as suggested in Section 5.3, this distance could change and new best values of X should be determined experimentally. Second, the distance to the top wall (Y) should not be higher than the upper portion of the vortex wall or 2.114" from the center of the impeller or 0.395 impeller diameters ($0.395D_2$) from the outside diameter of the impeller. Third, of the expansion angles (θ) tested, it was concluded that θ should be 40 degrees. Nevertheless, larger angles should be tested. In general, for the expansion wall a sudden expansion will perform better than a gradual expansion. Finally, the angle of a vane guide near the vortex wall (δ) has little effect on the fan performance, although it could have a slightly negative effect on performance for an angle larger than 30 degrees.

Some of the conclusions drawn from previous authors, as discussed in Chapter 2, were confirmed from the fan-inlet combinations tested. For example, it was verified that reducing the ratio of ε_2/D_2 to 7.66% or less improves the performance of the fan with the optimal being around 3.5%. These findings are consistent with the conclusions of Ikegami and Murata (1966). Also consistent with their research, it was noticed that reducing this ratio increases the fan performance at the expense of an increase in noise and vibration of the fan. Also, it was confirmed that as α_2 increases the maximum volumetric flow rate decreases.

In conclusion, in this study some inlet geometries were identified that preserve up to 75% of the original open fan performance in constricted spaces. Furthermore, critical design variables of the proposed cross-flow fan inlet geometry were identified. For these design variables typical ranges were suggested to set the bases of future optimization studies.

Future Work

The following is a series of suggestions of future work topics in regards to similar type of studies. The relationship between noise and the ratio ε_2/D_2 should be investigated to optimize the performance in function of noise. This will be particularly important since noise is a significant concern in most cross-flow fan applications. In addition, it would be useful to use a fully clear fan to study the inlet region, interior of the impeller, and discharge region of the fan. This would facilitate the mapping of the flow-field, and it should help identifying optimal parameters in normal operating conditions.

Several design variables are suggested for future research. First, a possible design variable to investigate is the height of the duct, in order to characterize the performance

loss related to reducing the height of the duct, as this variable could highly influence the performance of the fan. Second, study the effect of rotating the fan relative to the duct is recommended. In this study, for many of the fan-inlet configurations, a vortex appears in the bottom wall. This could be alleviated by rotating the fan backwards which could be translated to improved performance.

Regarding the PTV methodology developed in this study, future work should focus on measuring the accuracy of the PTV system and comparing it to conventional PIV systems. This will help to determine areas of improvement as well as other possible applications.

REFERENCES

ANSI/AMCA, 2000. *ANSI/AMCA Standard 210, ANSI/ASHRAE Standard 51,* s.l.: Air Movement and Control Association International, Inc. and American Society of Heating, Refrigerating and Air Conditioning Engineers, Inc..

Cao, X., Liu, J., Jiang, N. & Chen, Q., 2014. Particle Image Velocimetry measurement of indoor airflow field: A review of the technologies and applications. *Energy and Buildings 69,* pp. 367-380.

Cory, B., 2005. *Fans & Ventilation: A Practical Guide,* New York: Elsevier in association with Roles & Associates Ltd.

Eck, B., 1973. *Fans.* New York: Pergamon Press Ltd..

Electromatic Equipment Co., Inc., 2007. *Check-line by Electromatic.* [Online] Available at: https://www.checkline.com/product/CDT-1000HD
[Accessed 1 November 2016].

Fluke Corporation, 2006. *Fluke 922 Airflow Meter/Micromanometer.* [Online] Available at: http://en-us.fluke.com/products/hvac-iaq-tools/fluke-922-hvac-iaq.html#techspecs
[Accessed 1 November 2016].

Fukutomi, J. & Nakamura, R., 2005. Performance and Internal Flow of Cross-Flow Fan with Inlet Guide Vane. *JSME International Journal,* pp. 763-769.

Fu, S., Biwole, P. H. & Mathis, C., 2015. Particle Tracking Velocimetry for indoor airflow field: A review. *Building and Environment 87,* pp. 34-44.

Gabi, M. & Klemm, T., 2004. Numerical and Experimental Investigations of Cross-Flow Fans. *Journal of Computational and Applied Mechanics,* pp. 251-261.

Gonzalez Hernandez, M. A. et al., 2013. Design Methodology for a Quick and Low-Cost Wind Tunnel. *InTech,* pp. 3-28.

Heeley, D., 2005. *Understanding Pressure and Pressure Measurements,* Phoenix, AZ: Freescale Semiconductor.

Ikegami, H. & Murata, S., 1966. *A Study of the cross flow fan: Part 1, A theoretical analysis,* Osaka: Osaka University.

Jorgensen, R., 1983. *Fan Engineering.* Buffalo, New York: Buffalo Forge Company.

Kerho, M. F. & Bragg, M. B., 1994. Neutrally buoyant bubbles used as flow tracers in air. *Experiments in Fluids 16,* pp. 393-400.

Kim, T.-A., Kim, D. W., Park, S. K. & Kim, Y. J., 2008. Performance of a cross-flow fan with various shapes of a rearguider and an exit duct. *Journal of Mechanical Science and Technology,* pp. 1876-1882.

Mathworks, 2015. *Mathworks Documentation: Motion-Based Multiple Object Tracking.* [Online]
Available at: https://www.mathworks.com/help/vision/examples/motion-based-multiple-object-tracking.html
[Accessed 1 December 2016].

Mazur, J. S., 1984. *A Study of the Cross Flow Fan,* Detroit, Michigan: Wayne State University.

Mortier, P., 1893. United States of America, Patent No. 459,135.

Murata, S. & Nishihara, K., 1976. An experimental study of cross flow fan (1st Report, Effects of Housing Geometry on the Fan Performance). *Bulletin of the JSME,* pp. 314-321.

Murata, S. & Nishihara, K., 1976. An experimental study of cross flow fan (2nd Report, Movements of eccentric vortex inside impeller). *Bulletin of the JSME,* pp. 322-329.

Murata, S. et al., 1978. A study of Cross Flow Fan with Inner Guide Apparatus. *Bulletin of the JSME,* pp. 681-688.

Porter, A. M. & Markland, E., 1970. A study of the cross flow fan. *Journal of Mechanical Engineering Science,* pp. 421-431.

Rae Jr., W. H. & Pope, A., 1984. *Low-Speed Wind Tunnel Testing.* s.l.:John Wiley & Sons, Inc..

Rayle Jr., R. E., 1949. *An Investigation of the Influence of Orifice Geometry on Static Pressure Measurements,* Cambridge, MA: Massachusetts Institute of Technology.

Rezig, S., Toscano, R., Rusaouen, G. & Lozano, V., 2015. Fuzzy Kalman Filter for 3D Lagrangian Particle Tracking using Multi-Scale Bubble Detection. *Energy Procedia 78,* pp. 3078-3083.

Sage Action, Inc., 2008. *Helium Bubble Generator: Description and Operating Instructions.* Apache Junction, Arizona: Sage Action, INC.

Sage Action, 2016. *Sage Action Home Site.* [Online]
Available at: http://www.sageaction.com/
[Accessed 1 12 2016].

Shih, Y.-C., Hou, H.-C. & Chiang, H., 2008. On similitude of the cross flow fan in a split-type air-conditioner. *Applied Thermal Engineering,* pp. 1853-1864.

Stacharska-Targosz, J., 2013. Regulation of flow rate generated by cross flow fan with use of internal vane. Experimental and Numerical Results. *Technical Transactions Mechanics,* pp. 365-372.

Strike, N. D., 2014. *Fan Efficiency: An Increasingly Important Selection Criteria.* [Online]
Available at: http://www.nmbtc.com/fans/white-papers/fan_efficiency_important_selection_criteria/
[Accessed 1 12 2016].

Sun, K. et al., 2015. Experimental and numerical investigations on the eccentric vortex of the cross flow fan. *International Journal of Refrigeration,* pp. 146-155.

Thielicke, W. & Stamhuis, E., 2014. PIVlab - Towards User-friendly, Affordable and Accurate Digital Particle Image Velocimetry in MATLAB. *Journal of Open Research Software 2.*

Toffolo, A., 2004. On the theoretical link between design parameters and performance in cross-flow fans: a numerical and experimental study. *Computers & Fluids,* pp. 49-66.

Toffolo, A., Lazzaretto, A. & Martegani, A. D., 2004. An experimental investigation of the flow field pattern within the impeller of a cross-flow fan. *Experimental Thermal and Fluid Science,* pp. 53-64.

Tsurusaki, H. et al., 1996. Study of Cross-Flow-Fan Internal Flow by Flow Visualization. *JSME International Journal,* pp. 540-545.

Tuckey, P. R., 1983. *The aerodynamics and performance of a cross flow fan,* s.l.: Durham Theses, Durham University.

Universal Laser Systems, 2011. *IL Platform Series,* s.l.: Universal Laser Systems.

APPENDICES

Appendix A: Matlab Program Logic

Appendix B: Static Efficiency Curves

Appendix C: Performance Curves using Dimensionless Coefficients

Appendix D: Efficiency Curves using Dimensionless Coefficients

Appendix E: Performance Test Measurements

Appendix A: Matlab Program Logic

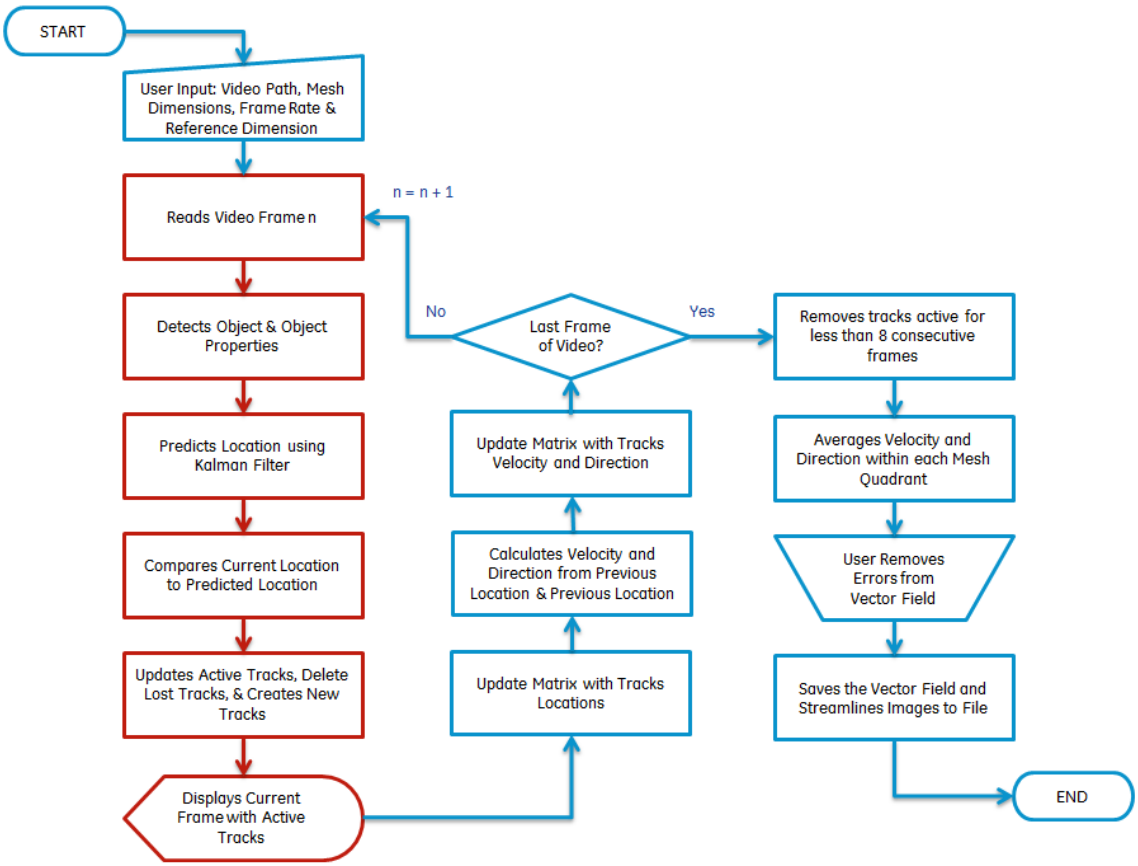

Figure Appendices-1 Program logic diagram (red: from Matlab example)

Appendix B: Static Efficiency Curves

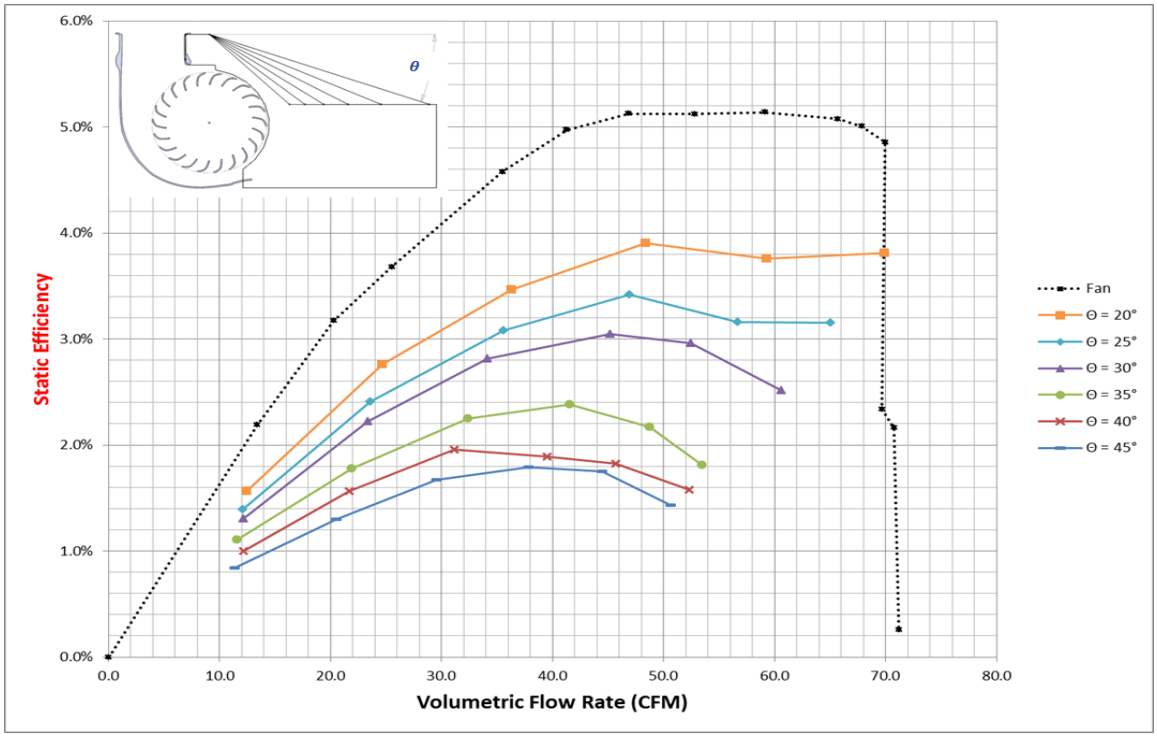

Figure Appendices-2 Static Efficiency: θ = expansion angle

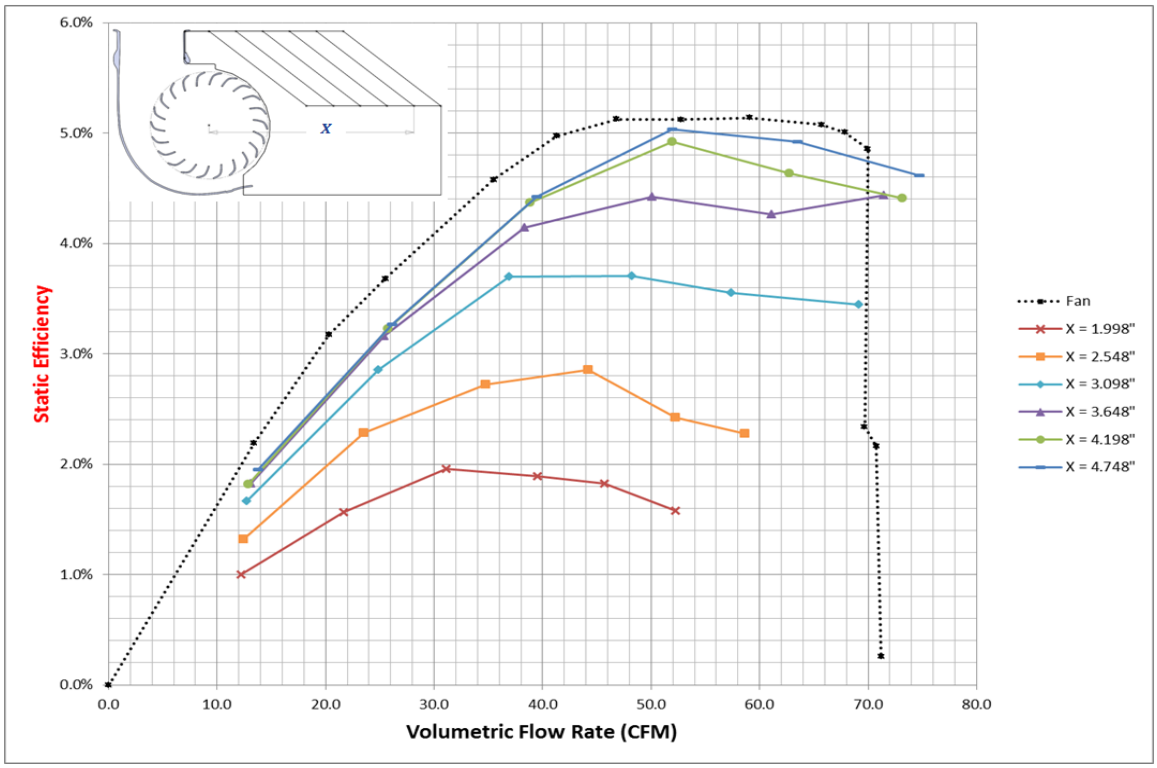

Figure Appendices-3 Static Efficiency: X = distance to expansion point

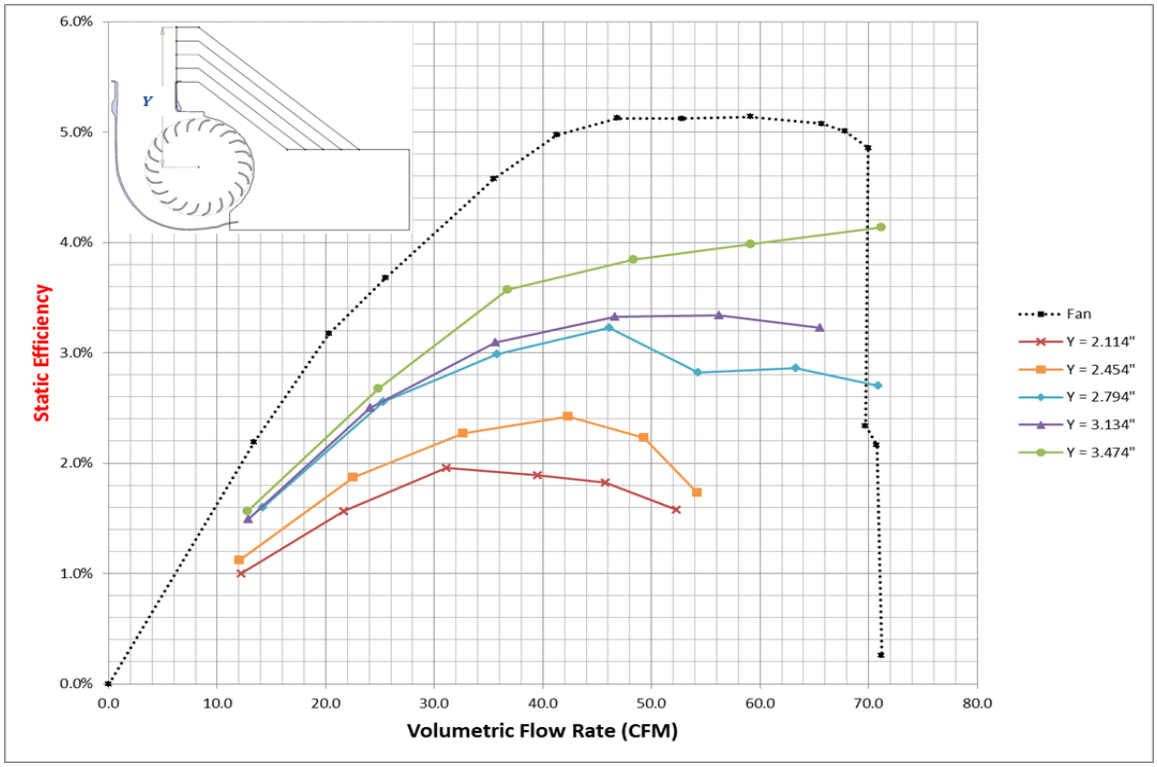

Figure Appendices-4 Static Efficiency: Y = distance to top wall

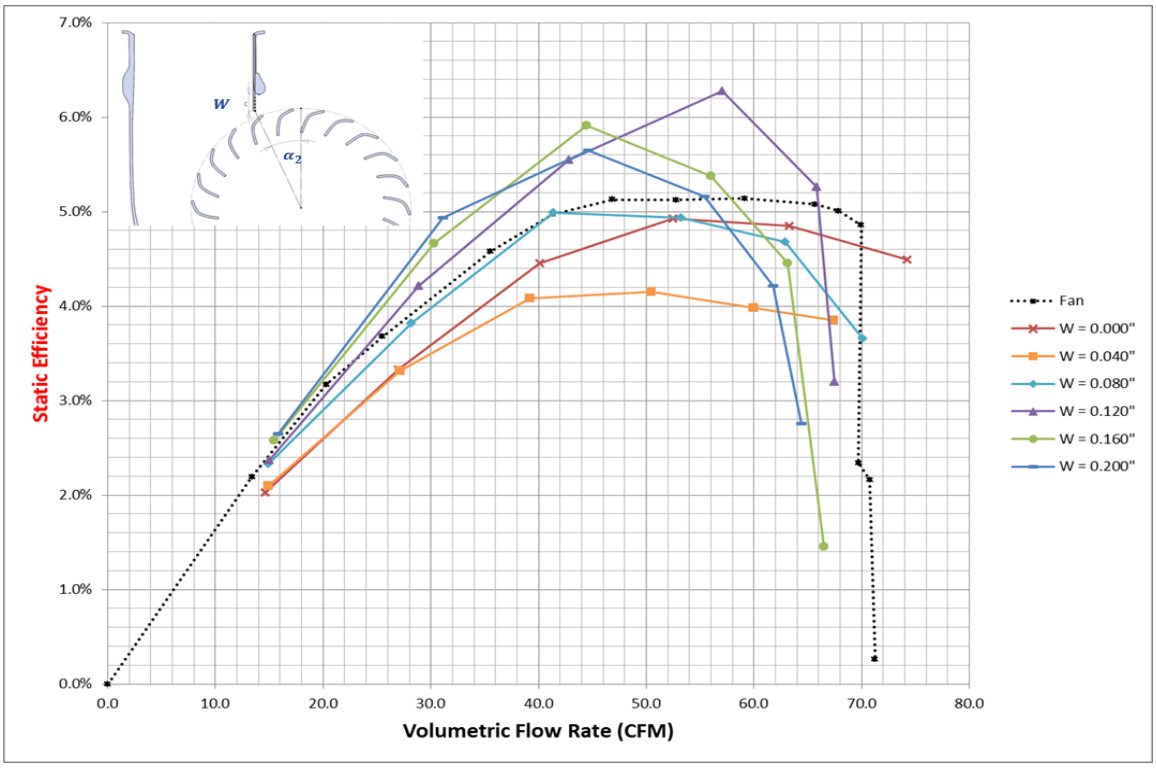

Figure Appendices-5 Static Efficiency: W = vortex wall added length

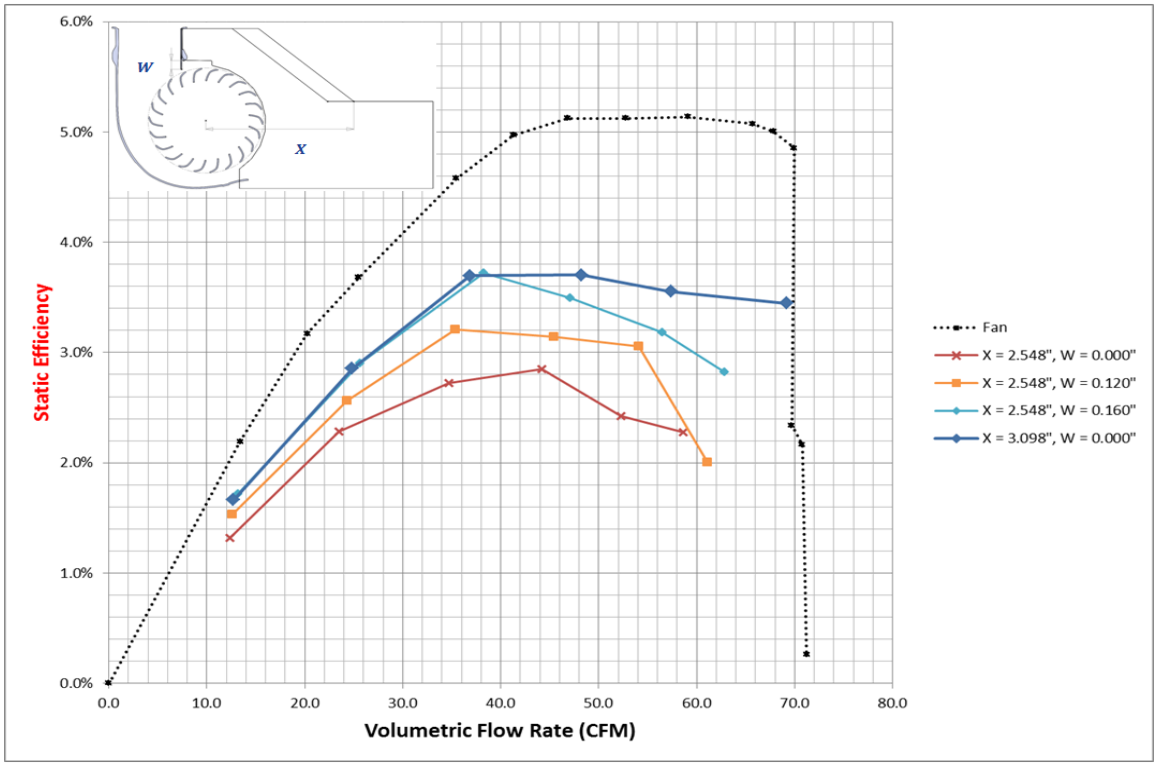

Figure Appendices-6 Static Efficiency: X and W

Appendix C: Performance Curves using Dimensionless Coefficients

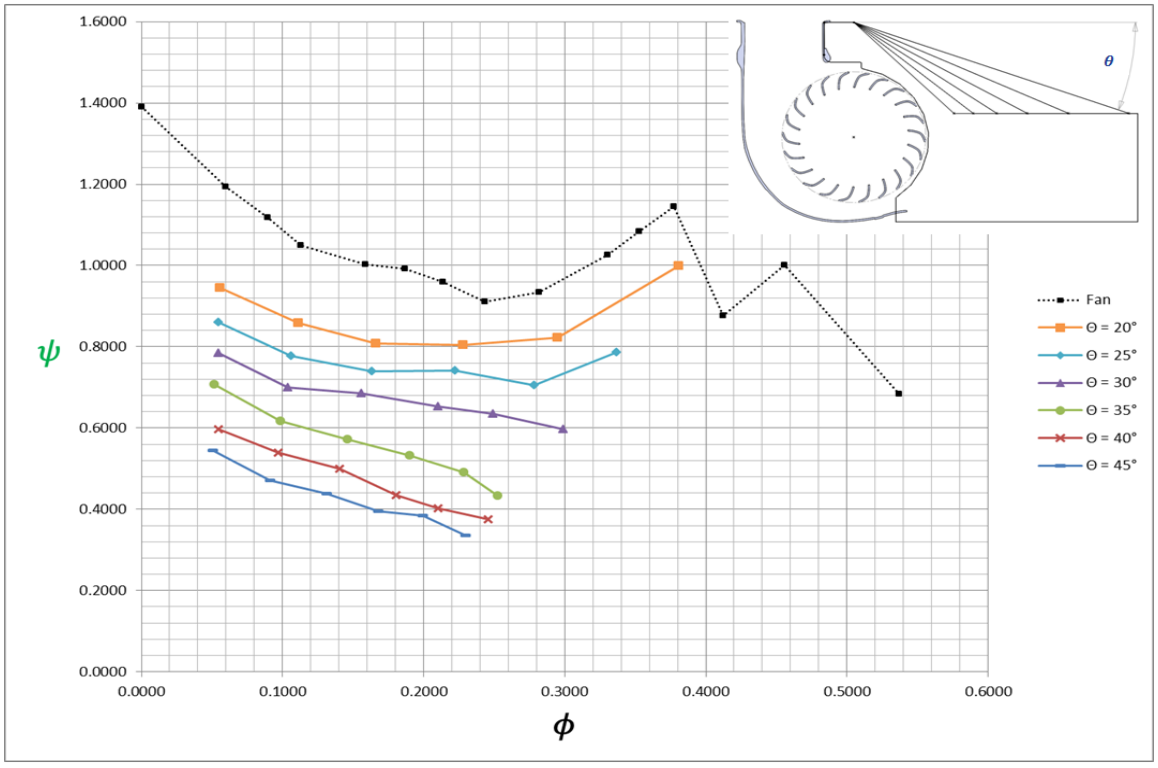

Figure Appendices-7 Dimensionless performance: θ

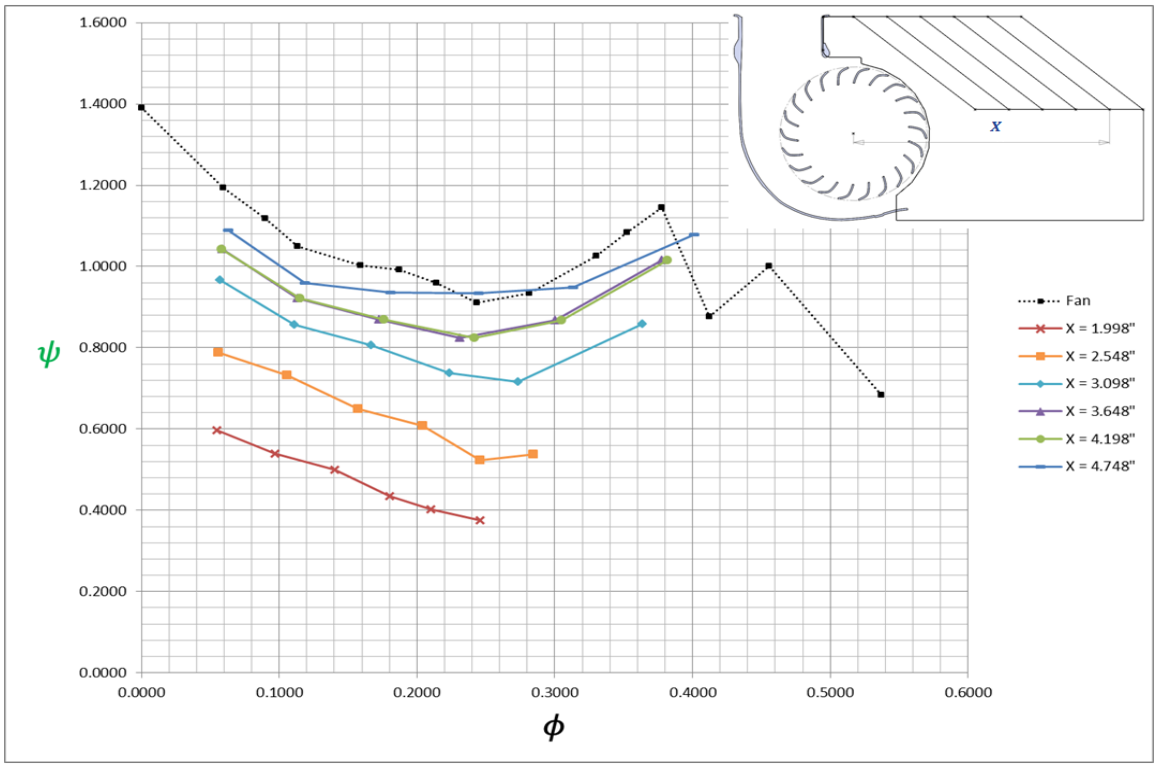

Figure Appendices-8 Dimensionless performance: X

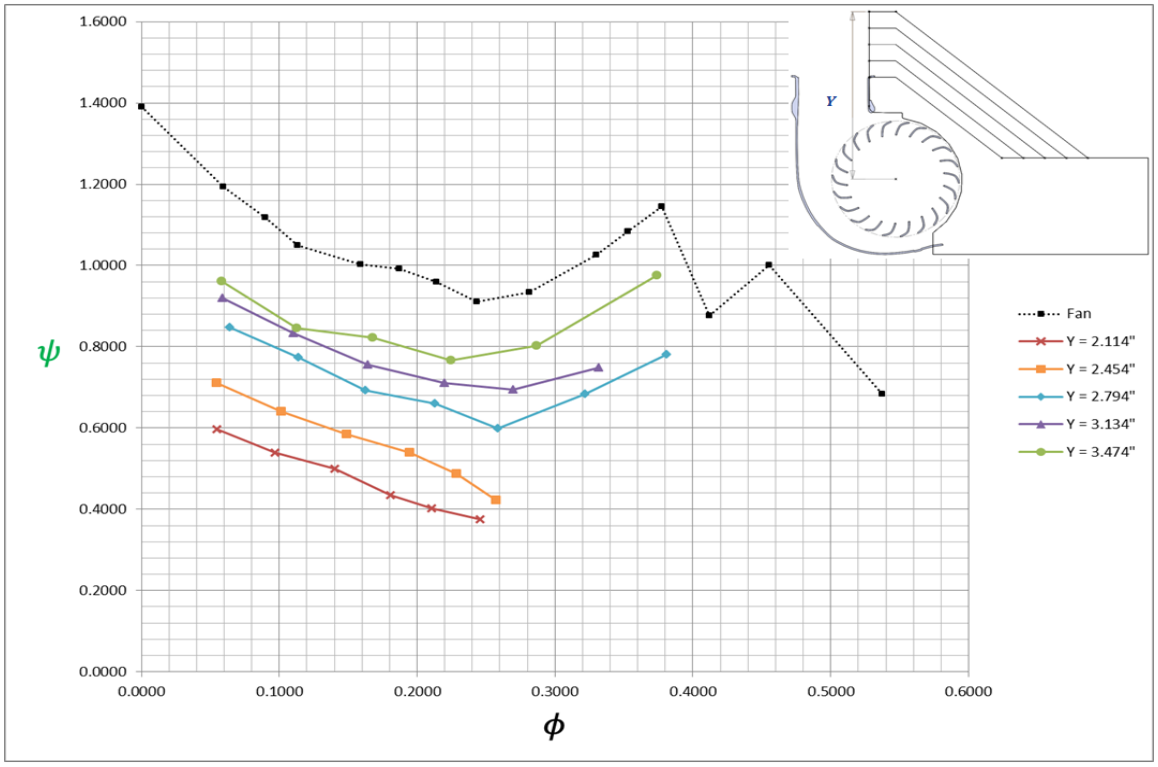

Figure Appendices-9 Dimensionless performance: Y

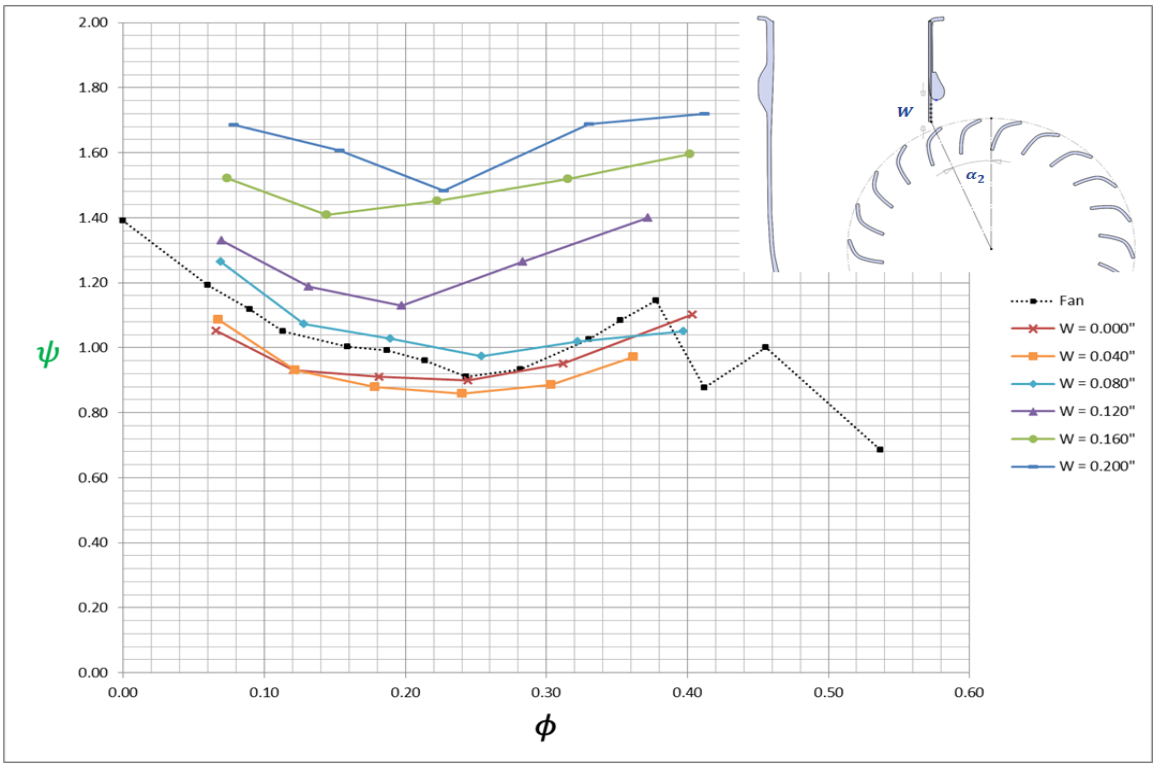

Figure Appendices-10 Dimensionless performance: W

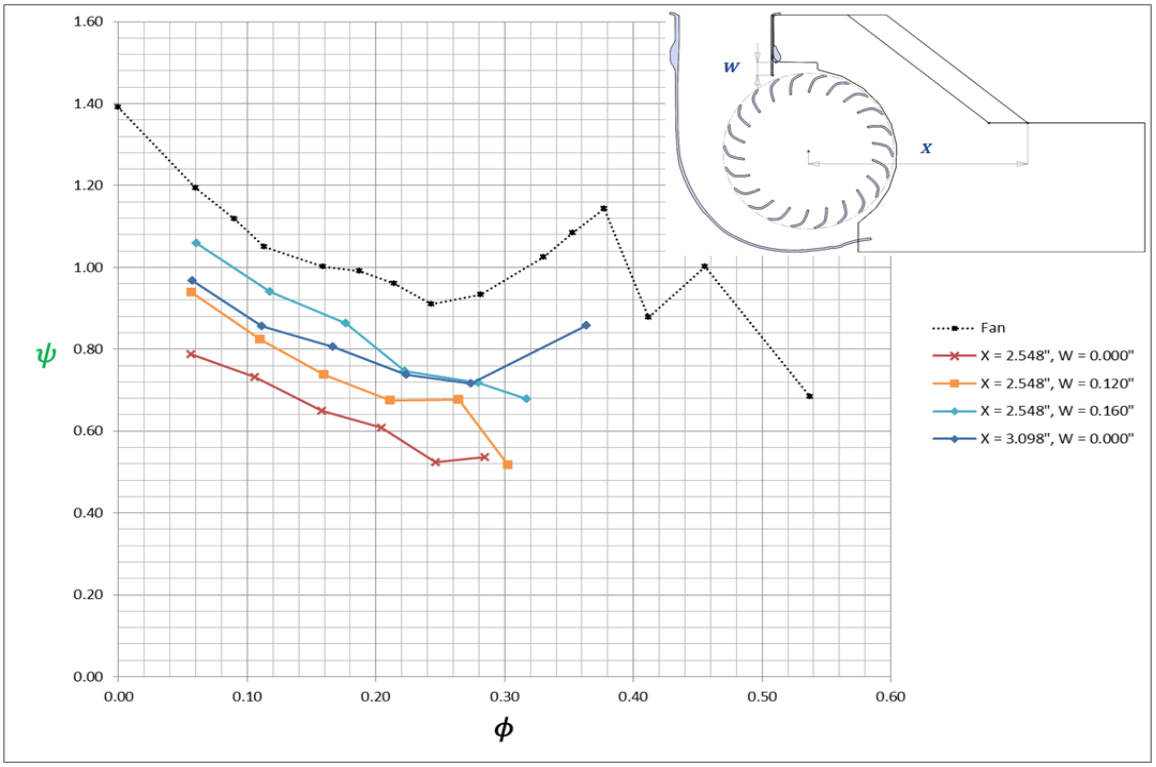

Figure Appendices-11 Dimensionless performance: X and W

Appendix D: Efficiency Curves using Dimensionless Coefficients

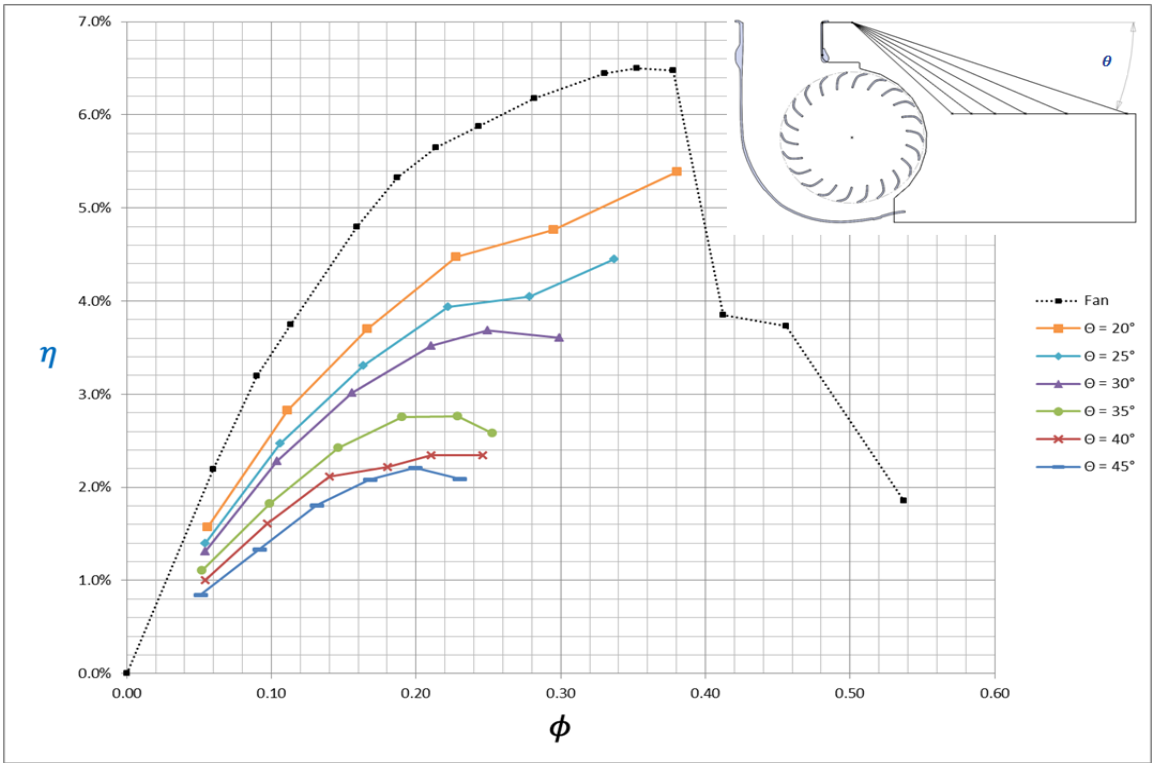

Figure Appendices-12 Dimensionless efficiency: θ

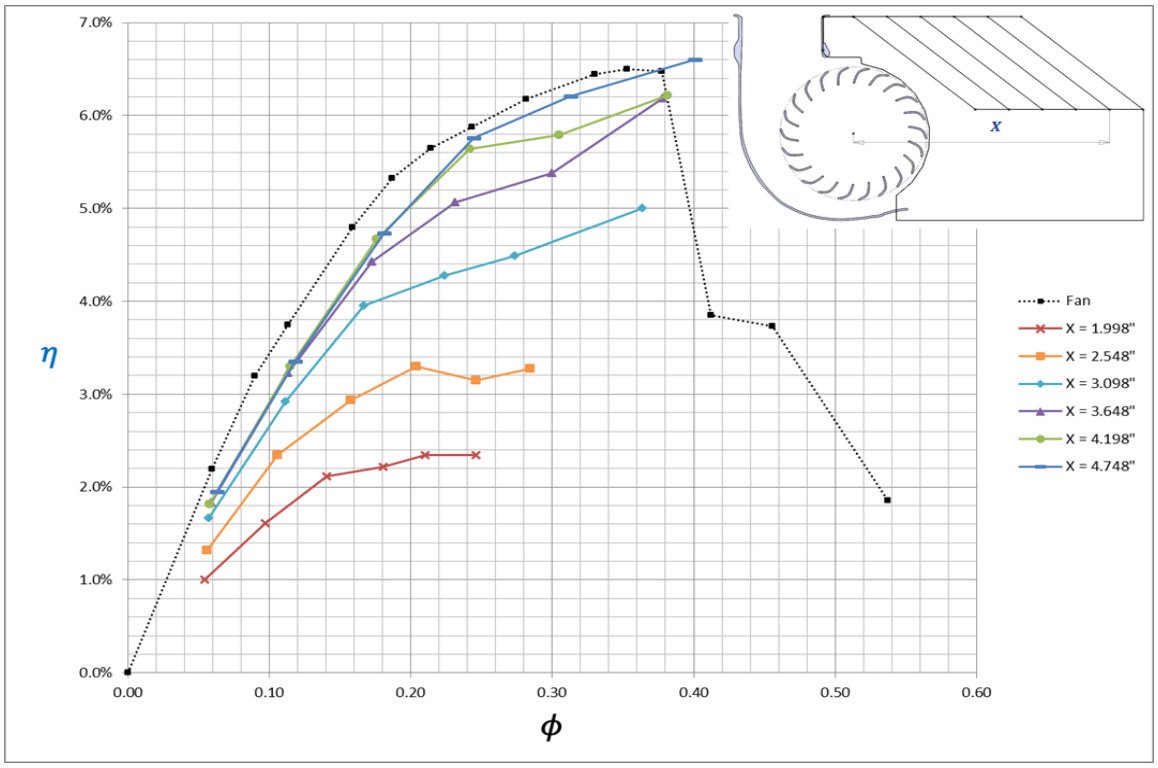

Figure Appendices-13 Dimensionless efficiency: X

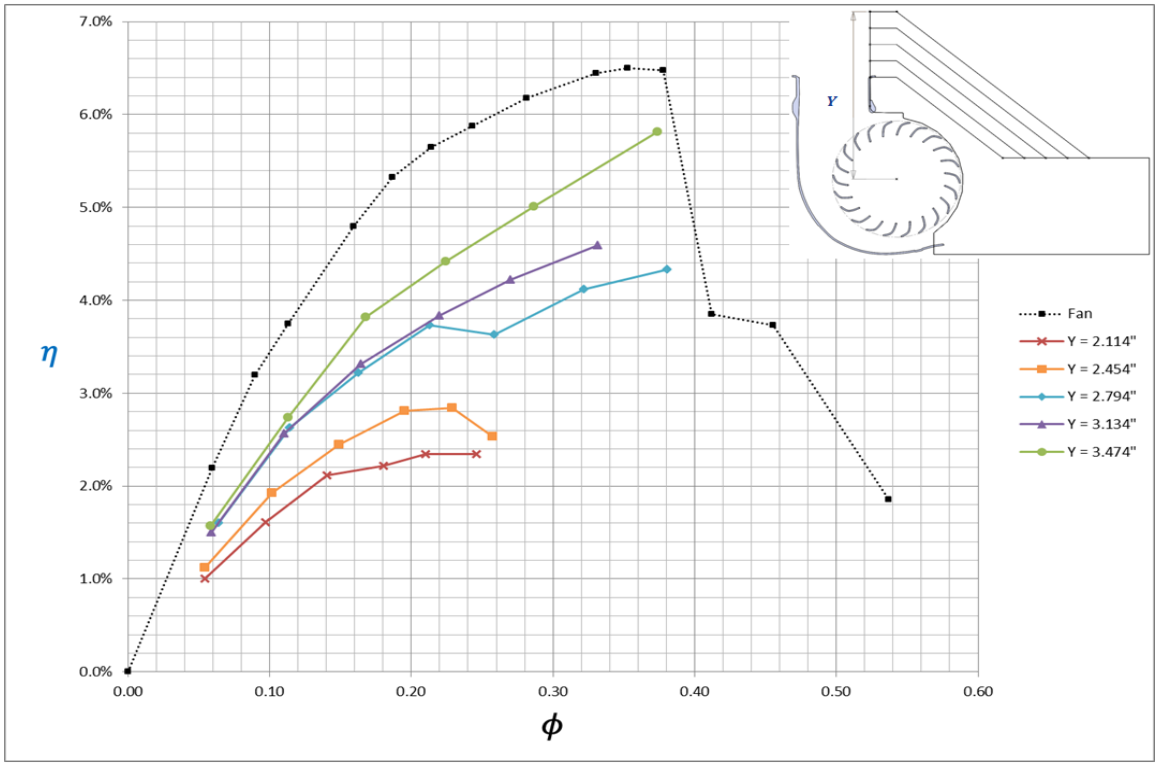

Figure Appendices-14 Dimensionless efficiency: Y

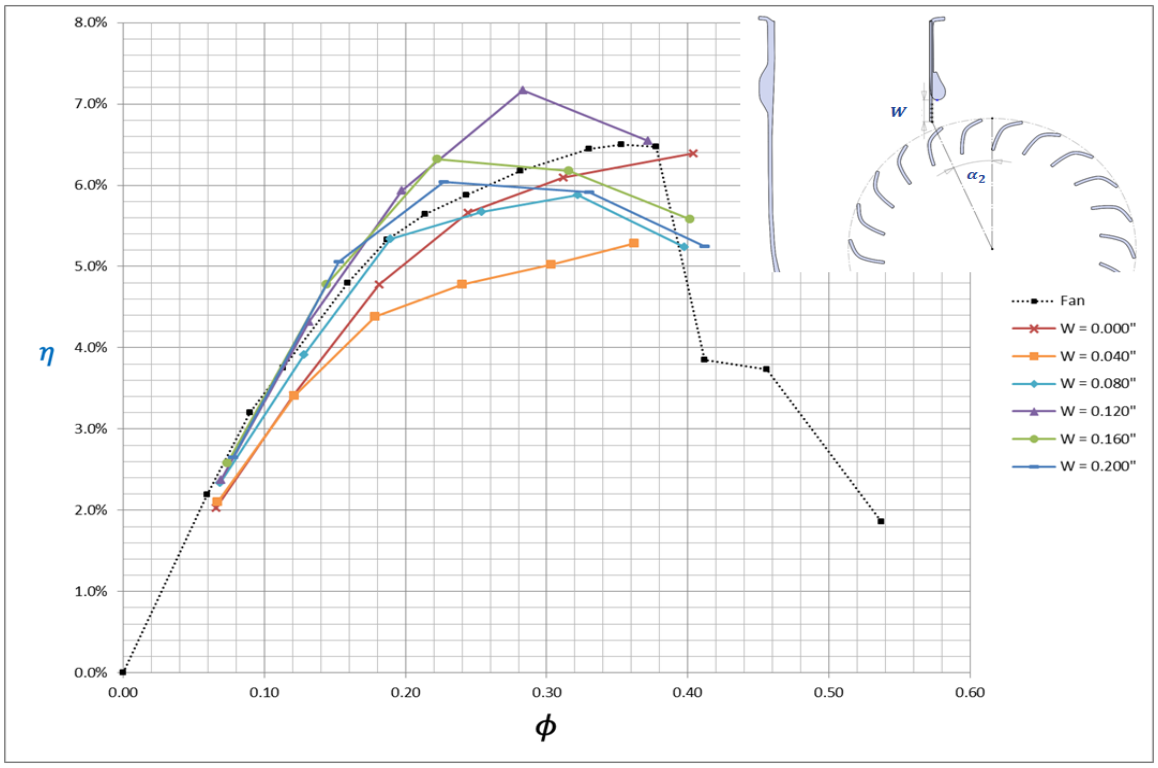

Figure Appendices-15 Dimensionless efficiency: W

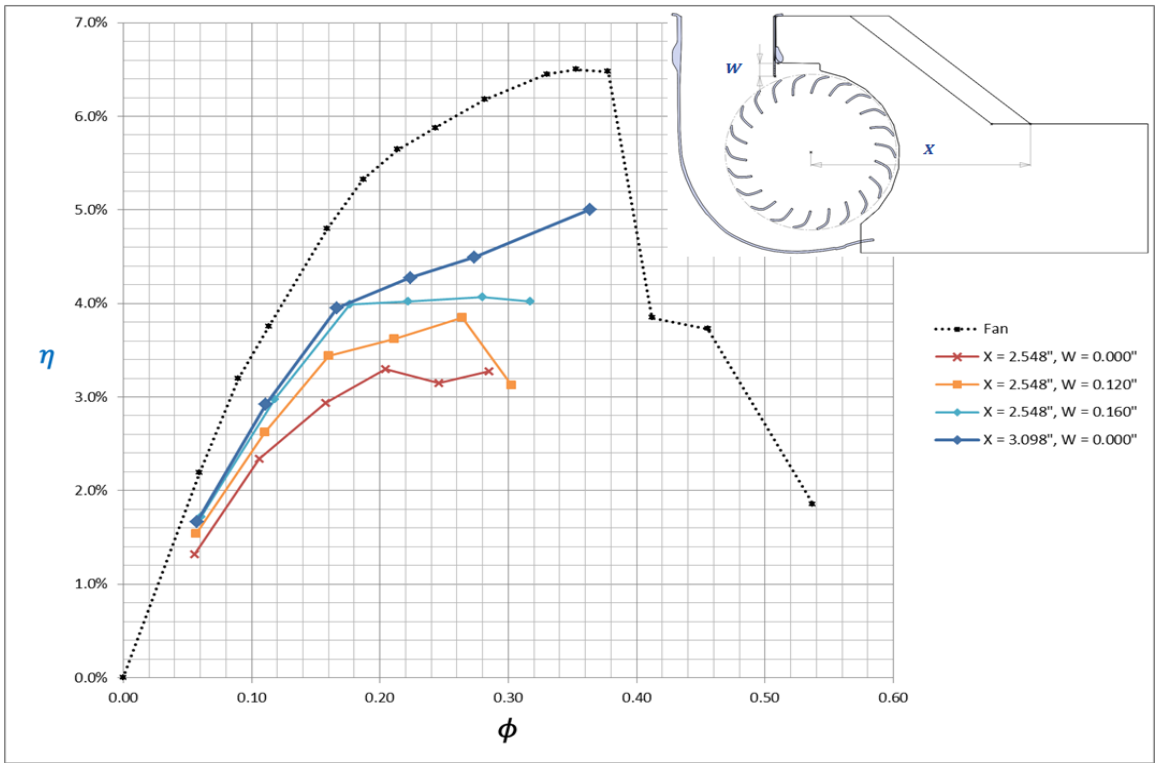

Figure Appendices-16 Dimensionless efficiency: X and W

Appendix E: Performance Test Measurements

Table Appendices-1 Performance measurements: inlet geometry 0

Temp (F)	ΔP4-5 (inH20)	Flow (CFM)	ΔP1-2 (inH2O)	Power (W)	Fan Speed (RPM)	Fan Static Efficiency	ψ	ϕ	η
70.0	0.076	14.6	0.250	21.2	3171	2.0%	1.05	0.07	2.0%
70.0	0.254	27.0	0.219	20.9	3192	3.3%	0.93	0.12	3.4%
70.0	0.554	40.1	0.200	21.2	3155	4.5%	0.91	0.18	4.8%
70.0	0.940	52.5	0.174	21.8	3063	4.9%	0.90	0.24	5.7%
70.0	1.361	63.2	0.150	23.0	2890	4.9%	0.95	0.31	6.1%
70.0	1.870	74.2	0.126	24.5	2620	4.5%	1.10	0.40	6.4%
70.0	1.564	67.8	0.051	26.1	1539	1.6%	1.71	0.63	2.9%

Table Appendices-2 Performance measurements: inlet geometry 1

Temp (F)	ΔP4-5 (inH20)	Flow (CFM)	ΔP1-2 (inH2O)	Power (W)	Fan Speed (RPM)	Fan Static Efficiency	ψ	ϕ	η
73.4	1.650	69.9	0.114	24.6	2617	3.8%	1.00	0.38	5.4%
73.4	1.190	59.3	0.125	23.2	2864	3.8%	0.82	0.29	4.8%
73.4	0.795	48.3	0.151	22.0	3023	3.9%	0.80	0.23	4.5%
73.4	0.451	36.3	0.172	21.2	3109	3.5%	0.81	0.17	3.7%
73.4	0.211	24.7	0.197	20.7	3161	2.8%	0.86	0.11	2.8%
73.4	0.055	12.4	0.222	20.7	3160	1.6%	0.95	0.06	1.6%

Table Appendices-3 Performance measurements: inlet geometry 2

Temp (F)	ΔP4-5 (inH20)	Flow (CFM)	ΔP1-2 (inH2O)	Power (W)	Fan Speed (RPM)	Fan Static Efficiency	ψ	ϕ	η
74.4	1.427	65.0	0.099	24.0	2750	3.2%	0.79	0.34	4.4%
74.4	1.088	56.7	0.109	23.0	2902	3.2%	0.71	0.28	4.1%
74.4	0.748	46.9	0.137	22.1	3009	3.4%	0.74	0.22	3.9%
74.4	0.434	35.6	0.156	21.2	3105	3.1%	0.74	0.16	3.3%
74.4	0.193	23.6	0.179	20.6	3170	2.4%	0.78	0.11	2.5%
74.4	0.052	12.1	0.202	20.6	3164	1.4%	0.86	0.05	1.4%

Table Appendices-4 Performance measurements: inlet geometry 3

Temp (F)	ΔP4-5 (inH20)	Flow (CFM)	ΔP1-2 (inH2O)	Power (W)	Fan Speed (RPM)	Fan Static Efficiency	ψ	ϕ	η
71.9	1.245	60.6	0.082	23.2	2887	2.5%	0.60	0.30	3.6%
71.9	0.936	52.4	0.108	22.5	2995	3.0%	0.63	0.25	3.7%
71.9	0.698	45.2	0.125	21.8	3061	3.0%	0.65	0.21	3.5%
71.9	0.401	34.1	0.147	21.0	3119	2.8%	0.69	0.16	3.0%
71.9	0.190	23.4	0.165	20.4	3204	2.2%	0.70	0.10	2.3%
71.9	0.053	12.2	0.187	20.5	3182	1.3%	0.78	0.05	1.3%

Table Appendices-5 Performance measurements: inlet geometry 4

Temp (F)	ΔP4-5 (inH20)	Flow (CFM)	ΔP1-2 (inH2O)	Power (W)	Fan Speed (RPM)	Fan Static Efficiency	ψ	ϕ	η
73.3	0.974	53.5	0.065	22.6	3016	1.8%	0.43	0.25	2.6%
73.3	0.811	48.8	0.084	22.2	3040	2.2%	0.49	0.23	2.8%
73.3	0.590	41.5	0.105	21.5	3110	2.4%	0.53	0.19	2.8%
73.3	0.361	32.4	0.124	21.0	3150	2.2%	0.57	0.15	2.4%
73.3	0.168	21.9	0.142	20.6	3170	1.8%	0.62	0.10	1.8%
73.3	0.048	11.6	0.167	20.6	3171	1.1%	0.71	0.05	1.1%

Table Appendices-6 Performance measurements: inlet geometry 5

Temp (F)	ΔP4-5 (inH20)	Flow (CFM)	ΔP1-2 (inH2O)	Power (W)	Fan Speed (RPM)	Fan Static Efficiency	ψ	ϕ	η
72.0	0.927	52.3	0.055	21.4	3029	1.6%	0.38	0.25	2.3%
72.0	0.711	45.7	0.071	20.9	3098	1.8%	0.40	0.21	2.3%
72.0	0.535	39.5	0.085	20.9	3119	1.9%	0.43	0.18	2.2%
72.0	0.334	31.1	0.109	20.4	3159	2.0%	0.50	0.14	2.1%
72.0	0.164	21.7	0.125	20.4	3181	1.6%	0.54	0.10	1.6%
72.0	0.053	12.2	0.142	20.3	3183	1.0%	0.60	0.05	1.0%

Table Appendices-7 Performance measurements: inlet geometry 6

Temp (F)	ΔP4-5 (inH20)	Flow (CFM)	ΔP1-2 (inH2O)	Power (W)	Fan Speed (RPM)	Fan Static Efficiency	ψ	ϕ	η
74.5	0.874	50.7	0.053	22.1	3138	1.4%	0.34	0.23	2.1%
74.5	0.675	44.4	0.072	21.5	3175	1.8%	0.38	0.20	2.2%
74.5	0.489	37.8	0.082	20.4	3210	1.8%	0.39	0.17	2.1%
74.5	0.301	29.6	0.098	20.4	3206	1.7%	0.44	0.13	1.8%
74.5	0.147	20.5	0.110	20.5	3200	1.3%	0.47	0.09	1.3%
74.5	0.046	11.3	0.129	20.5	3181	0.8%	0.54	0.05	0.8%

Table Appendices-8 Performance measurements: inlet geometry 7

Temp (F)	ΔP4-5 (inH20)	Flow (CFM)	ΔP1-2 (inH2O)	Power (W)	Fan Speed (RPM)	Fan Static Efficiency	ψ	ϕ	η
72.1	1.167	58.6	0.076	23.0	2935	2.3%	0.54	0.28	3.3%
72.1	0.930	52.3	0.087	22.1	3028	2.4%	0.52	0.25	3.2%
72.1	0.667	44.2	0.118	21.5	3083	2.9%	0.61	0.20	3.3%
72.1	0.415	34.7	0.140	21.0	3140	2.7%	0.65	0.16	2.9%
72.1	0.193	23.5	0.169	20.5	3170	2.3%	0.73	0.11	2.3%
72.1	0.055	12.4	0.186	20.6	3166	1.3%	0.79	0.06	1.3%

Table Appendices-9 Performance measurements: inlet geometry 8

Temp (F)	ΔP4-5 (inH20)	Flow (CFM)	ΔP1-2 (inH2O)	Power (W)	Fan Speed (RPM)	Fan Static Efficiency	ψ	ϕ	η
69.1	1.628	69.2	0.103	24.3	2709	3.4%	0.86	0.36	5.0%
69.1	1.125	57.4	0.120	22.8	2989	3.6%	0.72	0.27	4.5%
69.1	0.797	48.2	0.143	21.9	3070	3.7%	0.74	0.22	4.3%
69.1	0.470	36.9	0.178	20.9	3155	3.7%	0.81	0.17	4.0%
69.1	0.216	24.9	0.201	20.6	3183	2.9%	0.86	0.11	2.9%
69.1	0.058	12.7	0.230	20.7	3168	1.7%	0.97	0.06	1.7%

Table Appendices-10 Performance measurements: inlet geometry 9

Temp (F)	ΔP4-5 (inH20)	Flow (CFM)	ΔP1-2 (inH2O)	Power (W)	Fan Speed (RPM)	Fan Static Efficiency	ψ	ϕ	η
70.3	1.734	71.4	0.125	23.7	2695	4.4%	1.01	0.38	6.2%
70.3	1.272	61.1	0.137	23.1	2903	4.3%	0.87	0.30	5.4%
70.3	0.858	50.1	0.162	21.6	3085	4.4%	0.82	0.23	5.1%
70.3	0.505	38.3	0.193	21.0	3165	4.1%	0.87	0.17	4.4%
70.3	0.224	25.4	0.217	20.5	3190	3.2%	0.92	0.11	3.2%
70.3	0.061	13.1	0.246	20.8	3160	1.8%	1.04	0.06	1.8%

Table Appendices-11 Performance measurements: inlet geometry 10

Temp (F)	ΔP4-5 (inH20)	Flow (CFM)	ΔP1-2 (inH2O)	Power (W)	Fan Speed (RPM)	Fan Static Efficiency	ψ	ϕ	η
75.4	1.815	73.1	0.125	24.4	2730	4.4%	1.01	0.38	6.2%
75.4	1.341	62.8	0.150	23.9	2933	4.6%	0.93	0.30	5.8%
75.4	0.913	51.9	0.174	21.6	3064	4.9%	0.91	0.24	5.6%
75.4	0.514	38.8	0.199	20.8	3141	4.4%	0.92	0.18	4.7%
75.4	0.229	25.8	0.217	20.4	3187	3.2%	0.93	0.12	3.3%
75.4	0.059	12.8	0.250	20.8	3154	1.8%	1.07	0.06	1.8%

Table Appendices-12 Performance measurements: inlet geometry 11

Temp (F)	ΔP4-5 (inH20)	Flow (CFM)	ΔP1-2 (inH2O)	Power (W)	Fan Speed (RPM)	Fan Static Efficiency	ψ	ϕ	η
69.9	1.877	74.7	0.126	24.0	2655	4.6%	1.08	0.40	6.6%
69.9	1.358	63.5	0.149	22.6	2890	4.9%	0.95	0.31	6.2%
69.9	0.923	52.0	0.177	21.5	3026	5.0%	0.93	0.24	5.8%
69.9	0.536	39.5	0.200	21.0	3109	4.4%	0.94	0.18	4.7%
69.9	0.238	26.1	0.219	20.6	3141	3.3%	0.96	0.12	3.4%
69.9	0.068	13.8	0.251	20.9	3121	2.0%	1.09	0.06	2.0%

Table Appendices-13 Performance measurements: inlet geometry 12

Temp (F)	ΔP4-5 (inH20)	Flow (CFM)	ΔP1-2 (inH2O)	Power (W)	Fan Speed (RPM)	Fan Static Efficiency	ψ	ϕ	η
72.3	0.999	54.2	0.061	22.5	2999	1.7%	0.42	0.26	2.5%
72.3	0.828	49.3	0.085	22.1	3071	2.2%	0.49	0.23	2.8%
72.3	0.613	42.3	0.105	21.6	3094	2.4%	0.54	0.19	2.8%
72.3	0.368	32.7	0.125	21.2	3127	2.3%	0.58	0.15	2.4%
72.3	0.177	22.5	0.147	20.8	3165	1.9%	0.64	0.10	1.9%
72.3	0.052	12.1	0.166	21.0	3152	1.1%	0.71	0.05	1.1%

Table Appendices-14 Performance measurements: inlet geometry 13

Temp (F)	ΔP4-5 (inH20)	Flow (CFM)	ΔP1-2 (inH2O)	Power (W)	Fan Speed (RPM)	Fan Static Efficiency	ψ	ϕ	η
72.0	1.707	70.9	0.081	25.0	2652	2.7%	0.78	0.38	4.3%
72.0	1.362	63.3	0.088	22.9	2801	2.9%	0.68	0.32	4.1%
72.0	1.006	54.3	0.098	22.2	2990	2.8%	0.60	0.26	3.6%
72.0	0.728	46.1	0.128	21.5	3084	3.2%	0.66	0.21	3.7%
72.0	0.441	35.8	0.149	21.0	3135	3.0%	0.69	0.16	3.2%
72.0	0.223	25.3	0.177	20.6	3161	2.6%	0.77	0.11	2.6%
72.0	0.072	14.2	0.199	20.8	3160	1.6%	0.85	0.06	1.6%

Table Appendices-15 Performance measurements: inlet geometry 14

Temp (F)	ΔP4-5 (inH20)	Flow (CFM)	ΔP1-2 (inH2O)	Power (W)	Fan Speed (RPM)	Fan Static Efficiency	ψ	ϕ	η
73.7	1.449	65.5	0.098	23.4	2813	3.2%	0.75	0.33	4.6%
73.7	1.072	56.3	0.114	22.6	2970	3.3%	0.70	0.27	4.2%
73.7	0.740	46.7	0.132	21.8	3021	3.3%	0.71	0.22	3.8%
73.7	0.434	35.6	0.158	21.4	3086	3.1%	0.76	0.16	3.3%
73.7	0.202	24.1	0.186	21.1	3120	2.5%	0.83	0.11	2.6%
73.7	0.059	12.9	0.209	21.2	3110	1.5%	0.92	0.06	1.5%

Table Appendices-16 Performance measurements: inlet geometry 15

Temp (F)	ΔP4-5 (inH20)	Flow (CFM)	ΔP1-2 (inH2O)	Power (W)	Fan Speed (RPM)	Fan Static Efficiency	ψ	ϕ	η
73.6	1.707	71.2	0.120	24.3	2712	4.1%	0.98	0.37	5.8%
73.6	1.183	59.1	0.130	22.7	2940	4.0%	0.80	0.29	5.0%
73.6	0.795	48.4	0.148	21.9	3071	3.8%	0.77	0.22	4.4%
73.6	0.462	36.7	0.176	21.3	3117	3.6%	0.82	0.17	3.8%
73.6	0.214	24.9	0.191	20.9	3139	2.7%	0.85	0.11	2.7%
73.6	0.058	12.8	0.221	21.2	3129	1.6%	0.96	0.06	1.6%

Table Appendices-17 Performance measurements: inlet geometry 16

Temp (F)	ΔP4-5 (inH20)	Flow (CFM)	ΔP1-2 (inH2O)	Power (W)	Fan Speed (RPM)	Fan Static Efficiency	ψ	ϕ	η
75.0	1.464	65.9	0.104	24.0	2717	3.4%	0.84	0.35	4.7%
75.0	1.102	57.1	0.119	22.8	2896	3.5%	0.76	0.28	4.4%
75.0	0.774	47.8	0.146	21.7	3061	3.8%	0.76	0.22	4.3%
75.0	0.448	36.2	0.175	20.8	3146	3.6%	0.80	0.16	3.8%
75.0	0.205	24.3	0.194	20.5	3150	2.7%	0.85	0.11	2.8%
75.0	0.055	12.4	0.223	20.6	3167	1.6%	0.95	0.06	1.6%
75.0	0	0.0	0.289	20.6	3159	0.0%	1.23	0.00	0.0%

Table Appendices-18 Performance measurements: inlet geometry 17

Temp (F)	ΔP4-5 (inH20)	Flow (CFM)	ΔP1-2 (inH2O)	Power (W)	Fan Speed (RPM)	Fan Static Efficiency	ψ	ϕ	η
75.8	1.520	67.2	0.098	24.2	2618	3.2%	0.88	0.37	4.6%
75.8	1.100	57.1	0.121	22.9	2888	3.6%	0.78	0.28	4.5%
75.8	0.770	47.7	0.142	21.7	3040	3.7%	0.75	0.22	4.2%
75.8	0.458	36.7	0.169	21.0	3121	3.5%	0.79	0.17	3.7%
75.8	0.217	25.1	0.190	20.7	3148	2.7%	0.84	0.11	2.8%
75.8	0.059	12.9	0.220	20.9	3131	1.6%	0.96	0.06	1.6%
75.8	0	0.0	0.282	20.9	3130	0.0%	1.22	0.00	0.0%

Table Appendices-19 Performance measurements: inlet geometry 18

Temp (F)	ΔP4-5 (inH20)	Flow (CFM)	ΔP1-2 (inH2O)	Power (W)	Fan Speed (RPM)	Fan Static Efficiency	ψ	ϕ	η
76.8	1.385	64.2	0.092	24.5	2570	2.8%	0.85	0.36	4.1%
76.8	1.045	55.7	0.115	23.1	2830	3.3%	0.77	0.28	4.1%
76.8	0.772	47.8	0.140	22.2	2974	3.5%	0.78	0.23	4.1%
76.8	0.453	36.5	0.169	21.3	3112	3.4%	0.80	0.17	3.6%
76.8	0.209	24.6	0.188	20.9	3145	2.6%	0.83	0.11	2.7%
76.8	0.059	12.9	0.219	21.0	3125	1.6%	0.96	0.06	1.6%
76.8	0	0.0	0.278	20.7	3148	0.0%	1.19	0.00	0.0%

Table Appendices-20 Performance measurements: inlet geometry 19

Temp (F)	ΔP4-5 (inH20)	Flow (CFM)	ΔP1-2 (inH2O)	Power (W)	Fan Speed (RPM)	Fan Static Efficiency	ψ	ϕ	η
74.5	1.444	65.4	0.093	25.0	2487	2.9%	0.92	0.37	4.1%
74.5	1.095	56.9	0.117	23.6	2859	3.3%	0.77	0.28	4.2%
74.5	0.757	47.2	0.148	22.2	2965	3.7%	0.82	0.23	4.2%
74.5	0.468	37.0	0.175	21.3	3102	3.6%	0.83	0.17	3.8%
74.5	0.207	24.4	0.199	20.7	3171	2.8%	0.86	0.11	2.8%
74.5	0.054	12.3	0.227	20.8	3152	1.6%	0.97	0.06	1.6%
74.5	0	0.0	0.289	20.6	3162	0.0%	1.22	0.00	0.0%

Table Appendices-21 Performance measurements: inlet geometry 20

Temp (F)	ΔP4-5 (inH20)	Flow (CFM)	ΔP1-2 (inH2O)	Power (W)	Fan Speed (RPM)	Fan Static Efficiency	ψ	ϕ	η
75.5	1.393	64.3	0.087	25.0	2425	2.6%	0.92	0.38	3.8%
75.5	1.056	55.9	0.114	23.6	2764	3.2%	0.80	0.29	4.0%
75.5	0.738	46.6	0.136	22.6	2912	3.3%	0.79	0.23	3.8%
75.5	0.459	36.7	0.172	21.2	3121	3.5%	0.81	0.17	3.7%
75.5	0.209	24.6	0.196	20.7	3140	2.7%	0.87	0.11	2.8%
75.5	0.055	12.4	0.223	20.7	3146	1.6%	0.96	0.06	1.6%
75.5	0	0.0	0.282	20.6	3150	0.0%	1.21	0.00	0.0%

Table Appendices-22 Performance measurements: IG 0 VW +0.04"

Temp (F)	ΔP4-5 (inH20)	Flow (CFM)	ΔP1-2 (inH2O)	Power (W)	Fan Speed (RPM)	Fan Static Efficiency	ψ	ϕ	η
70.4	0.079	14.9	0.256	21.4	3160	2.1%	1.09	0.07	2.1%
70.4	0.256	27.1	0.217	20.9	3181	3.3%	0.93	0.12	3.4%
70.4	0.529	39.2	0.190	21.5	3131	4.1%	0.88	0.18	4.4%
70.4	0.870	50.5	0.158	22.6	2992	4.2%	0.86	0.24	4.8%
70.4	1.225	60.0	0.132	23.4	2817	4.0%	0.89	0.30	5.0%
70.4	1.544	67.4	0.118	24.3	2655	3.9%	0.97	0.36	5.3%

Table Appendices-23 Performance measurements: IG 0 VW +0.08"

Temp (F)	ΔP4-5 (inH20)	Flow (CFM)	ΔP1-2 (inH2O)	Power (W)	Fan Speed (RPM)	Fan Static Efficiency	ψ	ϕ	η
73.0	0.079	14.9	0.284	21.4	3092	2.3%	1.26	0.07	2.3%
73.0	0.274	28.2	0.242	21.0	3133	3.8%	1.07	0.13	3.9%
73.0	0.586	41.4	0.220	21.5	3118	5.0%	1.03	0.19	5.3%
73.0	0.962	53.2	0.178	22.6	2988	4.9%	0.97	0.25	5.7%
73.0	1.340	62.9	0.148	23.4	2783	4.7%	1.02	0.32	5.9%
73.0	1.660	70.1	0.109	24.6	2513	3.7%	1.05	0.40	5.2%
73.0	1.503	66.7	0.038	26	1457	1.1%	1.62	0.65	2.5%

Table Appendices-24 Performance measurements: IG 0 VW +0.12"

Temp (F)	ΔP4-5 (inH20)	Flow (CFM)	ΔP1-2 (inH2O)	Power (W)	Fan Speed (RPM)	Fan Static Efficiency	ψ	ϕ	η
71.1	0.080	15.0	0.297	22.1	3077	2.4%	1.33	0.07	2.4%
71.1	0.289	28.9	0.267	21.5	3122	4.2%	1.19	0.13	4.3%
71.1	0.629	42.8	0.239	21.7	3093	5.5%	1.13	0.20	5.9%
71.1	1.111	57.1	0.216	23.1	2874	6.3%	1.26	0.28	7.2%
71.1	1.474	65.8	0.169	24.9	2522	5.3%	1.40	0.37	6.5%
71.1	1.548	67.5	0.101	25.1	2346	3.2%	1.12	0.41	4.6%
71.1	1.55	67.5	0.048	26	1500	1.5%	1.74	0.64	2.8%

Table Appendices-25 Performance measurements: IG 0 VW +0.16"

Temp (F)	ΔP4-5 (inH20)	Flow (CFM)	ΔP1-2 (inH2O)	Power (W)	Fan Speed (RPM)	Fan Static Efficiency	ψ	ϕ	η
71.1	0.084	15.4	0.319	22.5	2980	2.6%	1.52	0.07	2.6%
71.1	0.315	30.3	0.291	22.2	2993	4.7%	1.41	0.14	4.8%
71.1	0.673	44.5	0.260	23.0	2846	5.9%	1.45	0.22	6.3%
71.1	1.062	56.0	0.200	24.5	2529	5.4%	1.52	0.32	6.2%
71.1	1.347	63.1	0.151	25.2	2240	4.5%	1.60	0.40	5.6%
71.1	1.493	66.5	0.048	25.8	1477	1.5%	1.77	0.64	2.8%

Table Appendices-26 Performance measurements: IG 0 VW +0.20"

Temp (F)	ΔP4-5 (inH20)	Flow (CFM)	ΔP1-2 (inH2O)	Power (W)	Fan Speed (RPM)	Fan Static Efficiency	ψ	ϕ	η
74.1	0.088	15.8	0.330	23.2	2888	2.6%	1.69	0.08	2.6%
74.1	0.333	31.1	0.310	23.0	2899	4.9%	1.61	0.15	5.1%
74.1	0.677	44.6	0.255	23.7	2798	5.6%	1.48	0.23	6.0%
74.1	1.039	55.4	0.198	25.0	2391	5.2%	1.69	0.33	5.9%
74.1	1.288	61.7	0.148	25.5	2135	4.2%	1.72	0.41	5.2%
74.1	1.399	64.4	0.094	25.8	1819	2.8%	1.72	0.50	3.9%
74.1	1.395	64.3	0.04	26	1387	1.2%	1.77	0.66	2.3%

Table Appendices-27 Performance measurements: IG 7 VW +0.12"

Temp (F)	ΔP4-5 (inH20)	Flow (CFM)	ΔP1-2 (inH2O)	Power (W)	Fan Speed (RPM)	Fan Static Efficiency	ψ	ϕ	η
71.5	0.057	12.6	0.220	21.3	3153	1.5%	0.94	0.06	1.5%
71.5	0.206	24.3	0.188	21.0	3148	2.6%	0.82	0.11	2.6%
71.5	0.431	35.4	0.162	21.0	3153	3.2%	0.74	0.16	3.4%
71.5	0.706	45.4	0.130	22.1	3064	3.1%	0.67	0.21	3.6%
71.5	0.997	54.1	0.108	22.5	2918	3.1%	0.68	0.26	3.9%
71.5	1.269	61.1	0.065	23.3	2879	2.0%	0.52	0.30	3.1%

Table Appendices-28 Performance measurements: IG 7 VW +0.16"

Temp (F)	ΔP4-5 (inH20)	Flow (CFM)	ΔP1-2 (inH2O)	Power (W)	Fan Speed (RPM)	Fan Static Efficiency	ψ	ϕ	η
72.2	0.062	13.2	0.239	21.6	3096	1.7%	1.06	0.06	1.7%
72.2	0.228	25.6	0.208	21.6	3100	2.9%	0.94	0.12	3.0%
72.2	0.502	38.3	0.181	21.9	3089	3.7%	0.86	0.18	4.0%
72.2	0.757	47.1	0.140	22.2	3021	3.5%	0.75	0.22	4.0%
72.2	1.085	56.5	0.110	23.0	2880	3.2%	0.72	0.28	4.1%
72.2	1.340	62.9	0.090	23.6	2828	2.8%	0.68	0.32	4.0%

Table Appendices-29 Performance measurements: Fan without inlet geometry

Nozzle Diameter	Temp (F)	ΔP4-5 (inH20)	Flow (CFM)	ΔP1-2 (inH2O)	Power (W)	Fan Speed (RPM)	Fan Static Efficiency
		0.000	0.00	0.330	21.4	3163	0.00%
		0.064	13.41	0.289	20.8	3205	2.19%
		0.144	20.28	0.271	20.4	3221	3.17%
		0.226	25.51	0.250	20.4	3209	3.68%
		0.433	35.50	0.228	20.8	3180	4.58%
		0.583	41.28	0.216	21.1	3146	4.97%
		0.748	46.83	0.200	21.5	3119	5.13%
1.6"	72.3	0.948	52.80	0.179	21.7	3092	5.12%
		1.186	59.12	0.164	22.2	2992	5.14%
		1.462	65.70	0.153	23.3	2835	5.08%
		1.558	67.84	0.148	23.6	2741	5.01%
		1.656	69.96	0.141	23.9	2640	4.86%
		1.643	69.70	0.073	25.6	2410	2.34%
		1.693	70.76	0.067	25.8	2213	2.16%
		1.715	71.22	0.008	26.0	1889	0.26%

CURRICULUM VITAE

NAME: Yoel Tanquero

CONTACT INFORMATION: 5024 Middlesex Drive, Louisville, KY 40245
Work: (502) 452-7547
Cell: (786) 234-1032
ytanquero@gmail.com

DOB: April 11, 1987

EDUCATION & TRAINING: M.S. Mechanical Engineering (exp. 05/2017)
University of Louisville
(GPA: 3.62 / 4.00)
2014 – Present

B.S. Mechanical Engineering
Florida International University
(GPA: 3.31 / 4.00)
2011 – 2014

WORK EXPERIENCE:

GE Appliances, Louisville, KY June 2014 – Present
Edison Engineering Development Program

4th Rotation, Range: Advanced Systems January 2016 – Present

- Developed an infrared temperature sensor algorithm to detect water boiling
- Validated a new enamel coating for steam-clean oven cavities
- Developed a Particle Tracking Velocimetry (PTV) system

3rd Rotation, Dishwasher: Production Engineering July 2015 – January 2016

- Redesigned multiple dishwasher door parts to improve assembly and unit performance.
- Led cost takeout projects like changing the material of the handle and redesigning the detergent cup.

2nd Rotation, Microwave: New Product Introduction January 2015 – July 2015

- Coordinated cross-functional global teams to complete project requirements for technical feasibility.
- Led the product evaluation and field tests.
- Performed the unit reliability test and root cause analysis on failures.

1st Rotation, Refrigeration: New Product Introduction July 2014 – January 2015

- Designed sealed system parts to meet DOE and program requirements
- Performed reliability tests at component level

GE Appliances, Louisville, KY January 2012 – August 2012
Technology Co-op

2th Co-op Rotation, Advance Technologies May 2012 – August 2012

- Designed spray arm system for dishwasher
- Performed fluid dynamics simulations for spray arm system developed

1st Co-op Rotation, Dishwasher: New Product Introduction January 2012 – May 2012

- Coordinated metallurgical analysis for stainless steel tub
- Performed door/hinge and controls reliability test

Aeronautical Investments Inc., Miami, FL August 2011 – January 2012
Technical Support Engineer

- Provided technical support and off-site troubleshooting of Flight Data Monitoring (FDM) systems to company clients
- Update and maintenance of FDM reports database

US Drafting Solutions, Miami, FL October 2010 – August 2011

CAD Drafter

- Created several engineering CAD drawings.
- Maintained CAD database and data collectors' information.

TECHNICAL SKILLS:

- Fan/System curve setup and measurement,
- Particle Tracking Velocimetry (PTV) measurements
- Finite Element Analysis (FEA)
- Computational Fluid Dynamics (CFD)
- Rapid prototyping

COMPUTER SKILLS & LANGUAGES:

Proficient: Solidworks, ProE, ANSYS Workbench / Fluent, Minitab, Matlab, Arduino, LabVIEW

Familiar: Star CCM+, Programming C++, Visual Basic, AutoCAD

Proficient in Spanish

PROFESSIONAL SOCIETY MEMBERSHIPS:

- ASME (member since 2011)